INVESTIGATION OF THE STRUCTURE OF LIGHT NEUTRON RICH ISOTOPES USING BREAKUP REACTIONS AT RELATIVISTIC ENERGIES

Jose Fernández Vázquez

17th October 2003

Contents

List of Figures

List of Tables

Resumen

La interacción fuerte es la responsable de que los quarks estén ligados formando nucleones y los nucleones formando núcleos. Mientras que el primer tipo de unión se puede explicar empleando la Cromodinámica Cúantica (QCD), el segundo puede únicamente ser descrito utilizando fuerzas nucleares fenomenológicas. Existen dos formas diferentes de tratar el problema de la caracterización de la fuerza entre nucleones: la difusión nucleón-nucleón (NN), y el estudio de sistemas nucleares de muchos cuerpos. En este último caso la competición entre las fuerzas nuclear y electromagnética define qué núcleos pueden existir y cuántos protones y neutrones pueden estar ligados dentro de un núcleo. El balance entre estas fuerzas determina en gran parte los detalles estructurales relativos a estos núcleos, por ejemplo sus masas y vidas medias. En consecuencia, el estudio experimental de las propiedades macroscópicas y estructurales de los núcleos permite profundizar en nuestro conocimiento sobre la fuerza nuclear.

En nuestro universo sólo existen 273 núcleos estables frente a cualquier desintegración espontánea. Cuando los representamos en una tabla de núcleos, éstos pueblan la llamada línea de estabilidad. El conocimiento que tenemos sobre el tratamiento de sistemas nucleares de muchos cuerpos se basa fundamentalmente en ellos. La fuerza nuclear es capaz de ligar además muchos otros núcleos no estables. El número de isótopos inestables que se predice que existen es de alrededor de 6000 y sólo 2500 han sido sintetizados en el laboratorio.

En la figura 1.1 se muestra el panorama actual de la tabla de núcleos. En dicha tabla los núcleos estables están representados por cuadrados negros. El área sombreada en gris claro corresponde a aquellos núcleos inestables que han podido ser sintetizados en el laboratorio. Para un elemento dado, el número máximo y mínimo de neutrones que pueden estar ligados define lo que se conoce como límite de existencia nuclear para neutrones y protones, respectivamente, que en la figura 1.1 viene indicado por el límite del área sombreada en gris oscuro.

Actualmente, y a pesar de los avances logrados en los últimos años, aún ex-

isten limitaciones tecnológicas que impiden el acceso experimental a todos estos núcleos exóticos. En particular, y tal como se muestra en la figura 1.1, sólo para núcleos ligeros hasta alrededor de Z=9 ambos límites de existencia han podido ser alcanzados experimentalmente. La zona sombreada en gris oscuro en la figura 1.1 representa a todos aquellos isótopos inestables que todavía no han podido ser sintetizados. Numerosos experimentos realizados con núcleos ligeros cercanos al límite de existencia han revelado la aparición de nuevos fenómenos interesantes, tales como el halo (de protones y neutrones), el reordenamiento de los orbitales, el cambio de números mágicos, la aparición de deformación y otros. Estos experimentos han abierto nuevas perspectivas en el estudio de la fuerza nuclear.

Los núcleos exóticos juegan igualmente un papel fundamental en astrofísica nuclear. De hecho, la mayoría de los procesos de nucleosíntesis durante los primeros instantes del Universo y posterior evolución estelar implican la participación de dichos núcleos. En este sentido, el estudio de los núcleos exóticos contribuye a mejorar los modelos astrofísicos actuales con las consecuencias que ello tiene en nuestra comprensión del Universo.

Este trabajo se dedica al estudio experimental de núcleos ligeros ricos en neutrones en la capa sd utilizando reacciones de ruptura a energías relativistas. Nos centraremos en particular en núcleos cercanos al límite de existencia con un número de neutrones cercano a N=16.

Resulta inevitable referirse al fenómeno de halo nuclear cuando hablamos de núcleos ligeros ricos en neutrones. Para núcleos cercanos al valle de la estabilidad las densidades de protones y de neutrones tienen perfiles muy similares, sin embargo, cuando nos acercamos al límite de existencia de neutrones nos encontramos con núcleos que tienen funciones de densidad de neutrones considerablemente más extendidas que las de protones. El exceso de neutrones hace que el pozo de potencial para neutrones creado por la fuerza nuclear esté lleno hasta el límite. En consecuencia, los neutrones más externos se encuentran débilmente ligados, lo que les permite desplazarse por efecto túnel a regiones clásicamente prohibidas durante un intervalo de tiempo no despreciable. El mismo razonamiento es extensible para protones con la particularidad de que la presencia del potencial Coulombiano reduce la probabilidad de penetración de la barrera y en consecuencia la fracción de la función de onda que se encuentra en la región prohibida se ve reducida respecto al caso de halo de neutrones.

Una de las herramientas más sofisticadas que se utiliza para obtener información espectroscópica acerca de los núcleos exóticos son las reacciones de ruptura.

Como en esta tesis trabajaremos con núcleos ligeros ricos en neutrones nos restringiremos al caso de la separación del (o de los) neutron(es) de valencia. Este canal de reacción se define como la separación de un neutrón externo del núcleo proyectil (el núcleo exótico en nuestro caso) al interaccionar con un blanco, el cual no afecta al fragmento restante. Desde los primeros experimentos realizados en GANIL [Ann90] (Grand Accelerateur Nationale d'Ions Lourds) y MSU [Orr92] (Michigan State University) con el ^{11}Li, se ha alcanzado un gran progreso [Bau98, Baz98, Nav98, Sme99, Aum00, Nav00, Sau00b, Cor01, Mad01]. Los primeros experimentos se limitaban a la medida de la distribución de momento longitudinal inclusivo de los fragmentos producidos. Este tipo de medidas trajo consigo información importante acerca del contenido en momento angular del nucleón arrancado del proyectil exótico. Más tarde, se introdujeron las medidas de las correspondientes secciones eficaces. Estas cantidades son extremadamente importantes para deducir información acerca de los factores espectroscópicos relacionados con dichos núcleos. El último observable incluido ha sido la medida de la emisión de rayos γ por parte de los fragmentos en coincidencia con la medida de la distribución de momento de los mismos.

Los isótopos de oxígeno próximos al límite de existencia de neutrones constituyen un área de estudio muy excitante. Por ejemplo, se ha visto recientemente que el ^{22}O tiene un primer estado excitado 2^+ a $3{,}17\ MeV$ [Thi00], mientras que en el ^{24}O no se ha observado ningún estado excitado por debajo de los $4\ MeV$ [Sta03], y podría tratarse de núcleos doblemente mágicos. Esto indica una persistencia del cierre de capa de protones en Z=8, y (sub)cierres de capas de neutrones en N=14 y N=16 [Oza00, Cor03b]. Al mismo tiempo, la no observación del isótopo ^{28}O, el cual tendría veinte neutrones, parece indicar que se produce un debilitamiento o desaparición del cierre de capa en N=20, siendo el último isótopo ligado de oxígeno que existe en la zona de los núcleos ricos en neutrones el ^{24}O [Tar97, Sak99, Oza02].

La hipótesis de que el ^{24}O tiene una capa cerrada $(2s_{1/2})^2$ fue confirmado por E. Sauvan *et al.* [Sau03], quienes observaron una distribución de momento longitudinal del ^{22}O relativamente estrecha tras la separación de un neutrón del ^{23}O. Este experimento condujo a una asignación de espín y paridad (J^π) del estado fundamental del ^{23}O igual a $\frac{1}{2}^+$. Sin embargo, R. Kanungo *et al.* [Kan02] atribuyeron $J^\pi = \frac{5}{2}^+$ al estado fundamental del ^{23}O, poniendo de manifiesto un conflicto experimental. Es posible obtener sin ambigüedades el espín y paridad del estado fundamental del ^{23}O a partir de medidas exclusivas de distribuciones de momento de fragmentos tras la separación del neutrón, tal y como se describe en este trabajo.

Desde el punto de vista teórico, se ha logrado un gran avance en la descripción de este tipo de experimentos. En un trabajo reciente de B. A. Brown *et al.* [Bro02] se ha puesto en evidencia que las reacciones de separación de un único neutrón a energías intermedias y relativistas en cinemática inversa permiten una asignación precisa de la probabilidad de ocupación de partícula independiente para núcleos exóticos. Estos avances también han permitido explicar el efecto de la modificación de capas nucleares a medida que aumenta el isospín (T_z). Según T. Otsuka *et al.* [Ots01] este fenómeno se debería a una modificación en la interacción nucleón-nucleón, en particular a la parte dependiente del espín y del isospín.

El experimento en el que se basa esta tesis se llevó a cabo en el FRS (Separador de FRagmentos) en el GSI, Darmstadt (Alemania). A partir de un haz primario de ^{40}Ar a una energía de aproximadamente $1\ AGeV$ se produjo por fragmentación nuclear en un blanco de produción de Be un haz secundario compuesto. De todos los isótopos producidos, únicamente ^{17,18,19,20,21}N, ^{19,20,21,22,23,24}O y ^{22,23,24,25,26,27}F fueron sometidos a estudio. La primera parte del FRS se fijó a un valor de rigidez magnética óptimo para la transmisión de los isótopos de oxígeno. Con el fin de cubrir todos los isótopos, fue necesario utilizar diferentes valores de rigidez magnética. Puesto que la aceptancia en momento del FRS es del orden de $\pm 1\,\%$, la transmisión de otros núcleos con valores de rigidez magnética cercanos pudo realizarse simultáneamente. Todos los proyectiles fueron completamente identificados con respecto a A y Z.

Un blanco de reacción situado en el plano focal intermedio permitió el estudio de las siguientes reacciones:

- separación de un neutrón en un blanco de carbono para los núcleos: ^{17,18,19,20}N, ^{19,20,21,22,23}O, ^{22,23,24,25,26}F
- separación de un neutrón en un blanco de plomo para los núcleos: ^{19,20}N, ^{22,23}O, ^{25,26}F
- separación de dos neutrones en un blanco de carbono para los núcleos: ^{21}N, ^{24}O, ^{27}F

La segunda parte del FRS se fijó a un valor de rigidez magnética que permitió optimizar la transmisión de los isótopos de oxígeno producidos en el blanco de reacción situado en el plano focal intermedio. Los fragmentos también fueron identificados en A y Z en la segunda parte del FRS.

La utilización de una serie de detectores de posición permitió determinar las trayectorias de los proyectiles exóticos y los fragmentos. A partir de las medidas de posición en el último plano focal fue posible determinar con gran precisión las distribuciones de momento de los distintos fragmentos producidos en la reacción y transmitidos a lo largo de la segunda parte del FRS.

Un conjunto de centelleadores de NaI situado justo detrás del blanco de reacción permitió obtener espectros de rayos γ y emitidos por los diferentes fragmentos producidos.

Los siguientes observables fueron medidos en este experimento:

- secciones eficaces de separación de uno o dos neutrones. Estos observables se determinaron por medio del cociente entre el número de fragmentos justo después del blanco de reacción situado en el plano focal intermedio del FRS y el número de proyectiles antes del mismo blanco. Cuando las medidas no pudieron ser realizadas en dicho plano focal fue necesaria la aplicación de una corrección por transmisión

- distribuciones de momento de los fragmentos emergentes de la reacción. Para este tipo de medidas fue necesario emplear el FRS, un espectrómetro magnético de gran resolución, en modo de pérdida de energía. En este modo de funcionamiento, es posible asociar directamente diferencias de posición de los fragmentos en el último plano focal con diferencias de momento en el plano focal intermedio, donde la reacción ha tenido lugar. A las medidas experimentales de las distribuciones de momento se les sustrajo la resolución intrínseca de dicho espectrómetro, obtenida experimentalmente. También se estudió el efecto causado por la diferente pérdida de energía que cada núcleo sufre en el blanco dependiendo de la profundidad a la que tiene lugar la reacción («location straggling»), el cual resultó ser despreciable

- espectro de rayos γ emitidos por los fragmentos producidos en las distintas reacciones. En ciertos casos, cuando se tenía suficiente estadística, se pudieron distinguir los diferentes estados finales del fragmento (medidas exclusivas). Esto se llevó a cabo por medio de la detección simultánea de los fragmentos y los rayos γ emitidos por los mismos. Puesto que los rayos γ fueron emitidos por fuentes en movimiento -a energías relativistas- se aplicó una serie de correciones para recuperar el espectro «original» : *addback* (para recuperar sucesos que depositan su energía en varios detectores), corrección Doppler, multiplicidad. Dicho procedimiento presenta tres problemas esenciales: la indeterminación del punto de emisión del rayo

γ, necesario para la corrección Doppler, el corrimiento Doppler, que reduce la eficiencia, y el ensanchamiento Doppler, que limita la resolución final en energía asociada al detector. Estos dos últimos efectos también pueden impedir la resolución en energía de picos cercanos. Para la aplicación de esta técnica de coincidencias entre la detección del fragmento y la detección de los rayos γ procedentes la desexcitación del mismo fue necesaria la realización de una simulación completa (en GEANT) de la respuesta del conjunto de centelleadores

A continuación pasamos a describir los resultados más relevantes obtenidos en este trabajo:

Las secciones eficaces de separación de un neutrón presentan un claro efecto par-impar a la vez que aumentan con A dentro de una cadena isotópica. Estos resultados han sido comparados con otras medidas similares realizadas a energías más bajas [Sau00a] (en torno a $60\ AMeV$), observándose un buen acuerdo general. También se ha observado que las secciones eficaces medidas con el blanco de plomo son mayores que las obtenidas con el blanco de carbono, lo que era de esperar, puesto que la interacción Coulombiana es mayor en el caso del blanco de plomo.

También se han medido las distribuciones de momento de los fragmentos emergentes de la reacción de separación con el objetivo de investigar la variación del llenado de orbitales con el isospín. De nuevo encontramos un buen acuerdo general con otras medidas realizadas a energías más bajas [Sau00a]. Además, la comparación de nuestros datos para los dos blancos considerados indica que los perfiles obtenidos para las distribuciones longitudinales son muy parecidos. Por lo tanto, nuestros resultados confirman que el perfil de la distribución de momento longitudinal es independiente de la energía a la que se realiza la colisión y de la naturaleza del blanco empleado para ello [Bau99, Sau00b].

Al comparar las anchuras de las distribuciones de momento de los fragmentos emergentes de las reacciones de separación de un neutrón obtenidas en el experimento (FWHM), se observa un cambio significativo de comportamiento cuando llegamos a N=14 (para el fragmento). Este cambio coincide con el comienzo de llenado del nivel $2s_{1/2}$ en el modelo de partícula independiente. También en esta ocasión se han observado efectos de apareamiento (par-impar), que son explicables puesto que los proyectiles con un número impar de neutrones deberían tener el neutrón de valencia menos ligado, y por lo tanto la distribución de momento del fragmento debería resultar más estrecha.

La medida de la coincidencia entre los fragmentos emergentes de la reacción y los rayos γ emitidos por los mismos permitió separar fragmentos producidos en el estado fundamental de fragmentos producidos en estados excitados. El método de las coincidencias se aplicó a aquellos núcleos que presentaban picos en el espectro de rayos γ. La razón entre el número de fragmentos producidos en estados excitados y el número de fragmentos producidos en el estado fundamental puede ser una buena medida de la polarización del centro compacto dentro del proyectil, siempre y cuando no se produzca excitación de fragmentos durante la reacción.

Finalmente presentamos la interpretación de los resultados experimentales:

Las secciones eficaces de separación del neutrón de valencia han sido empleadas para identificar posibles candidatos a núcleo con halo, en particular el ^{23}O [Oza01]. El ^{23}O no presenta una sección eficaz de separación de un neutrón demasiado grande, tanto para el blanco de carbono como para el de plomo, comparada con la de sus vecinos de la cadena isotópica. El incremento observado puede explicarse considerando que se trata de un núcleo con un número impar de neutrones. Su neutrón de valencia debería estar en el estado $2s_{1/2}$, y, desde el punto de vista del modelo de partícula independiente, el centro compacto llena los niveles $1p_{1/2}$ para protones y $1d_{5/2}$ para neutrones, situación que lo vuelve relativamente estable. Esto, junto con el elevado valor obtenido para la energía de separación del último neutrón ($2{,}74 \pm 0{,}12\ MeV$), parece indicar que este núcleo no presenta un halo de neutrones.

El ^{26}F tiene una sección eficaz de separación de un neutrón baja comparada con la de su vecino, el ^{25}F. Este resultado parece indicar que el neutrón desapareado se encuentra en el nivel $1d_{3/2}$, sin descartar el nivel $2s_{1/2}$. La distribución de momento del fragmento emergente de la reacción de ruptura del ^{26}F (el ^{25}F) tiene un perfil que es característico de una onda s. Estos dos hechos podrían indicar que el neutrón arrancado en esta reacción tiene una probabilidad importante de proceder del nivel $2s_{1/2}$.

En cuanto a la separación de dos neutrones del proyectil exótico, no es éste un proceso tan directo como la separación de un neutrón, así que las conclusiones que se puedan extraer han de ser contempladas con prudencia. El canal de separación de dos neutrones se estudió para: el ^{24}O, el cual presenta valores aparentemente «normales» tanto para la sección eficaz como para la anchura de la distribución de momento, lo que probablemente confirma que no se trata de un núcleo con halo. Por otra parte, el ^{27}F presenta una sección eficaz de separación de dos neutrones elevada y una distribución de momento estrecha, pudiendo

indicar ambos observables que el ^{27}F es un núcleo con halo. Sería interesante realizar un experimento similar al descrito en este trabajo, centrado esta vez en los isótopos ^{26,27}F, con el objetivo de obtener datos específicos para estos núcleos.

Sólo se han observado picos claros en espectros de rayos γ de fragmentos que proceden de proyectiles con un número impar de neutrones (^{18,20}N, ^{21,23}O, ^{22}F). Esto podría indicar que hay polarización del centro compacto de dichos núcleos. La presencia de picos en el espectro también parece independiente de la reacción, puesto que los tres espectros de rayos γ del ^{18}N (obtenido tras separación de un neutrón en carbono y en plomo, y separación de dos neutrones en carbono) presentan el mismo pico.

La controversia generada acerca de la asignación de espín y paridad al estado fundamental del ^{23}O necesitaba de un estudio más completo, como lo son las medidas exclusivas presentadas en este trabajo. La distribución experimental de momento longitudinal del fragmento ^{22}O obtenida tras la separación de un neutrón sobre blanco de carbono ha sido comparada con distribuciones teóricas obtenidas en el marco del modelo de Glauber. Estos cálculos se han mostrado para momentos angulares $l = 0$ y $l = 2$. Claramente puede verse que la distribución que mejor se ajusta a los resultados experimentales es la que asume un neutrón en el nivel $2s_{1/2}$, el cual se acopla al centro compacto, que se halla en su estado fundamental 0^+. Por lo tanto podemos concluir que el espín y paridad del estado fundamental del ^{23}O es el $J^\pi = 1/2^+$, desmintiendo los resultados obtenidos por Kanungo *et al.* [Kan02].

No hemos observado picos en los espectros de rayos γ de los fragmentos ^{19,21}O, lo que esta de acuerdo con las predicciones del modelo de capas (OXBASH) para los isótopos ^{20,22}O (centro compacto principalmente en el estado fundamental). Por lo tanto es lógico pensar que los isótopos ^{20,22}O se ajustan bastante bien al modelo de partícula independiente.

Finalmente, los datos experimentales han sido comparados con calculos realizados en el marco de un modelo teórico más sofisticado que el de partícula independiente (Glauber + QRPA + QP-C) y se ha obtenido una buena concordancia con las predicciones teóricas de los factores espectroscópicos para centros compactos en su estado fundamental. También se ha hallado un acuerdo razonable entre nuestros datos experimentales y las predicciones teóricas (tanto para partícula independiente como para el modelo de acoplamiento cuasipartícula-centro compacto -QP-C-) para los estados fundamentales del ^{21}O ($\frac{5}{2}^+$) y del ^{23}O ($\frac{1}{2}^+$). Los cálculos con QP-C también predicen que los niveles $2s_{1/2}$ y $1d_{5/2}$

se hallan muy cercanos para estos núcleos.

Hemos encontrado, sin embargo, ciertas discrepancias a la hora de comparar, para centros compactos en distintos estados excitatos, los correspondientes factores espectroscópicos obtenidos experimentalmente con los calculados de forma teórica (Glauber + QRPA + QP-C). Esto puede deberse a la aproximación semiclásica (aproximación eikonal) que se ha empleado para describir el mecanismo de reacción. Por lo tanto, cabe esperar que un análisis más cuantizado (por ejemplo, usando DWBA) daría mejores resultados.

Este experimento nos ha proporcionado una gran cantidad de nuevas medidas consistentes para contrastar cálculos teóricos de algunos observables importantes que pueden ayudar a entender la estructura de los núcleos exóticos que se hallan próximos al límite de existencia. La aplicación del método de las coincidencias permite obtener las distribuciones longitudinales de momento para diferentes estados excitados del centro compacto tras la reacción, lo que nos da información acerca del momento angular orbital asociado al neutrón de valencia. También nos da acceso a factores espectroscópicos determinados de modo experimental, que podrían ser en un futuro cercano muy útiles para probar el poder de predicción de los diferentes modelos teóricos utilizados en la interpretación de los datos. Los factores espectroscópicos experimentales deducidos en este trabajo constituyen un conjunto de datos único, puesto que de momento son los únicos que han sido obtenidos a energías relativistas, y para núcleos relativamente pesados.

Este trabajo abre nuevas perspectivas en el campo de la investigación de núcleos exóticos ligeros utilizando reacciones de ruptura. Desde un punto de vista experimental, el uso de detectores de rayos γ de gran granularidad permitiría reducir la incertidumbre experimental asociada a las medidas.

La contribución del autor de esta memoria al trabajo presentado incluye la colaboración en la preparación del dispositivo experimental y sus diferentes calibraciones, en particular la matriz de centelleadores de NaI, la participación en la toma de datos y el análisis completo de los mismos, junto con su correspondiente interpretación.

Chapter 1

Introduction

The strong interaction is behind the binding of quarks in nucleons and nucleons in nuclei. While the former is understood within the frame of Quantum Chromo-Dynamics (QCD), the latter can only be described using phenomenological nuclear forces. Two different approaches can be followed to characterize the nuclear force: NN scattering and the nuclear many-body system. The competition between the nuclear and the electromagnetic force defines which nuclei can exist and how many protons and nucleons can be bound together. The balance between these forces determines the structural details related to the nuclei, for instance their masses and half lives. In this way, the experimental investigation of the structure of nuclei provides important constraints on the nuclear force.

In our universe, there are approximately 273 nuclei stable against any spontaneous decay. When we represent them in a chart of nuclides they populate the so called stability line. Most of the knowledge that we have about the nuclear many-body systems rely on stable nuclei.

Many other non-stable nuclei are bound by the nuclear force. Theoretical estimations indicate that the number of expected non-stable isotopes is close to 6000. During the last decades, advances in accelerator technologies have allowed the production of approximately 2500 of such non-stable nuclei.

In figure 1.1, we show the present landscape of the nuclides. Stable nuclei are represented by black squares, and the light grey area corresponds to those nuclei that have been synthesized in the laboratory. For a given element, the maximum and minimum number of neutrons leading to bound nuclei is defined by the so called neutron and proton driplines, which delimit the frontiers of nuclear existence, and are shown in figure 1.1 as the limit of the dark grey area.

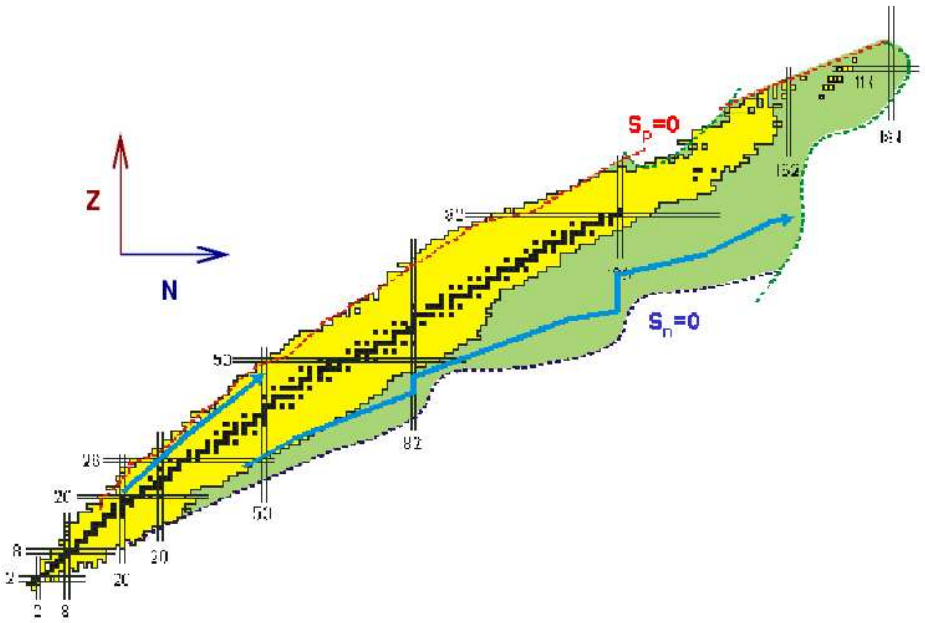

Figure 1.1: Chart of the nuclides. Stable nuclei are represented by black squares, the light gray area corresponds to radioactive nuclei that can be synthesized in the laboratory, and the dark gray area corresponds to the theoretical prediction for particle stability.

Technological problems remain that limit experimental access to very exotic nuclei close to the driplines. Particularly, for light nuclei up to approximately Z=9 both driplines have been reached, as demonstrated in figure 1.1. Experiments performed with nuclei in this region of the chart of the nuclides reveal interesting phenomena such as the proton and neutron halo, orbital reordering, change in magic numbers, and deformation, which have opened new perspectives in the study of the nuclear force.

The exotic nuclei also play a major role in Nuclear Astrophysics. Indeed, the majority of nucleosynthesis processes in the early Universe and later on in the Stars, involved non-stable nuclei. In this respect, the study of exotic nuclei improves the present astrophysical models and our understanding of the Universe.

1.1 Light neutron-rich nuclei

In this section, we will briefly introduce major advances achieved in recent decades in the field of light exotic nuclei. We will attempt to summarize the status of this knowledge, particularly from an experimental point of view. We will concentrate on results achieved for light neutron-rich nuclei as they are the object of the present study. Particular emphasis been placed on information obtained using breakup reactions as spectroscopic tools.

The area of light neutron-rich nuclei has revealed interesting phenomena, including the neutron-halo. For nuclei close to the valley of stability the proton and neutron densities present similar profiles. However, when we approach the neutron dripline, we find nuclei which present a neutron density function considerably more extended than that of the proton. This excess of neutrons results in a potential well completely filled for neutrons, with the "outer" neutrons being loosely bound. As a consequence, these loosely bound nucleons can move to classically forbidden regions for a non negligible amount of time (tunneling effect), and then return to the potential well. Some authors [Jen00] define a halo as when the valence nucleon(s) spend more than 50% of the time in the forbidden region.

The discovery of ^{6}He in 1936 [Bje36] can be considered as the birth of the exotic nuclei physic. Subsequentially, in 1951 the first online mass separator [Kof51] was built. This new experimental apparatus made it possible to better investigate the nuclear properties of specific nuclei. Then, in 1966 ^{11}Li was observed for the first time [Pos66]. The discovery of ^{11}Li being a bound nuclei was quite surprising since its (A-1,Z) neighbour ^{10}Li is not bound. A subsequent spectroscopic study [Kla69] was carried out to unveil its nuclear structure. Also, other exotic nuclei (^{11}Be, ^{8}B, ^{8}He, and ^{17}F) were produced at a later stage.

Progress in the study of dripline nuclei depends very much on the quality of production methods of exotic nuclei. At this point, we would like to make reference to the pioneering fragmentation experiments at Berkeley [Sym79, Wes79] which began in 1979 and resulted in the performance of extensive experimental and theoretical research.

Subsequently, in 1983 a very large $E1$ transition was observed for ^{11}Be [Mil83]. In 1985 total reaction cross-section measurements [Tan85a, Tan85b] indicated that ^{11}Li has a large matter radius by comparison to its neighbours. This experiment motivated Hansen and Jonson [Han87] to develop a theoretical model to interpret the results, it was then when the term "halo" appeared for the first

time in this context. In 1987 almost identical magnetic momenta were observed in ^{11}Li and ^{9}Li [Arn87]. Later, in 1992 the quadrupole momenta of those nuclei were measured [Arn92], with similar charge and different matter distributions being found. However, in 1988, after dissociation reactions of ^{11}Li [Kob88], a narrow transverse momentum distribution width was found for the fragment ^{9}Li, and in 1989 [Kob89], a still narrower width was observed for the longitudinal momentum distribution after breakup, a result confirmed in 1990 by [Ann90].

At this time the image of a halo consisting of a valence nucleon coupled to an inert core was more or less accepted for the case of neutrons. However, the existence of proton halos was a more controversial topic. The presence of a Coulomb potential for the proton halo reduces the tunneling probability and reduces the fraction of wave function outside the core region. With respect to these facts, one should mention the pionnering experiment performed at the FRS [Sch95] where the ^{8}B was appointed as a single proton halo in its ground state. Later experiments confirmed this observation, for example [Neg96, Sme99, Cor01].

Following on from this intriguing background, a new experimental plan began in the mid 1980's, devoted to the exploration of unknown areas of the chart of the nuclides. New experimental probes were designed, which were used in conjunction with other established techniques used for stable nuclei. The ultimate objective was to decipher the structure of these exotic nuclei by considering different perspectives. These new experiments were at the beginning oriented towards quite simple observables, for example, interaction and reaction cross-sections measurements [Tan85a, Tan85b, Oza02, Vis02]. Elastic and inelastic scattering [Cor97, Thi00, Kah00, Lag01, Lap01, Ege02] were soon used with these radioactive nuclear beams.

Over time more complex experiments were designed in order to measure further sophisticated observables. The experimental set-ups gained complexity which was directly translated into greater amounts of good quality data. We would like to mention, as an example, β-decay experiments [Bor86, Bor88, Bor91, Bor93], transfer reactions studies [For99], and in-flight γ-ray spectroscopy experiments [Bel01, Gui02, Sta03] performed with exotic beams.

The breakup, or knockout process, is considered one of the most sophisticated tools used to obtain spectroscopic information with exotic nuclei. This reaction channel is defined as the removal of an external nucleon from a projectile (the exotic nuclei in our case) by the target, leaving the remaining fragment unaffected. Since the original experiments performed at GANIL [Ann90] (Grand Accelerateur Nationale d'Ions Lourds) and MSU [Orr92] (Michigan State Uni-

versity) with ^{11}Li, great advances have been made in the field [Bau98, Baz98, Nav98, Sme99, Aum00, Nav00, Sau00b, Cor01, Mad01]. The first experiments were limited to the measurement of the inclusive longitudinal momentum distribution of the emerging fragments. Such measurements produced important information regarding the angular momentum content of the nucleon removed from the exotic projectile, with the measurement of the corresponding cross-sections being introduced at a later stage. These quantities have been proven to be extremely important in order to deduce spectroscopic information related to these exotic nuclei. The last observable included was the γ de-excitation of these fragments in coincidence with the momentum fragment measurement. We would also like to mention the results achieved using this technique at relativistic energies for the particular case of the proton halo nucleus ^{8}B [Cor02, Cor03a].

Neutron-rich oxygen isotopes near the neutron-drip line constitute a very exciting area. It has been proven recently that ^{22}O with a first excited 2^+ state at $3.17\ MeV$ [Thi00] and ^{24}O with no excited state below $4\ MeV$ [Sta03] appear to be doubly magic nuclei. This indicates a persistence of the proton-magic shell at Z=8 and (sub-) shell closures at N=14 and N=16 [Oza00, Cor03b]. At the same time, the non-observation of ^{28}O with twenty neutrons indicates a weakening of the N=20 shell; the last bound oxygen isotope is ^{24}O [Tar97, Sak99, Oza02].

The tentative assignment of ^{24}O having a closed $(s_{1/2})^2$ shell was corroborated by Sauvan *et al.* [Sau00b] who measured a relatively narrow longitudinal momentum distribution of ^{22}O after neutron knockout from ^{23}O, leading to a ground-state spin and parity of $J^\pi = 1/2^+$ for ^{23}O. In contrast to these findings, Kanungo *et al.* [Kan02] attributed $J^\pi = 5/2^+$ to the ^{23}O ground state. This controversy prompted a comment by Brown *et al.* [Bro03] where a consistent analysis of the available *inclusive* data in terms of a $(1d_{5/2})^6(2s_{1/2})^1$ configuration for ^{23}O was given. The experimental confirmation of such theoretical analysis requires an *exclusive* knockout measurement, where the states of the core fragment are identified by recording in coincidence the corresponding de-exciting γ-rays. This has been done in the experiment that we will present in the following chapters.

From a theoretical point of view, great steps have been taken in this field, considering its earlier periods, when the momentum distributions of the core fragments were simply described with the aid of semiclassical representations, neglecting any reaction mechanism or final state interaction. More recently, in [Bro02] it has been demonstrated that single-nucleon knockout reactions, at intermediate and high energies, in inverse kinematics allow quite precise assessment of single-particle occupancies, even when exotic projectiles are used. If the γ de-excitation of the fragments is recorded in coincidence with the fragment

momentum distributions, we can also identify core fragment states after the interaction. This particular work makes use of the *so-called* **quasiparticle-core coupling model** to account for the structure of the nuclei, and describes the reaction mechanism by means of the **eikonal theory**.

It is important to mention the modification of nuclear shells observed experimentally when the isospin (T_z) increases. One possible interpretation, given by Otsuka *et al.* [Ots01], would attribute this phenomenon to the modification in the strength of the spin-isospin dependent part of the nucleon-nucleon interaction in exotic nuclei. This term outlines the existence of a strongly attractive interaction between one proton and one neutron in spin-orbit coupling partner orbitals ($l \pm 1/2$ and $l \mp 1/2$), respectively (l is the orbital angular momentum). In the case of non exotic nuclei, the respective partners are similarly filled and the attraction is very strong, thus determining an approximation in energies between them. However, in the case of nuclei with very different numbers of protons and neutrons the situation changes. This is the case of ^{24}O, where the proton population of the $1d_{5/2}$ level is expected to be very low, in contrast with the neutron population of the level $1d_{3/2}$. As a consequence, there is not much attraction between these partners and the level $1d_{3/2}$ shifts towards higher energies, showing the appearance of a large gap, ($\sim 6\ MeV$) [Bro83], between $2s_{1/2}$ and $1d_{3/2}$ levels, and also, the disappearance of the gap between the $1d_{3/2}$ level and the pf shell. Subsequentially, the N=20 magic number disappears and a new magic number appears at N=16 for this nuclide (see figure 1.2). This effect, in different magnitude, should also be present in neighbouring nuclei. One experimental indication of the vanishing of N=20 is the existence of anomalies in the binding energies of nuclei around ^{24}O, which has been pointed out by [Oza00].

This work is devoted to the experimental investigations of light neutron rich isotopes in the sd shell using breakup reactions at relativistic energies. In particular, we will be focusing on $^{17-21}$N,$^{19-24}$O and $^{22-27}$F (shown in figure 1.3), where we have studied mainly one-neutron removal reactions. We will concentrate on isotopes that are close to the dripline and have neutron numbers around N=16. In particular, ^{23}O is a candidate to a one-neutron halo nucleus, it is close to the new proposed shell N=16, and the spin and parity of its ground state are still under discussion.

If we assume that the removal of the nucleon produced in the breakup reaction leaves the remaining fragment unaffected by the reaction itself, we can obtain the following information from the measured observables:

1. the removal cross-section informs us of the spatial extension of the removed

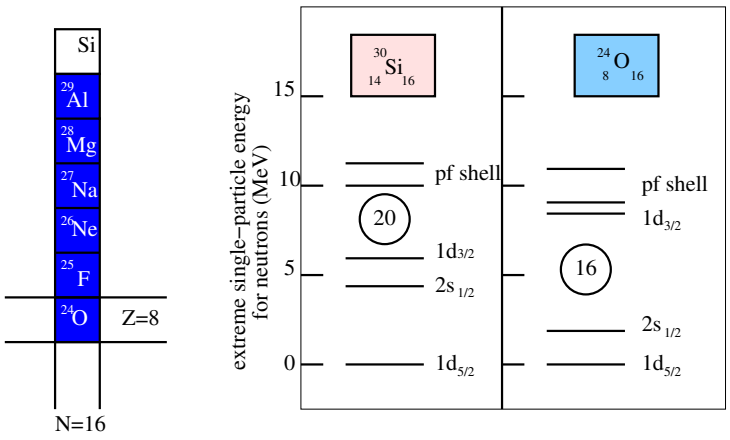

Figure 1.2: We present in this figure the evolution of the nuclear shells for different isospin nuclei. The example compares the dripline nucleus ^{24}O to the stable ^{30}Si. As a result of the neutrons $1d_{3/2}$ level energy rising when moving towards the neutron dripline (where the number of neutrons is very different from the number of protons and the attraction between spin orbit coupling partner orbitals is smaller [Ots01]), the magic number N=20 vanishes and a new energy gap appears at N=16.

nucleon(s) wave function, when they were still inside the projectile, just before the reaction. This data, once complemented with the corresponding cross-sections analyzed in the framework of an eikonal reaction theory, yield for spectroscopic factors [Bro02]

2. the momentum distribution profile and the total removal cross-section provide unique structure information. The momentum distribution of the fragment is related to the momentum distribution of the removed nucleon(s). This, in turn, is related to the Fourier transform of the probability density of these valence nucleon(s) since the momentum and the position are reciprocal coordinates. The longitudinal momentum distribution of the core fragment determines the orbital angular momentum l of the valence nucleon removed from the projectile, by comparing the shape of the experimental momentum distribution with theoretical ones assuming a given l value for the valence nucleon.
   The combination of these two observables establishes important constrains for the different models proposed to explain the experimental results. This makes it possible to choose between different model calculations the one that best fits the experimental results

3. The γ rays emitted by the core fragment provide direct information about

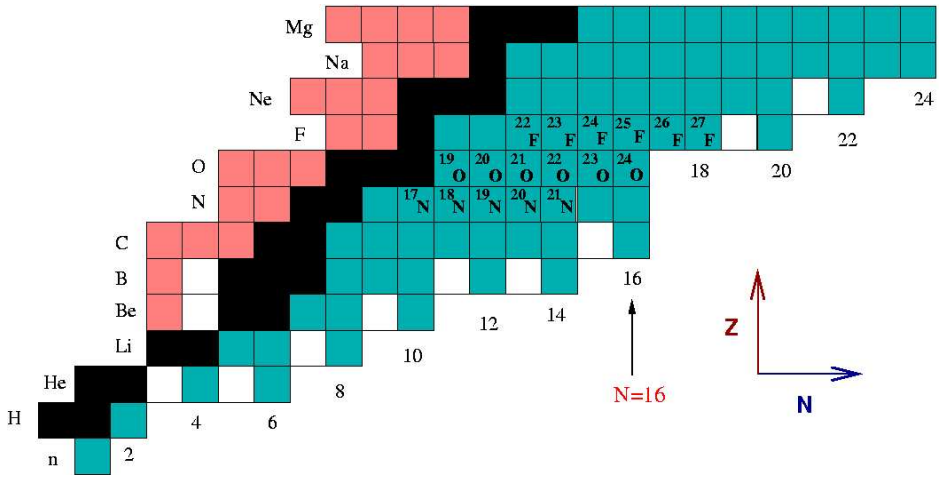

Figure 1.3: Zoom on the chart of the nuclides for light isotopes. Stable nuclei are represented by black squares. The neutron deficient nuclei are represented by light gray squares, whereas the dark gray squares represent the neutron-rich nuclei. The light neutron-rich nuclei studied in this work are indicated.

the different individual final levels populated. If the remaining fragment after breakup is not affected by the reaction, its detection in an excited state is due to the fact that it was already excited inside the projectile.
The measurement of the γ rays emitted by the core fragment in coincidence with its momentum distribution makes it possible to select the individual momentum distribution of the core fragment produced in the different states. This is of special interest to our studies, as it would allow to disentangle the different contributions to the wave function of the valence nucleon(s) inside the exotic projectile before the reaction (due to the sensitivity of the momentum distribution to the orbital angular momentum l of the projectile).
As a result, the coincidence between the emitted γ rays and the core fragment momentum distribution gives *direct experimental information* about the detailed nuclear structure of the projectile

The results of these investigations are presented in this thesis, which is organized as follows:

- the second chapter presents the technique and the experimental method used in this work

- the data evaluation and the definition of the main experimental observables are presented in the third chapter
- in the fourth chapter we present the main experimental results which are compared with those obtained at lower energies
- the fifth chapter is devoted to the interpretation of the experimental data using model calculations for both the nuclear structure and the reaction mechanism
- finally, we present the main conclusions and perspectives of this work

Chapter 2

The experimental setup

In this chapter we will discuss the technical aspects related to the experiment.

In order to study the behaviour of the nuclear force near the neutron dripline, we needed an experimental facility to measure the observables introduced in chapter **1**. The experimental requirements were a heavy ion accelerator able to provide relativistic primary beams from which the secondary exotic nuclei could be produced by nuclear fragmentation, a high resolution magnetic spectrometer equipped with different detectors to identify and determine the trajectory of projectiles and fragments and a gamma detector able to measure the γ de-excitation of fragments.

2.1 The accelerator and experimental facilities at GSI

The GSI (Gesellschaft für Schwerlonenforschung) [GSI] is a heavy ion research center located in Darmstadt (Germany). It is able to provide high energy and high intensity beams, from protons to Uranium, for different applications.

We used the following GSI accelerator facilities and experimental areas (See figure 2.1): the ion sources, providing primary beams for the experiments; the UNIversal Linear ACcelerator (UNILAC), accelerating primary beams up to $2 - 20\ AMeV$; the Heavy-Ion Synchrotron (SIS), which ultra-accelerates those primary beams (all the elements of the periodic system up to Uranium) to more than 90% of the speed of light; and finally, the FRagment Separator (FRS), the high resolution magnetic spectrometer where the experiment took place.

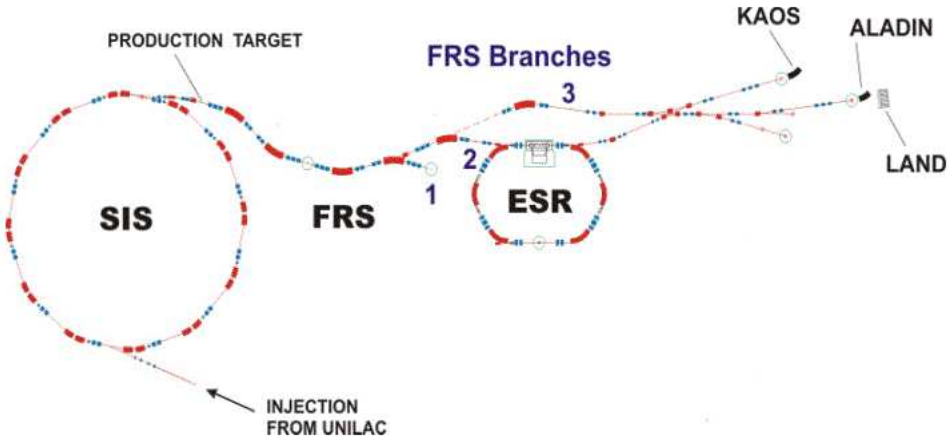

Figure 2.1: Schematic view of the radioactive nuclear beam facility at GSI. The heavy ions are accelerated by the linear accelerator (UNILAC) and by the synchrotron (SIS) up to a maximum energy of $1000 - 2000\ AMeV$, the ions are converted to interesting exotic nuclei at the entrance of the fragment separator (FRS). The inflight separated fragments are investigated directly at the FRS (1), in the storage ring ESR (2), or in the target hall (3) where ALADDIN, LAND, and KAOS are located.

2.2 The fragment separator FRS

The FRS [FRS, Gei92], which was first used in **1990**, is a high-resolution forward spectrometer designed for research studies with relativistic heavy ions. It ensures an efficient separation of secondary beams produced via projectile fragmentation (or fission) at the production target (see figures **??**).

The momentum resolving power of the FRS is $R \approx 1500$ for an emittance of 20π mm·mrad and a transmission of $\pm 1\%$ in $\frac{\Delta p}{p}$. With the FRS it is possible to analyse heavy-ion beams with magnetic rigidities ranging from 5 to 18 T·m. During the experiment, the FRS made use of a specially designed ion optics for breakup studies that ensured the measurement of the complete momentum distribution in one single setting. Consequentially, this ion optics presents a lower resolving power $R \approx 1040$ compared to the standard FRS $R \approx 1500$.

The FRS has four stages (see figure 2.2). Each stage consists of one *30 degrees* dipole magnet to separate different velocities, five quadrupole magnets to provide *first order* focussing, and two sextupole magnets to correct *second order* optical aberrations. Quadrupoles and sextupoles are located before and

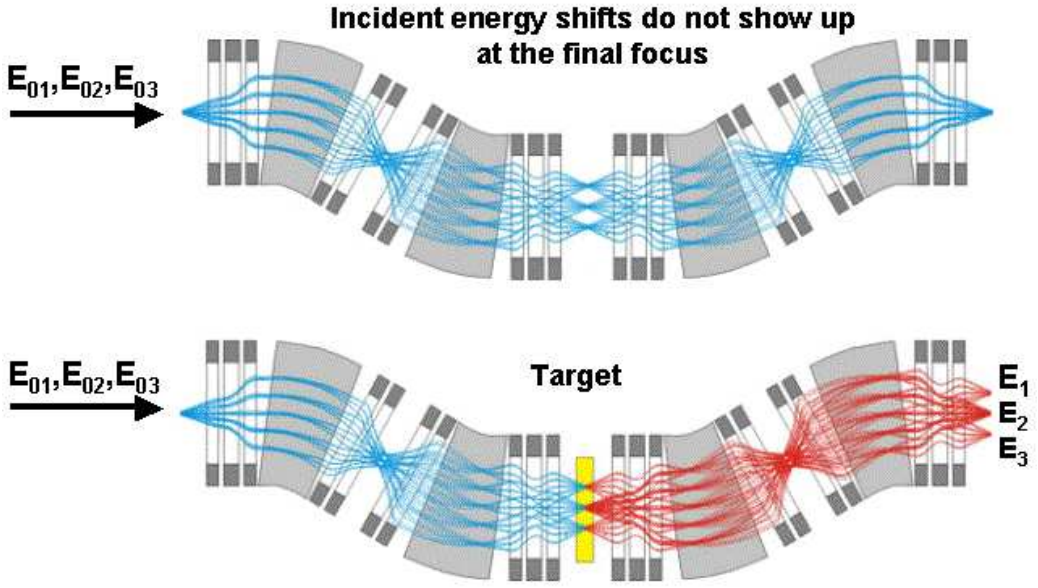

Figure 2.2: The FRS has four stages. Each stage has one dipole magnet, five quadrupole lenses, and two sextupole lenses. This plot shows how the FRS works in energy-loss mode: in the ideal situation, without breakup target at the intermediate focal plane, we have point-to-point imaging (even for different energies) between the entrance and the exit of the FRS. If we place now a breakup target at the intermediate focal plane of the FRS, **only** the energy differences induced by the target will show up at the exit of the fragment separator.

after each dipole (see figure 2.2). There are four focal planes, each one after each stage of the spectrometer.

In our experiment, the FRS worked in *energy-loss mode*. The *energy-loss mode* is a special ion optical setting for a two-stage spectrometer where the combination of both stages is an *achromatic system*, while each stage by itself is dispersive. The dispersion of the first stage is compensated by the dispersion of the second stage, therefore this mode is also called *dispersion matched mode*.

If we insert a *target* in the intermediate focal plane of the FRS ($S2$, the separation point of the two dispersive stages), the momentum change can be measured with the dispersion of the second stage. This can be done because the energy-loss is independent of the energy spread of the incoming beam. For a detailed discussion of this mode see [Gei92].

The first energy-loss spectrometer was proposed by *C. Schaerf* and *R. Scrimaglio* in **1964** as a new magnetic analyzer for scattering experiments [Sch64], and are still today ideal tools for measurements using exotic beams.

The change in momentum induced by the breakup reaction in the intermediate focal plane is (at relativistic energies) two orders of magnitude smaller than the acceptance of the spectrometer. Consequently, it would be impossible to distinguish this effect from the initial momentum spread of the secondary beam in a direct measurement. When working in *energy-loss mode*, the change in momentum due to the breakup reaction can be measured independently of the initial momentum spread of the secondary beam. This guarantees an effective measurement of the longitudinal momentum distribution of the fragments after the breakup reaction.

2.3 Detectors

The FRS was the environment in which our experiment took place. We equipped the FRS with several detectors located at different focal plane positions **S1**, **S2** and **S4**. (see figure 2.3). These detectors are described in the following sections, together with the main calibration procedures applied in order to extract physical information from the measurements. They have been separated into three groups: beam monitor, ionisation detectors and scintillators.

2.3.1 Beam monitor: SEETRAM

The SEcondary Electron TRAnsmission Monitor (SEETRAM) [Zie91] placed at the entrance of the FRS is a detector that **measures the intensity of the primary beam** delivered by the SIS.

The SEETRAM consists of three aluminum foils placed in a vacuum environment (see figure 2.4). The two outer layers are connected to a positive potential ($80\ V$), and the inner layer (cathode) is set to ground. When an ion passes through the SEETRAM, some electrons close to the surface of the inner foil may leave the foil, generating a positive current in the central layer. The current is integrated all over the spill, resulting in a quantity proportional to the number of incoming ions.

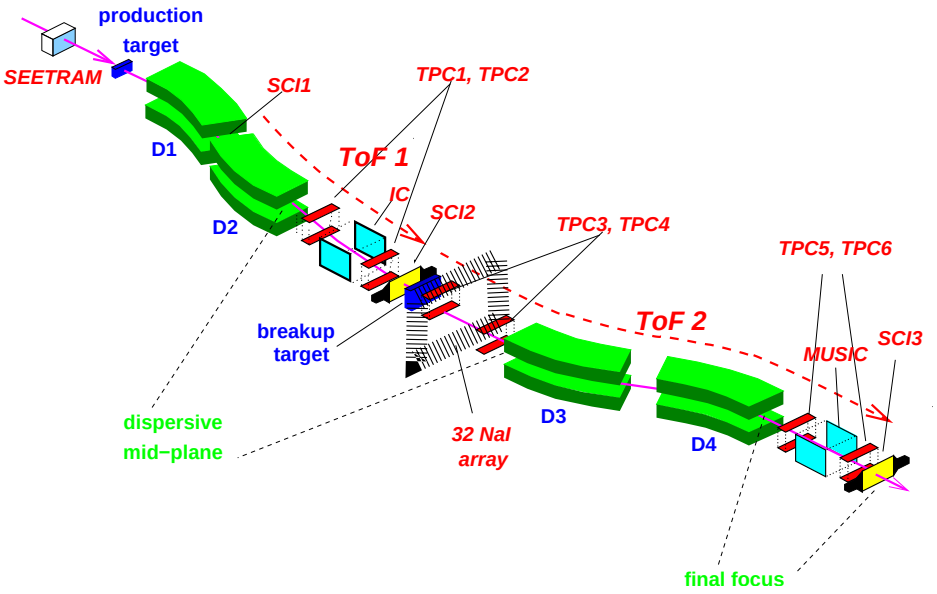

Figure 2.3: Experimental setup of the FRS used in the experiment. A secondary radioactive beam of projectiles was produced from the primary beam at the production target. These secondary projectiles can loose one or more nucleons after stripping at the intermediate breakup target. For the complete identification of the projectiles before and after the breakup target, ionisation chambers, plastic scintillators and time projection chambers were used. Finally, γ rays emitted by the fragments produced in an excited state could be detected by a NaI crystals array.

Due to the fact that the SEETRAM is mainly vacuum and the three foils are very thin ($8.90\ mg/cm^2$ in total), less than 0.1 % of the beam particles react with the SEETRAM layers. This makes it a very efficient beam monitor. The SEETRAM does not directly give the total number of particles that pass through it, but only a proportional signal.

A plastic scintillator was placed between the SEETRAM and the production target to calibrate the beam monitor. Since the plastic scintillator is able to measure the number of ions, it is possible to use it to find the proportionality factor which relates the signal provided by the SEETRAM and the real number of counts. The calibration measurements were done using the SEETRAM and the plastic scintillator simultaneously to count the total number of particles per spill for different primary beam intensities (see figure 2.5). For more details about the calibration of the SEETRAM the interested reader can consult [Caa02, SEETRAM, Jur02]. The proportionality factor used to convert from

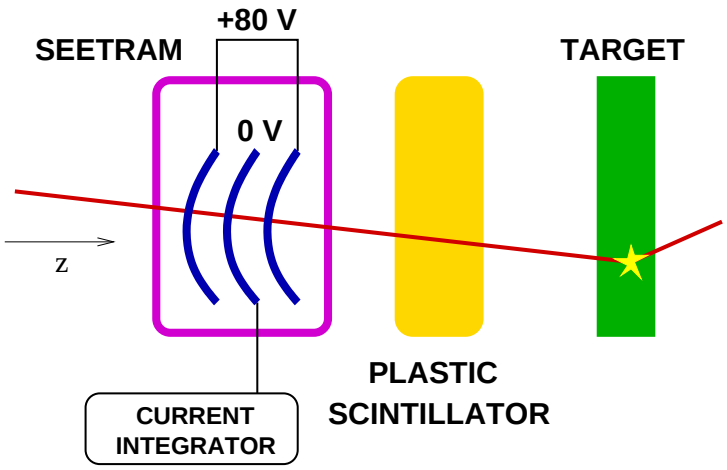

Figure 2.4: Schematic view of the SEETRAM and its location at the beam line, just in front of the production target. The plastic scintillator used for the calibration of the SEETRAM is also shown. After the calibration measurements are done, the plastic scintillator is removed from the beam line. The anodes and cathode foils are curved in order to achieve better mechanical stability.

equivalent counts in the SEETRAM to the real number of ions was, in this experiment, equal to 3571 ± 5 ions/SEETRAM pulse.

It is important to mention that in this work the SEETRAM has been used only to obtain the incident beam intensity in the calculation of the *two-neutron removal* cross-sections.

2.3.2 Ionisation detectors

A ionisation detector [Leo93] is basically a gas filled container (normally a mixture of argon and other species) with an anode and a cathode that are kept at a given voltage. An ionizing particle that penetrates inside the detector generates a cloud of gas ions and free electrons that depends on the speed of the incoming particle and is proportional to the square of its charge. The produced electrons drift towards the anode and the positive ions towards the cathode.

In the experiment two types of ionisation detectors were used: the ionisation chambers and the time projection chambers.

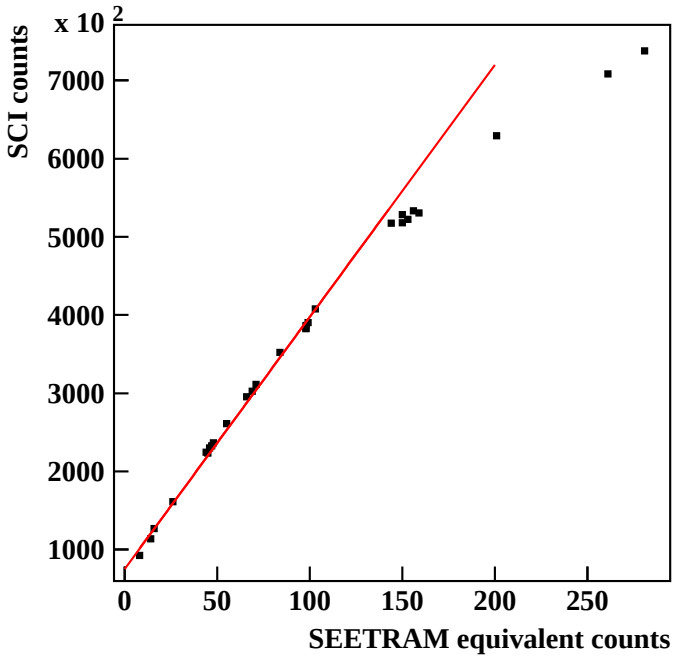

Figure 2.5: Total number of counts per spill measured by the SEETRAM and the plastic scintillator for different argon beam intensities. At low intensities it is clearly a linear dependence. At high intensities the plastic scintillator saturates, as can be seen from the deviation with respect to the linear fit. Taken from [Caa02].

2.3.2.1 Ionisation chambers

In an ionisation chamber [Sto99, Pfu94] the amount of ionisation produced is relatively independent of small variations in the voltage applied to it. This occurs because at the working voltage all the ionisation produced by the incident particle is collected without generating additional electron-ion pairs (*avalanche* effect). By recording the electron signal, which is proportional to the shower produced by the incident particle, we can obtain the charge of the particle passing through, given that the velocity is known.

In our experiment we used two ionisation chambers for the *charge identification (Z)* of the projectiles and the fragments. The small Ionisation Chamber (small IC [Sto99]) located at S2 identified the exotic projectiles, and the MUltiple Sampling Ionisation Chamber (MUSIC [Pfu94]) located at S4 identified the fragments.

The MUSIC is an ionisation chamber $60\ cm$ thick filled with $P10$ gas, while the small IC is a detector $40\ cm$ thick filled with CF_4 gas. Both detectors are operated at normal pressure and room temperature, and have four anodes that are used to obtain the average of four different measurements (see figure 2.6).

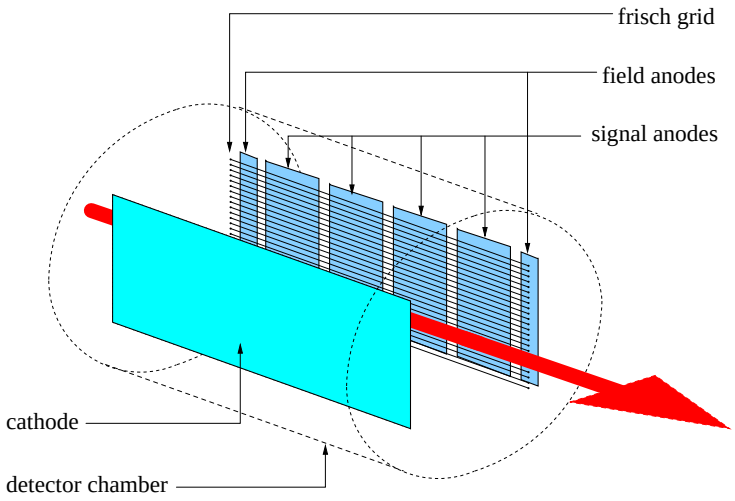

Figure 2.6: Schematic view of an ionisation chamber. The ionisation chamber located at S2 was 40 cm thick filled with CF_4 gas, while the MUSIC located at S4 was 60 cm thick filled with P10 gas (90%Ar+10%CH_4).

The energy-loss of charged particles in a material is, in first order Born approximation, given by the Bethe formula (equation 2.1). Where s is the path length traveled by the particle in the material, Z is the atomic number of the particle, m_e is the electron mass at rest, c is the speed of light, β is the speed of the particle in c units, e is the electron charge, Z_0 is the atomic number of the material, A_0 is the mass number of the material, and L is the so-called *stopping number*.

$$\frac{dE}{ds} = -\frac{4\pi Z^2}{m_e c^2 \beta^2}\left(\frac{e^2}{4\pi\epsilon_0}\right)^2 Z_0 N_0 L \tag{2.1}$$

The stopping number is defined in equation 2.2, where E_{max} (see equation 2.3) is the maximum energy which can be imparted to an electron in a collision, and I is the mean excitation energy of the material (in this case the corresponding gas at normal pressure and room temperature).

$$L = ln\frac{E_{max}}{I} - \beta^2 \tag{2.2}$$

$$E_{max} = \frac{2m_e c^2 \beta^2}{1-\beta^2} \tag{2.3}$$

An ionisation chamber does not measure the energy-loss, but the ionisation in the gas, relative to the energy deposition. The difference between the energy-loss and the energy deposited inside the detector is due to the production of δ-rays (energetic electrons) in close proximity of the particle with the gas. If the δ-rays leave the detector, the deposited energy will be less than the energy-loss. A simple approximation for this effect, described in [Pfu94, Hli98] and known as *truncated Bethe-Bohr model*, modifies slightly the stopping number (see equation 2.4) by using the restricted energy-loss E_d, which is an empirical parameter that depends on the dimensions of the absorber.

$$L' = \frac{1}{2} ln\frac{E_{max}E_d}{I^2} - \beta^2 \tag{2.4}$$

It is now possible to substitute and integrate to obtain the energy deposited in the detector:

$$\Delta = k\frac{L'}{\beta^2} \tag{2.5}$$

With $k = \frac{4\pi Z^2 s}{m_e c^2}\left(\frac{e^2}{4\pi\epsilon_0}\right)^2 Z_0 N_0$.

In order to calibrate the ionisation chambers we used the primary beam, with four different reference velocities. These different velocities were achieved by slowing down the primary beam with carbon targets of different well known thicknesses at the entrance of the FRS. The different velocities were evaluated with the ATIMA code [ATIMA]. We fitted the data recorded at the ionisation chambers to the equation 2.5. This allows us to calibrate both detectors. The results of these calibrations are shown in figure 2.7. The IC energy resolution was better than the energy resolution of the MUSIC, as will be shown in figure 3.2.

2.3.2.2 Time projection chambers

A Time Projection Chamber (TPC) [Bau96, Hli98] is an ionisation detector working in the *proportional* region. An ionizing particle passing through the detector creates a shower of electrons along its track. These electrons drift towards the anode wires because of the uniform electric field (the drift time gives us the y

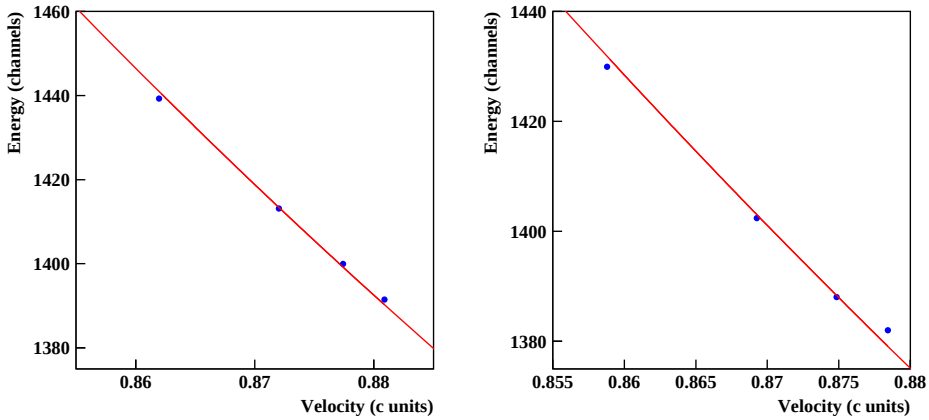

Figure 2.7: Calibration of the ionisation chambers with argon primary beam, by adjusting equation 2.5 to four points obtained from four different reference velocities of the primary beam. Left panel: Calibration of the IC located at $S2$. Right panel: Calibration of the MUSIC located at $S4$.

coordinate information) and once they approach the wires they are accelerated under the effect of a radial electric field. The acceleration causes a maximum atomic ionisation, producing a large shower of localized negative charge near the anode, which is reflected as positive in the delay line. The positive charge in the delay line produces a pulse. The time needed to collect the pulse can be used to deduce the x position. From the x and y position measurement in two different detectors we can also deduce the angle.

We used six TPC's for the **tracking** of the projectiles and fragments (see figure 2.3). TPC's **1** and **2** were located before the target at $S2$, while TPC's **3** and **4** were located behind it. TPC's **5** and **6** were located at $S4$.

The TPC's we used are P10 gas (90%Ar, 10%CH_4) filled detectors operating at normal pressure and room temperature. They have four anodes and one cathode. The anodes are wires, and have a "delay line" just below them (see figure 2.8).

These detectors have an x and y position resolution better than $0.5\ mm$ and a very small amount of matter in the beam path, which minimizes the angular straggling.

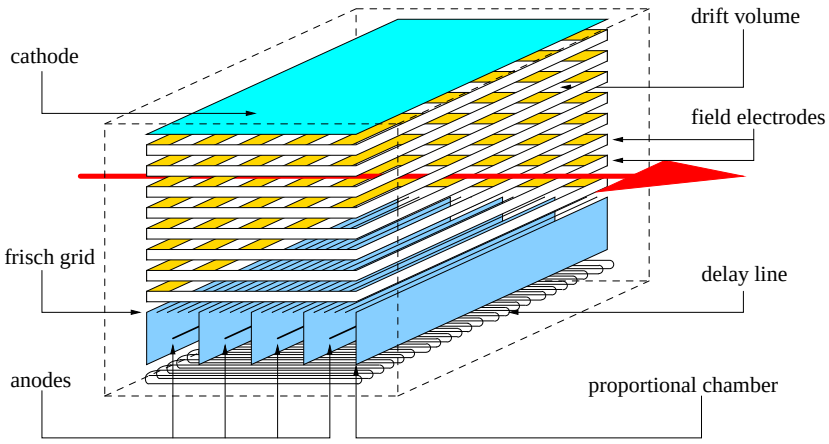

Figure 2.8: Schematic view of a time projection chamber. It is a detector 7 cm thick filled with P10 gas (90%Ar+10%CH_4). An ionizing particle passing through it creates a shower of electrons along its track. These electrons drift towards the anode wires because of the vertical uniform electric field (the drift time gives us the y coordinate information) and once they approach the wires they are accelerated under the effect of a radial electric field. The acceleration causes a maximum atomic ionisation, producing a big shower of localized negative charge near the anode, which is reflected as positive in the delay line. The positive charge in the delay line produces a pulse. The time needed to collect the pulse can be used to deduce the x position.

The calibration of the TPC's was done with primary beam, in six settings (one for each TPC). In each setting we placed a grid in front of the corresponding TPC. The grid partially stopped the beam at certain physical x and y positions. The TPC recorded a spectrum that presented holes at different positions (see figure 2.9). The calibration was done by matching the position of the holes at the spectrum to the physical ones.

An example of the tracking information that could be obtained with those detectors is presented in figure 2.9 for the particular case of ^{22}O. These position detectors allow us to obtain a very accurate measurement of the magnetic rigidity (Bρ) of each ion (event-by-event basis) if we know the magnetic rigidity of the reference particle for the current setting.

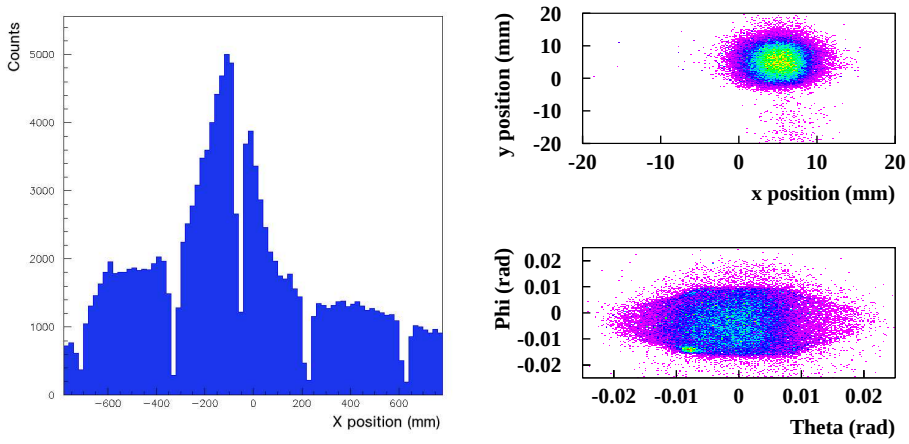

Figure 2.9: Left panel: TPC's position calibration. A grid was placed just in front of the TPC for calibration purposes. It absorbed part of the beam at certain positions (see this at the spectrum). Right panel: profile and angular distribution of the beam at the breakup target. Theta is the angle in the x direction and phi is the angle in the y direction.

2.3.3 Scintillators

A scintillation detector [Leo93] has two important components: the scintillator and the photo-multiplier. The scintillator works by excitation of its atoms and molecules when some radiation passes through it, and subsequent de-excitation by visible (or near-visible) light emission (this process can take a certain time which defines the response velocity of the scintillator). Further amplification of the light produced is done at the photo-multiplier by generating electrons at the cathode by photo-electric effect. These primary electrons are multiplied inside the tube (a typical gain is 10^6) generating a large amount of electrons that hit the anode and give rise to an electric pulse proportional to the amount of energy deposited in the crystal. This means that scintillation detectors should have a linear stable response with energy.

In the experiment two types of scintillation detectors were used: the plastic scintillators and the array of NaI(Tl) crystal scintillators.

2.3.3.1 Plastic scintillators

Plastic scintillators [Vos95] were used as timing detectors, measuring the speed of the particles passing through the FRS by using time difference and space separation information. The time difference information is usually referred to as

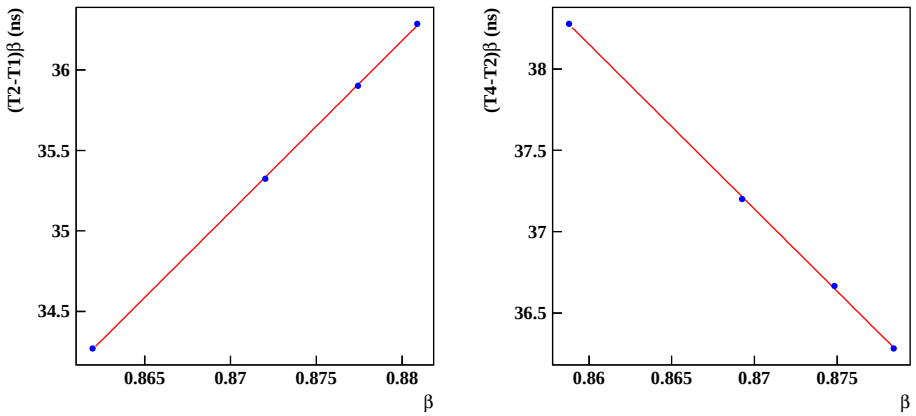

Figure 2.10: Fits used to calibrate the $11R - 21R$ (left) and $21R - 41R$ (right) time difference for the trigger used to measure the cross-sections. In the first case, $21R$ gives the start signal (for valid events) while $11R$ gives the stop signal (for the time difference). The delay introduced in the S1 scintillator signal to make it fall inside the accepted events window causes the time difference multiplied by β to increase with β. In the second case, $21R$ gives the start signal and $41R$ gives the stop signal. The opposite behaviour appears in this plot, because the S2 scintillator is delayed in such a way that the signal of the S4 scintillator can fall inside the accepted events window opened by S2 (without that delay the signal at the S4 scintillator would appear too late).

Time of Flight (ToF) and we will follow this convention. They were also used to **generate the two triggers used in the experiment**. We have used three scintillators made of BC420 plastic located at S1, S2 and S4. The thicknesses of the detectors at S1 and S2 were $3\ mm$ each, while the scintillator at S4 was $5\ mm$ thick. Each plastic scintillator was connected to two photo-multipliers (left and right side) to improve the time resolution and to give optional position information as well.

We used two triggers in order to achieve the best measurement conditions for certain observables:

The first trigger used the signal provided by the plastic scintillator at **S4** as a *start*. This trigger was used for the **core fragment longitudinal momentum distribution** measurements, and also for the **coincidence** with the γ rays emitted by the de-exciting core fragments, because it *filtered* all the events that were not able to reach S4. In order to measure **cross-sections** a different trigger,

provided by the scintillator located at **S2**, was used.

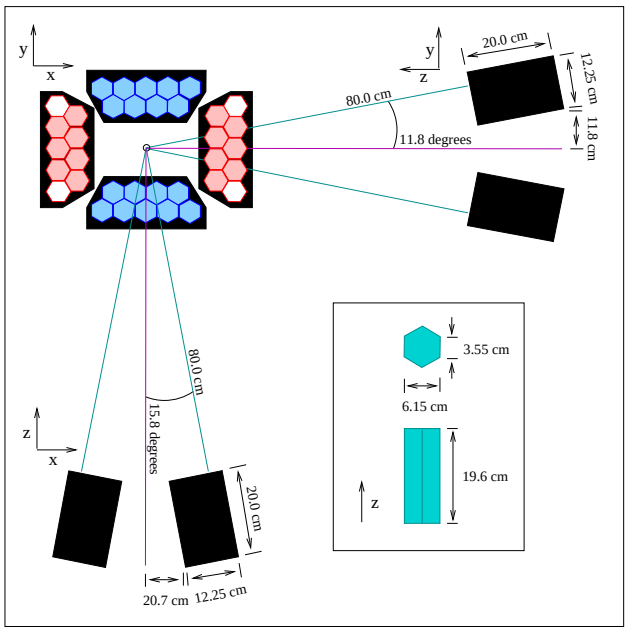

Figure 2.11: The NaI array was made up of 32 individual NaI crystals (shaded hexagons in the figure), the dimensions of each one are given in the inset (bottom, right). Three main views are represented: front view (top, left); side view (top, right); top view (bottom, left).

A calibration was needed to obtain the equivalence between $\mathrm{ToF}\ (ns)$ for the different $11L-21L$, $11R-21R$, $21L-41L$ and $21R-41R$ signals, and speed in **c** units (β) of the isotope (to clarify the notation we show an example: $21L$ stands for the left photomultiplier signal of the scintillator located at S2). This calibration was done by fitting $\mathrm{ToF}\beta\ (ns)$ vs. β, for the four velocities already used in the ionisation chambers calibration. The calibrations of the $11R-21R$ and $21R-41R$ ToF's are shown in figure 2.10 as an example, in the case of the trigger used to measure the cross-sections.

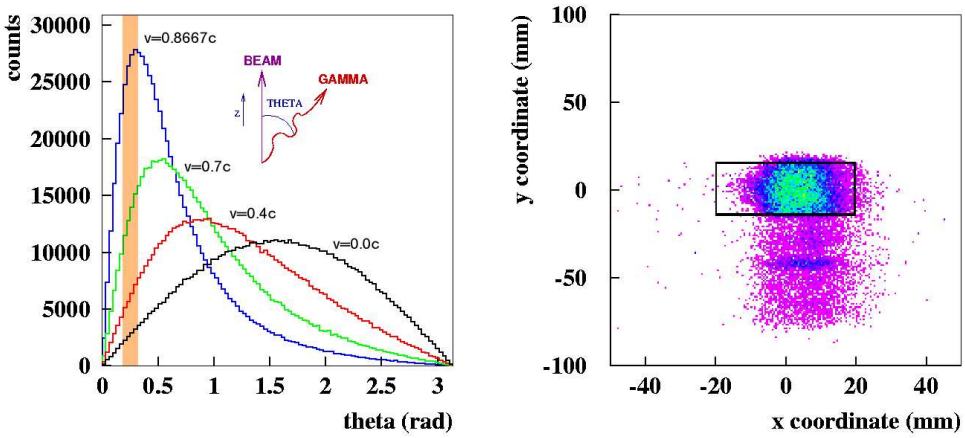

Figure 2.12: Left panel: Variation in the angular distribution with respect to the beam direction of the γ rays emitted by a moving source at different velocities. All the curves have the same area. Under the conditions of the experiment ($\sim 1\ AGeV$, β=0.8667) the maximum is found around 0.3 radians. The shadowed area signifies the fraction of the distribution covered by the NaI array. θ is the γ-ray emission polar angle with respect to the beam. Right panel: The beam as it is seen by the NaI crystals array. The picture is obtained by extrapolation to the array position of the beam image with the third and fourth TPC's (located before and after the NaI scintillators). The size of the beam justifies the dimension of the "hole" in our array (shown as a square in the plot). As an example, in the case of ^{22}O obtained after one-neutron removal from ^{23}O on a carbon target, the array stops only around 1% of the ^{22}O core fragment flux (result which has been obtained with a MOCADI simulation).

2.3.3.2 NaI scintillators array

For the measurement of the γ **rays emitted by the core fragments** after one nucleon removal we used a NaI scintillators array [Wan99, Fer01] shown in figure 2.11. It consists in 32 hexagonal NaI crystal detectors, disposed parallel and forming a "ring" around the beam axis. The array was located juse $80\ cm$ after the target at S2.

The setup was designed to cover the largest solid angle for the γ rays emitted by the fragments. The angular distribution of the emitted γ rays with respect to the beam axis was peaked forward, due to the high energy, in the polar angle at approximately 16 degrees ($\approx 0.3\ rad$) as can be seen in figure 2.12 -left-. The

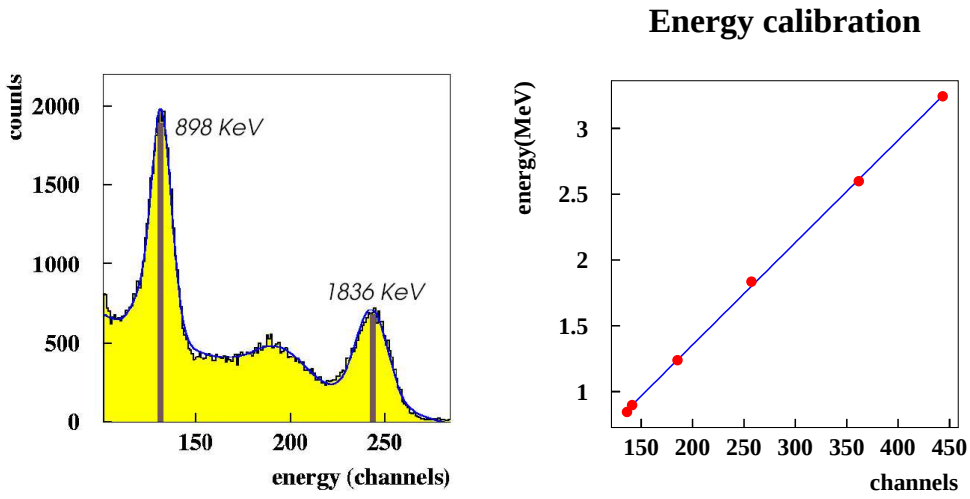

Figure 2.13: Plots showing the two steps in the energy calibration of the NaI array using sources at rest. Left panel: First we placed different sources in front of the array and recorded the corresponding energy spectra (the example is for ^{88}Y and a single detector), and determined the position of the peaks in channels, relating them to the energy of the corresponding emitted γ rays. Right panel: Then we made a fit "Energy vs. Channel position" to obtain the energy calibration. The dependence is linear.

NaI crystals were placed at this angle forming a "ring" around the beam, trying to get an equilibrium between avoiding the beam and having the biggest possible geometric efficiency (see figure 2.12 -right-).

Low energy γ rays coming from the background [Wan99, Hol92] could disturb our measurement. The amount of background γ rays is proportional to the charge of the target and projectile and could be of relative importance up to energies of around $500\ keV$. In order to reduce those background γ rays we placed a shielding in front of the NaI crystals consisting of one layer of aluminum ($2.0\ mm$ thick) and two layers of lead (each one $1.0\ mm$ thick). These two materials have high interaction cross-sections for low energy γ rays and thus the mean free path for the γ rays in those materials is low. In consequence, $4.0\ mm$ were enough to reduce their intensity to an acceptable level for our purpose. As the emitted γ rays during the experiment are strongly Doppler shifted due to the high velocity of the emitter fragments ($\beta \simeq 0.8667$), their energies, as seen by the detectors, are expected to be much higher than $1\ MeV$. This is not the case for the background γ rays, which do not suffer any Doppler shift and remain with low energy. With the aluminum and lead layers, the ratio between the number

of γ rays before and after attenuation for γ rays of $10\ keV$ is around 10^{-96} and for γ rays of $100\ keV$ is of the order of 10^{-9}, but for γ rays of $1\ MeV$ it is 0.8. In this way we obtain the desired reduction of low energy γ rays, keeping the intensity of the high energy ones.

The main information obtained with this array is the energy released in each individual NaI crystal per event, and the time at which the event took place, having as start signal for the time information the plastic scintillator located before the breakup target.

The energy calibration was done with different sources at rest [Fer01] (^{88}Y and ^{56}Co) in order to cover the maximum energy range available, because during the experiment we were expecting γ rays with energies up to $6.2\ MeV$. The calibration (shown in figure 2.13) was done separately for each crystal.

Chapter 3

Data analysis

In this chapter we will describe the procedure followed in order to get the experimental observables from measurements performed with the detectors.

First we will define some notation that will be used in the rest of the work:

- we will call primary beam to the ^{40}Ar beam accelerated by SIS
- the (exotic) projectiles are the fragments generated by nuclear fragmentation of the primary beam in a (production) target located at the entrance of the FRS and transmitted to S2, where they interact with a breakup target
- the (core) fragments are the heavy residues produced after the breakup reaction of the exotic projectiles in the S2 target

$^{17-21}$N, $^{19-24}$O and $^{22-27}$F isotopes were produced by fragmentation of a primary beam of ^{40}Ar which impinges on a beryllium target of $6.333\ g/cm^2$ located at the entrance of the FRS at an energy of $1.035\ AGeV$. The intensity of the primary beam ranged between $10^9 - 10^{10}$ particles per spill at *8 seconds* repetition rate.

The first half of the FRS was set to the magnetic rigidity ($B\rho$) value of the $^{19-24}$O isotopes. This was accomplished in different settings trying to get the best transmission for the selected oxygen isotopes. The FRS momentum acceptance ($\pm$1%) allowed the transmission of other nuclei with close $B\rho$ values: $^{17-21}$N and $^{22-27}$F. All these isotopes were completely identified with respect to A and Z.

Three different kinds of reactions were studied for these isotopes:

- one-neutron removal (1n-removal) reactions using a carbon breakup target at S2

- two-neutron removal (2n-removal) reactions using a carbon breakup target at S2

- 1n-neutron removal reactions using a lead breakup target at S2

Behind the S2 breakup target the magnetic fields were set to select the 1n-removal products: $^{16-19}$N, $^{18-22}$O and $^{21-25}$F (from $^{17-20}$N, $^{19-23}$O and $^{22-26}$F), and the 2n-removal products: ^{19}N, ^{22}O and ^{25}F (from ^{21}N, ^{24}O and ^{27}F). They were completely identified with respect to A and Z as well.

3.1 Mass and charge identification

The identification in A and Z was accomplished in an event-by-event basis. The time-of-flight was measured by the plastic scintillators located at S1, S2 and S4. The magnetic rigidity of each particular ion was determined from position measurements in position-sensitive time projection chambers (TPC's), and the magnetic field provided by a *Hall* probe. The atomic number was deduced from the energy deposited in multiple sampling ionisation chambers (IC and MUSIC). In figure 3.1 we have plotted schematically all the observables needed for the identification of the fragments (S2-S4 section of the FRS).

The reduced size of the plastic scintillator located at S1 ($\pm 1\ cm$ in x) made necessary the use of slits just before it. This consequently reduced the size and intensity of the secondary beam.

The timing information provided by the plastic scintillators was used to measure the time needed by the produced nuclei to pass through the FRS, or Time of Flight (ToF). This was done for projectiles (nuclei before the breakup target) by measuring the ToF between the first scintillator (located at the first focal plane of the FRS) and the second scintillator (located at the intermediate focal plane of the FRS), and for fragments (nuclei after the breakup target) measuring the ToF between the second scintillator and the third one (located at the final/fourth focal plane of the FRS). We used plastic scintillators as timing detectors because of the fast rise time of the light pulse produced when charged particles pass through the plastic material. The speed is obtained by dividing the length of the path followed by the nucleus between two plastic scintillators by

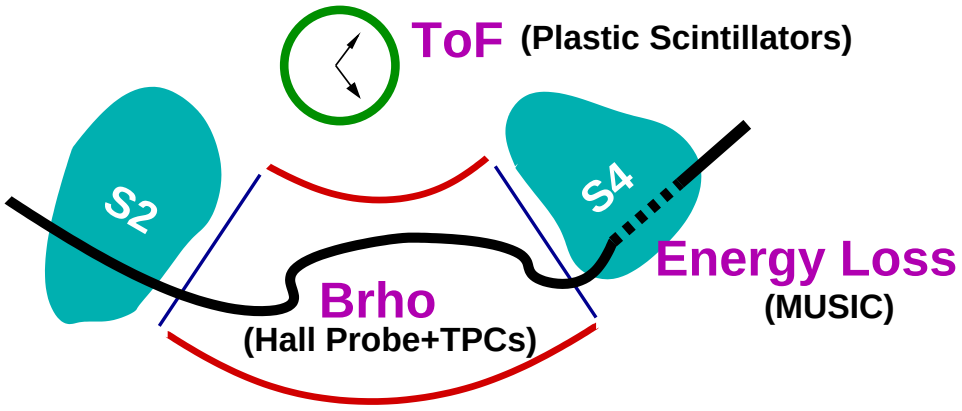

Figure 3.1: Schematic representation of the observables needed for the identification of the different nuclides in Z and A/Z. The example is for the S2-S4 part of the FRS. The time of flight (ToF) is measured with the start and stop signals that provide the plastic scintillators located at S2 and S4. The magnetic rigidity ($B\rho$) is obtained from the magnetic rigidity of the reference particle for the current setting and specific measurements of the position of the ion with respect to the reference particle (information given by the TPC's). Finally, a MUSIC detector located in this case at S4 measures the energy deposited by the ions that pass through it. From the ToF we obtain the speed of the ions (β), which together with the $B\rho$ gives the A/Z. The β combined with the *deposited energy* measurement gives the atomic number (Z).

the ToF measured with the same scintillators.

The magnetic rigidity of a particular nucleus was obtained from the equation 3.1 (see [Bau99]).

$$B\rho = \frac{D_f + x_{S4} - (x|x)_f \cdot x_{S2}}{D_f} \cdot B\rho_0 \tag{3.1}$$

In this equation, D_f is the dispersion from S2 to S4 that the FRS induces in the fragments, x_{S2} and x_{S4} are the positions of the nucleus at the focal planes at $S2$ and $S4$, respectively, $(x|x)_f$, called magnification, is defined at first order as the variation in the position of the particle at the focal plane S4 with respect to the variation in the position of the reference particle at the same focal plane, and $B\rho_0$ is the magnetic rigidity of the reference particle. D_f and $(x|x)_f$ are theoretical values, and $B\rho_0$ is calculated multiplying the magnetic field measured with a Hall probe and the efective radius of the reference trajectory.

Once the value for the speed of the nucleus and its magnetic rigidity ($B\rho$) are known, the *mass number over atomic number* ratio (A/Z) can be deduced

using the expression 3.2.

$$A/Z = \frac{B\rho e}{\beta c \gamma u} \tag{3.2}$$

In this equation e is the electron charge, β is the speed of the nucleus in c units, γ is the Lorentz factor and u is the atomic mass unit. If in addition we know Z (from the *deposited energy measurement obtained with the corresponding* MUSIC and the β substituted in equation 2.5), the unambiguous projectile/fragment identification is possible. In figure 3.2 we show an example, where we can observe that the resolution in Z was better for projectiles due to the better performance of the IC placed at S2 compared with the MUSIC at S4. In another hand, the A/Z resolution was better for fragments due to the larger distance between the scintillators, thus giving better TOF resolution.

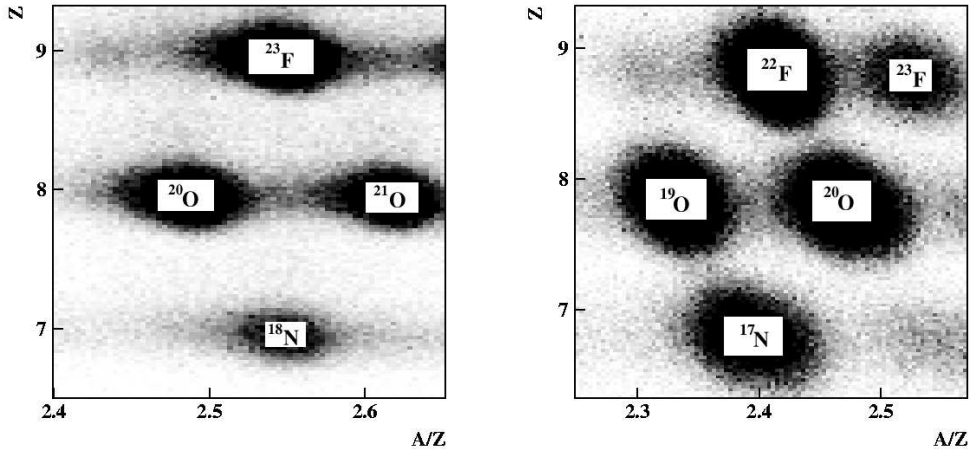

Figure 3.2: Typical identification spectra obtained from measurements in MUSIC detectors, plastic scintillators, TPC's and Hall probes. Left panel: Identification of projectiles (S1-S2 part of the FRS). Right panel: Identification of fragments (S2-S4 part of the FRS).

3.2 One- and two-neutron removal cross-sections

The one- and two-neutron (1n, 2n) removal cross-sections were determined with the number of projectiles before (N_0) and the number of fragments (N) after the corresponding reaction, by using the formula:

$$N = N_0 \cdot e^{-\sigma n t} \tag{3.3}$$

Where σ is the cross-section, n is the atomic density of the target, and t is the thickness of the target.

In order to obtain accurate values for the measurements of N_0 and N it is important to use very efficient detectors. Ionisation chambers, TPC's, and plastic scintillators fulfilled this requirement and were used in the measurements. One ionisation chamber, two TPC's, and one plastic scintillator located just in front of the breakup target (see figure 2.3) were used to identify the projectiles and count them in the case of the 1n-removal cross-sections. Unfortunately we had not proper detectors located just behind the target. It was therefore necessary to use the detectors at the focal plane S4 to obtain the number of core fragments emerging from the corresponding reactions. Note that there are transmission losses between S2 and S4, and secondary reactions can take place in the breakup target itself and any layer of matter in the fragments path between S2 and S4. These two effects reduce the number of fragments that arrive at the scintillator at S4, and had to be taken into account.

The transmission of the fragments through the FRS was calculated with the ion-optical ray-tracing code MOCADI [Iwa97, MOCADI]. This Montecarlo simulation accounts for secondary reactions in the breakup target as well. In order to ensure that the simulation fitted as much as possible the reality, the shapes of the simulated position distributions (in x and y) evaluated at the position of the six TPC's used in the experiment were adjusted to the measured ones. The transmission of non-centered isotopes (for example, the nuclide ^{22}O) was calculated with the simulation adjusted to the reference isotope (in the example that we are considering, the nuclide ^{23}O), which was centered. The relative error that we introduce evaluating the transmission with MOCADI is estimated to be around 10%. The transmission evaluated for the different isotopes is shown in table 3.1.

We have not corrected for secondary reactions out of the breakup target. We have estimated that the error they introduce in the cross-section measurement is small and falls inside the error contribution of the MOCADI simulation.

Contaminations from other breakup channels are excluded by the double identification and by the large change in $B\rho$ between the two magnetic stages of the FRS of more than 9 % (in the case of the ^{23}O going to ^{22}O), which is well outside the FRS acceptance of $\Delta B\rho \simeq 1\%$.

Table 3.1: Transmissions of the different fragments (first 23 entries) and projectiles (last 3 entries) necessary to obtain the cross-sections, determined with MOCADI. In the table, "fragment" refers to the core fragment emerging from the one-neutron removal on carbon (first fourteen entries), one-neutron removal on lead (next six entries), and two-neutron removal on carbon (following three entries). "Projectile" refers to the exotic projectile produced at the entrance of the FRS ($S0$), where the SEETRAM is located. The last three entries of the table refer to the projectiles of the two-neutron removal reactions on carbon (note that with two-neutron removal reactions we need to know the transmission between $S0$ and $S2$, and between $S2$ and $S4$).

Fragment	N_{S4}/N_{S2} (%)	$\Delta(N_{S4}/N_{S2})$ (%)
^{16}N	72.5	7.2
^{17}N	73.5	7.4
^{18}N	76.9	7.7
^{19}N	74.6	7.5
^{18}O	71.9	7.2
^{19}O	73.5	7.4
^{20}O	75.2	7.5
^{21}O	76.9	7.7
^{22}O	77.5	7.8
^{21}F	75.8	7.6
^{22}F	75.8	7.6
^{23}F	78.7	7.9
^{24}F	80.6	8.1
^{25}F	80.6	8.1
^{18}N	62.1	6.2
^{19}N	64.1	6.4
^{21}O	67.6	6.8
^{22}O	66.7	6.7
^{24}F	69.4	6.9
^{25}F	69.4	6.9
^{19}N	68.0	6.8
^{22}O	77.5	7.8
^{25}F	79.4	7.9
Projectile	N_{S2}/N_{S0} (%)	$\Delta(N_{S2}/N_{S0})$ (%)
^{21}N	9.9	0.9
^{24}O	12.5	1.2
^{27}F	15.2	1.5

With respect to the 1n-removal cross-sections, corrections for acquisition dead time were not necessary because the measurement of the number of particles at S4 requires that they come from valid projectiles at S2. If one particle reaches S2, it triggers. Due to the existing dead time it can be accepted for registering its information in the detectors or not. If it is accepted, and the identification confirms that it is a valid projectile the action passes to S4. The very low dead time at S4 compared to the one at S2 implies that the effective dead time at S4 will be mainly the dead time at S2. The effect of both dead times cancels when we calculate the cross-section.

With respect to the 2n-removal cross-sections, we did not have measurements with the trigger given by the plastic scintillator at S2, but only by the plastic scintillator at S4. This means that the detectors at S1 and S2 only registered events that reached S4 (only valid projectiles that led to valid fragments). The only one detector able to give the total number of valid projectiles was the SEETRAM, because it integrated the primary beam over each pulse (or *spill*). The SEETRAM counted the number of ^{40}Ar nuclei that entered the FRS. As the production cross-sections of ^{21}N, ^{24}O and ^{27}F from ^{40}Ar on a beryllium target are known, we can calculate the number of exotic projectiles at $S0$, and using the transmission estimated with MOCADI it is possible to determine the number of ^{21}N, ^{24}O and ^{27}F reaching S2. In this case we had to correct by dead time the number of counts at S4: the ratio between the processed and the total valid events was ~ 97 %.

3.3 Momentum distributions of core fragments

3.3.1 Position measurements

The position distributions of the core fragments measured at the focal plane S4 were used to obtain their corresponding momentum distributions.

Two TPC's (5 and 6) were needed to determine the trajectory of the core fragments (position and angle). These two observables allowed us to obtain by extrapolation the transversal location (x and y) of the core fragment at any z-position.

To measure the correct x-position of the core fragments at S4 we have to detemine the z-position of the image focal plane. The x-position distribution is

narrowest at the image focal plane (see [Bau99] for a detailed discussion). Using this information, and plotting the Full Width at Half Maximum (FWHM) of the x-position distribution as a function of z, the z-position of the image focal plane was determined experimentally for each setting, and was found to be around $2\ m$ after the last FRS quadrupole for all nuclides.

Once the z-position of the image plane is known, we can evaluate the correct fragment x-position distribution by projecting it till this point using the information given by TPC's 5 and 6 (figure 3.3). The y-distribution at the same z-position is also shown.

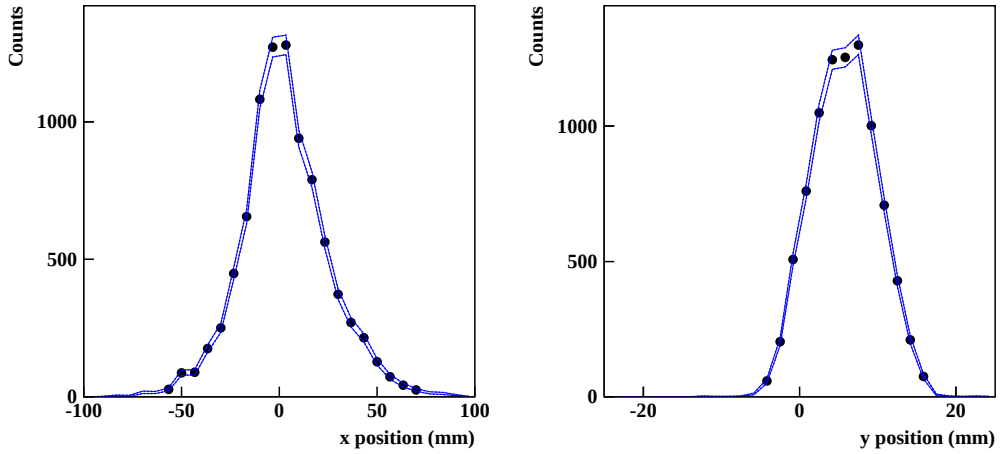

Figure 3.3: Example position distributions of ^{22}O fragments coming from ^{23}O at the focal plane S4 obtained with the TPC's 5 and 6. Left panel: x-position distribution. Right panel: y-position distribution. The lines delimit the error interval.

3.3.2 Longitudinal momentum distribution

In order to obtain the fragment longitudinal momentum distribution we used the FRS in its energy-loss mode [Bau99], in which the momentum change in the middle focal plane S2 (where the breakup target is) is translated into a change in x position in the final focal plane S4.

The momentum change in the breakup target can be due to two causes:

- The change of isotope in the reaction due to the one neutron loss

- The energy loss in the breakup target

This momentum change, in the laboratory reference frame, can be expressed as:

$$\Delta p_{S2} = eZ_f B\rho_0 \cdot \frac{x_{S4}}{D_f} \tag{3.4}$$

In this equation e is the electron charge, Z_f is the atomic number of the fragment, $B\rho_0$ is the magnetic rigidity of the reference particle, x_{S4} is the position of the nucleus at the focal plane S4, and D_f is the dispersion that the FRS induces in the fragments.

In order to obtain this momentum change in the center of mass of the projectile we need to perform a Lorentz transformation. The first step is to know the total momentum, obtained by adding the momentum of the reference particle in the second stage of the FRS to the momentum change:

$$p_{S2} = p_0 + \Delta p_{S2} = eZ_f B\rho_0(1 + \frac{x_{S4}}{D_f}) \tag{3.5}$$

If Z_f and $B\rho_0$ are known, to measure the core fragment longitudinal momentum distributions we still need to evaluate the dispersion in the second stage of the FRS, and to measure the x-position distribution in the experimental z-position of the image focal plane at S4 (see section **3.3.1**). These two tasks are acomplished with the help of the TPC's.

Equation 3.5 corresponds to the ideal case in which all the core fragments produced at the breakup target come from projectiles whith identical momentum: the one of the reference particle in the first stage of the FRS. We must still remember that there is a slowing down inside the breakup target caused by the energy loss of the projectile before the reaction and the one of the fragment after it. Depending on where the reaction at the breakup target took place, the slowing down will be different. We call this effect "Location Straggling" and it is due to the fact that the energy loss is different for the projectile and the fragment. This location straggling induces an extra broadening of the momentum distribution at S4 which must be taken into account (see figure 3.4 -left-).

Another contribution to the resulting fragment momentum distribution is the intrinsic resolution introduced by the setup itself. In order to take it into account, we analyzed for each reaction an additional setting in which, after the target, the projectiles that did not react were transmitted to the final focal plane and their corresponding momentum distribution was obtained. This contribution had to

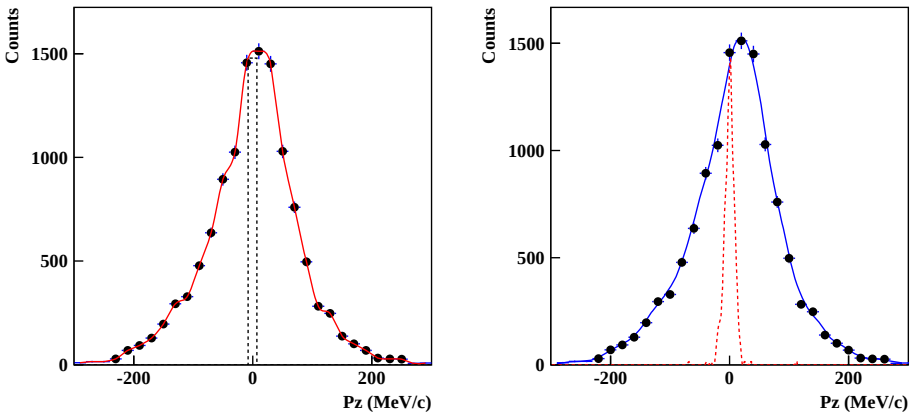

Figure 3.4: Left panel: contribution of the location straggling to the momentum distribution of ^{22}O (core fragment after breakup from ^{23}O): the dashed histogram represents the difference in energy loss in the target between the projectile and the fragment. The convolution of this effect and the experimental points gives the solid curve. It can be seen that the effect of the location straggling is negligible. Right panel: contribution of the intrinsic resolution introduced by the setup to the momentum distribution of ^{22}O (core fragment after breakup from ^{23}O): the convolution of the experimental points and the intrinsic resolution (dashed curve) gives the solid curve, which is slightly broader than the initial distribution.

be subtracted for each setting, either deconvoluting the experimental momentum distribution with the intrinsic resolution or using the width of these distributions assuming a *Gaussian* shape and applying the formula 3.6 (see figure 3.4 -right-, and [Bau99] for more details).

$$FWHM = \sqrt{FWHM_p^2 - FWHM_i^2} \tag{3.6}$$

The formula 3.6 is only valid for *Gaussian* profiles. We have checked and observed that the contribution of the intrinsic resolution to the momentum distribution of the core fragment was negligible in our case with non-*Gaussian* shapes.

Once the core fragment longitudinal momentum distribution in the laboratory refence system (p_{S2}) has been evaluated, we can obtain the corresponding longitudinal momentum distribution in the moving frame of the projectile before the breakup reaction (p_z) by using equation 3.7.

$$p_z = \gamma_p \cdot (p_{S2} - \beta_p E_f) \tag{3.7}$$

Where γ_p is the Lorentz factor of the projectile, β_p is the speed of the projectile in c units, and $E_f = \sqrt{p_{S2}^2 + (A_f u)^2}$ the energy of the fragment, being A_f the mass number of the fragment and u the atomic mass unit.

3.3.3 Transversal momentum distributions

The transversal components of the core fragment momentum distribution at the laboratory reference frame can be obtained from the longitudinal momentum distribution and the angle of emission of the fragments in x and y directions measured just after the breakup target (see figure 3.5). We use TPC's 3 and 4 to obtain this angle. From the tangent of this angle we obtain the ratio between the transversal and the longitudinal component of the fragment momentum distribution.

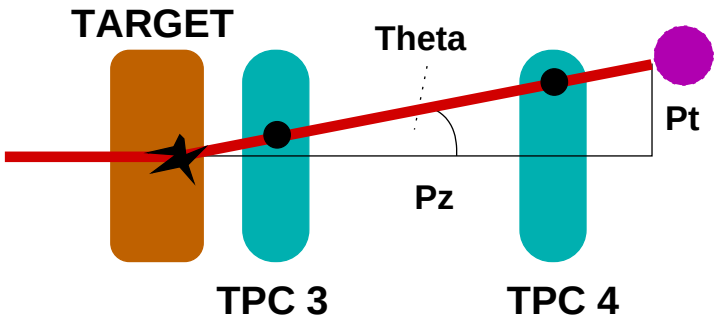

Figure 3.5: Schematic representation showing how to calculate the transversal component (x or y) of the momentum distribution of the fragment. Once we know the longitudinal component at the laboratory reference frame (P_z), we can obtain the transversal one (P_t) by multiplying by the tangent of the angle (in x or y) of emission of the fragments just after the reaction ($Theta$).

In case that the transversal components are much smaller than the longitudinal one, which is specially true in our situation (**in the laboratory reference frame**), the tangent can be approximated by the angle itself. The transversal components of the momentum are not affected by the lorentz transformation since the speed of the ions is very strongly peaked forward and can be considered to have only longitudinal component. This means that the distributions of the transversal components in the laboratory reference frame are the same as the components in the center of mass reference frame.

The intrinsic resolution of the FRS for the transversal components is calculated from the longitudinal component. This is done in the same way as the transversal core fragment momentum distributions are calculated from the corresponding core fragment longitudinal momentum distribution.

3.4 γ-ray spectra

The detection of γ rays emitted by the different fragments was performed by means of the NaI array presented in section **2.4.3.2**. We will discuss now different considerations necessary to obtain a "proper" γ-ray spectrum with minimized background.

We will present in detail the particularities introduced when we performed in-beam γ-ray spectroscopy with relativistic sources.

3.4.1 Energy information

The energy information recorded in each crystal of the array is used to obtain the energies and the number of detected γ rays. In the case of emission by sources moving at relativistic energies the energy information is obviously Doppler shifted and we need to apply a Doppler correction to obtain it in the center of mass system of the core fragment. The Doppler correction must be made taking into account the angular position of the NaI crystal with respect to the emitter direction. Unfortunately, there is an uncertainty in this measurement due to the opening angle of the NaI γ-ray detector (approximately 4.5 degrees in the setup used in our experiment), since these detectors are not punctual. However, we must treat them as punctual and, following this approach, we conventionally define their position at the center of their volume. This is the origin of the Doppler broadening that cannot be corrected. We try to show how this effect affects the γ-ray spectrum in figure 3.6.

In order to proceed with the Doppler shift correction we assume that all excited fragments de-excite via γ rays inside the target. Gamma emission is a very fast process [Kan95] (of the order of 0.1 ns) and at velocities of β=0.8667, at $10\ cm$ from the breakup point (the distance between the target and the array is $80\ cm$) only ~ 13 % of the excited fragments remain.

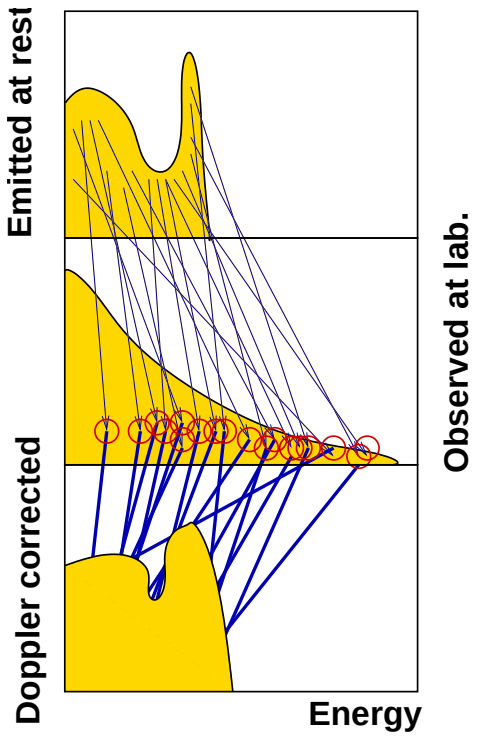

Figure 3.6: Top: schematic representation of how the original γ-ray energy spectrum should be recorded if the emitters were at rest. Center: representation of how the spectrum is observed in the laboratory reference system (emitters not at rest, different Doppler shift for NaI scintillators at different angular positions, Doppler broadening and other minor effects also contribute to make the shape different). Bottom: representation of how is the spectrum that we get after applying corrections (Doppler shift correction with add-back and multiplicity) to the one observed in the laboratory reference frame. The differences observed between the third spectrum and the first one are due to the contributions that could not be corrected (mainly Doppler broadening), and are represented by circles of imprecision at the second spectrum.

Once the spectra of all the individual crystals have been corrected of Doppler shift they can be added to get the total energy spectrum for the array. This procedure is quite simple if the γ ray leaves all the energy in the first hit NaI scintillator. If this is not the case an additional treatment (add-back procedure and multiplicity control) must be done (these points will be discussed later).

The Doppler broadening mainly affects the energy resolution. If the energy resolution is too low we will not be able to experimentally distinguish between γ transitions of similar energy.

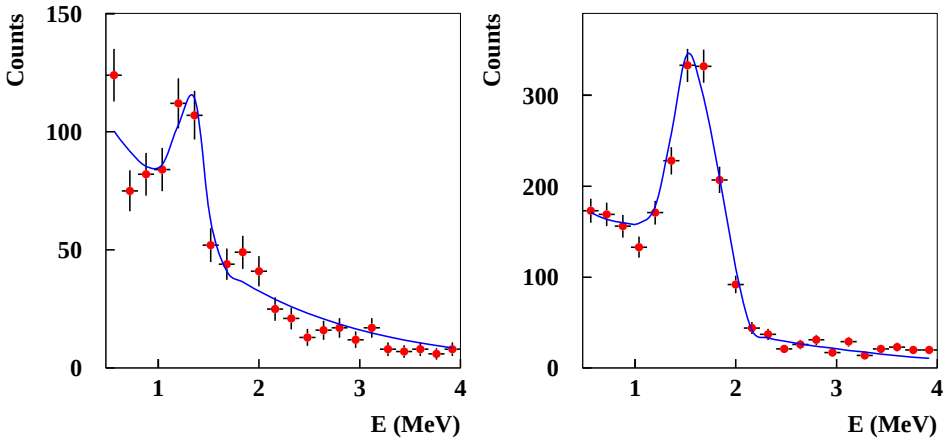

Figure 3.7: Energy spectra obtained for the γ rays emitted by ^{17}N (left) and ^{20}O (right), nuclides produced at the breakup target after one-neutron removal from ^{18}N and ^{21}O, respectively. In the case of the ^{17}N the peak is centered at approximately $1.3\ MeV$ with a FWHM of around $0.3\ MeV$ and is due to one γ ray of around $1.4\ MeV$, while for the ^{20}O the peak is centered at approximately $1.6\ MeV$ with a FWHM of around $0.5\ MeV$ and is made of **two** γ rays of 1.6 and $1.9\ MeV$, which accounts for the difference in the FWHM of both peaks.

Figure 3.7 shows the energy spectra of ^{17}N and ^{20}O obtained with our NaI array, after Doppler correction. Both spectra present one peak, centered at approximately 1.3 and $1.6\ MeV$, respectively. The FWHM's of these peaks are around 0.3 and $0.5\ MeV$, respectively, which correspond to energy resolutions of around 23%, for the ^{17}N, and 31% for the ^{20}O. We observe that although both peaks are relatively close in energy, their energy resolutions (due to the intrinsic resolution of the array and to the Doppler broadening) are quite different. The energy resolution expected in our particular case at those energies ($\sim 900\ AMeV$) is around 23% (obtained with a GEANT simulation [GEANT, Fer01]), in good agreement with the value observed for the ^{17}N peak. The explanation for the different resolution observed for ^{20}O is that the peak is made of **two** different γ rays of around 1.6 and $1.9\ MeV$ which correspond to the de-excitation of the first and the second excited state of ^{20}O.

The contribution of different γ rays to the same peak at the γ-ray spectrum introduces an additional difficulty in the analysis that will be treated at the end of this chapter.

In the energy spectrum there are also contributions from background γ rays and from other particles. It is important to remember that the background con-

tribution is especially important at low energies, because it corresponds to γ rays emitted at rest. Each NaI detector was protected with one layer of aluminum ($2\ mm$ thick) and two layers of lead (each one $1\ mm$ thick) that absorbed these low energy γ rays and gave a negligible contribution in the region of the spectrum were the information about the emitted γ rays was crucial (see section 2.3.3.2).

3.4.2 Time information

The time information of the NaI detectors is used to discriminate γ rays (mainly coming from excited fragments after 1n-removal) from charged particles (mainly nuclei produced at or coming from the breakup target) and neutrons (which are ripped out of the nuclei in the breakup reactions). To be able to discriminate, the detector must have enough time resolution to distinguish in the time spectrum the peaks produced by the three contributions, specially the closest ones due to charged particles and γ rays. Typical time spectra obtained in our experiment are presented in the figure 3.8. The time spectra can be understood in the following way: coming from the interaction point, we have three kinds of particles, γ rays, neutrons and charged particles. The fastest ones are the γ rays, and after then we have the the neutrons and the charged particles. The biggest shower is the one produced by the charged particles, followed by the one generated by the γ rays. The neutrons shower is the weakest. With these considerations the charged particles shower is the first one seen, because though it comes later than the γ rays one, it is bigger and is sooner detected. The next one is originated by the γ rays, and finally, a not very high peak corresponding to the neutrons appears. By setting a gate at the γ rays position we get only their contribution and the energy spectrum is clean of unwanted background. NaI detectors are fast enough to distinguish the neutrons from the charged particles and the γ rays in our experiment, but due to the finite time resolution γ rays are sometimes difficult to filter (see figure 3.8 right).

3.4.3 Add-back procedure

With this correction we try to reconstruct γ events which did not leave all their energy in the first hitted detector, but only a part of it, and the rest is deposited in neighbour NaI crystals. The time information gives us the moment of the collection of a certain energy in one scintillator. If we look at the nearby detectors (usually four) as a whole by considering the energy of the detected γ ray as the addition of the energies deposited in these detectors, and assigning it to the first hitted NaI crystal of the group (before the Doppler correction) it is possible to

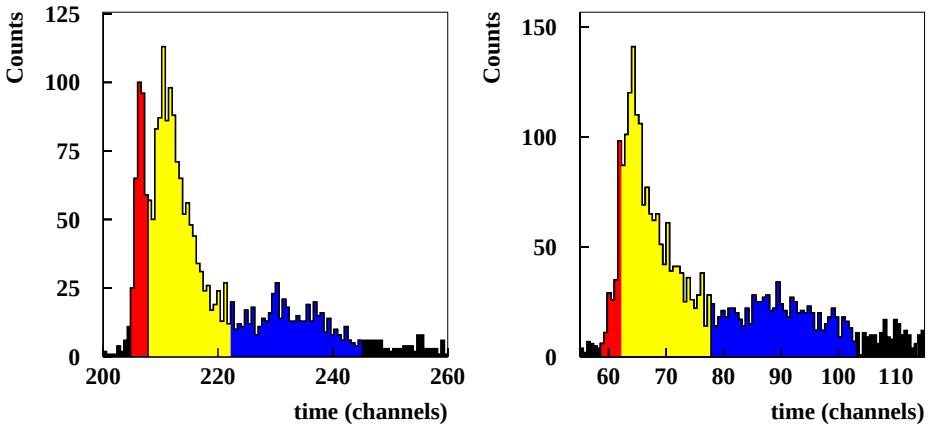

Figure 3.8: Left panel: Typical time spectrum of one individual NaI crystal during the experiment. Charged particles, γ rays and neutrons contributions are showed in different grey: intermediate for the charged particles, lighter for the γ rays, and darker for the neutrons. In the analysis a window getting only the γ rays is set to reduce the background. Right panel: NaI crystal time spectrum with bad time resolution.

gain in photo-peak efficiency without loosing in energy resolution. The effect of the correction is equivalent to have bigger detectors but the same Doppler broadening. Figure 3.9 illustrates this procedure.

In figure 3.10 we show the energy spectrum of the γ rays coming from de-excitation of ^{22}O ions recorded with our NaI array. On the left, the spectrum obtained after the Doppler correction is presented. To show the usefulness of the Add-back procedure with a real case, on the right we show the same spectrum after Add-back and Doppler correction. The peaks at 1.3 and $2.8\ MeV$ (corresponding to the γ de-excitation of the second excited state to the first one, and to the de-excitation of the first excited state to the fundamental one, respectively) appear much more clearly after applying the Add-back procedure.

3.4.4 Multiplicity

The γ multiplicity is defined as the number of γ rays that are detected by the γ array for a given event. In our experiment we observe quite high multiplicities. This was expected since we are dealing with high energy γ rays (of up to $6\ MeV$ in the case of the ^{23}O) due to the γ factor of around 2 that whe had. The application of the add-back procedure causes a considerable reduction in the observed

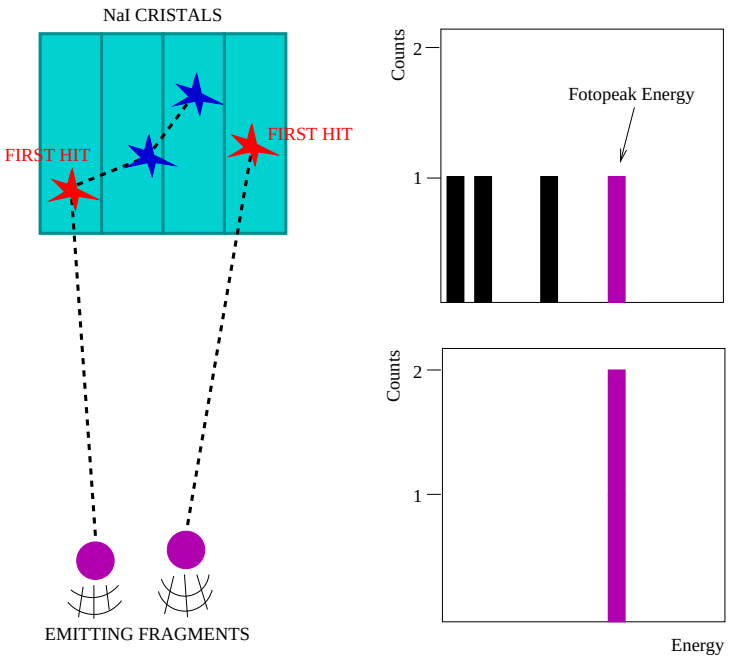

Figure 3.9: Schematic representation showing how the add-back procedure works. Two nuclei emit two γ rays. The first one releases its energy on three neighbour NaI crystals, the second one is totally absorbed in the first hit. Without treatment (upper spectrum) only the second gamma contributes to the photo-peak. By adding the energy of the three detectors hit by the first gamma and assigning it to the first hit crystal we can recover the event for the photo-peak (lower spectrum).

multiplicities (see figure 3.11 for an example with ^{20}O).

It is possible to account for some unwanted background in our spectrum if we stablish a cut in the multiplicity of the event after applying the add-back procedure. By selecting events of multiplicity 1 we remove unwanted events where the γ ray deposits its energy in different detectors and the add-back procedure has not been able to recover the event. The effect of the cut in multiplicity is shown in figure 3.11 for ^{20}O.

Upon this basis we selected for our analysis **only** events with multiplicity equal to **one** for all the studied nuclides.

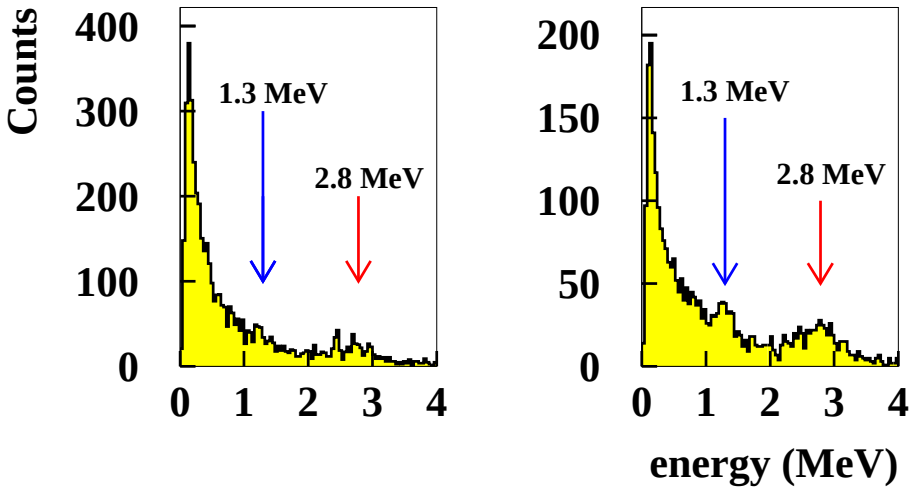

Figure 3.10: Energy spectrum of the radiation detected at the whole array with applied windows in Z and A/Z to select the projectile ^{23}O that goes to the fragment ^{22}O, before (left) and after (right) the Add-back procedure. The Doppler correction has been done to obtain the γ rays energies in the emitter (^{22}O) reference system.

3.5 Coincidences between γ rays and momentum distributions of core fragments

All the observables in the experiment were measured in an event-by-event basis. This allowed us to establish coincidences between them and select very particular channels.

The goal of the γ-ray detection was to discriminate the fragments emerging after 1n-removal at S2 in the ground state from contributions of those fragments in any excited state. This defines a very "selective" way to study nucleon(s)-removal reactions.

The procedure followed in order to select the fragments produced in the ground state is based on the γ ray information obtained with the NaI array located just after the target. The procedure consists of eight steps (see figure 3.12):

1. the first thing that this method requires is that all (or the most important) excited states of the core fragment deexcite to the ground state via one level that emits a single γ ray. This level is used to set the gate for the coincidence and it is usually the first excited state

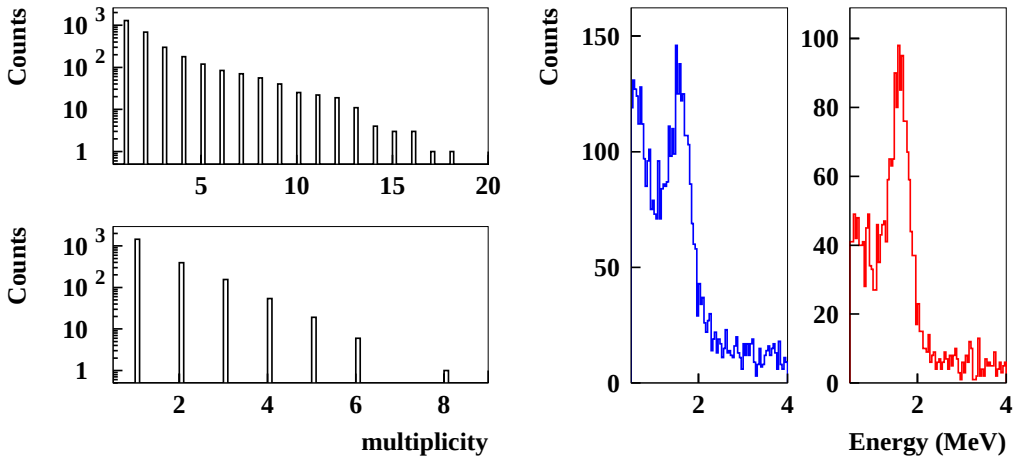

Figure 3.11: Left panel: Multiplicity obtained in the experiment for the nuclide ^{20}O, produced at S2 from ^{21}O inpinging on a carbon target. Two histograms are shown: the upper one corresponds to the case in which the raw spectrum is recorded. The lower one is obtained after applying the add-back procedure. Right panel: Example of how the cut in multiplicity can reduce the background present in the energy spectrum. In this case we see ^{20}O before (left) and after (right) requiring the multiplicity to be equal to one.

2. we obtain the fragment momentum distribution gating at the peak in the γ-ray spectrum (note that the background under the peak is also included). This recorded momentum distribution is made of events belonging to the peak, and of events coming from the background under the peak. We will call it $dN_g(p)$. The total number of events using this selection will be N_g and will come from the integration of $dN_g(p)$ over all the possible momenta p

3. we obtain the fragment momentum distribution for the background events alone (by setting a gate at very low energies in the γ-ray spectrum). We will call this distribution $dN_b(p)$. The total number of events will be N_b

4. in order to proceed to the background subtraction we need to estimate the peak-to-background ratio. For this purpose we determine the number of events inside the gate **in the γ ray spectrum** (N_s) and...

5. ...subtract the background to the peak (**in the γ ray spectrum**) by using an exponential decay function. With this correction it is possible to determine the number of events inside the gate that correspond **only** to the peak (N_p)

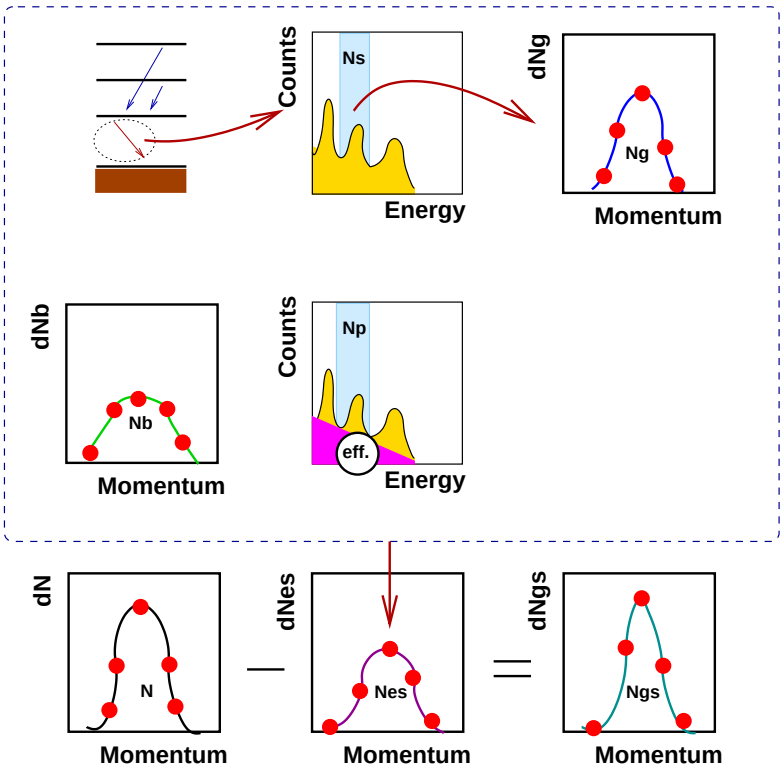

Figure 3.12: Schematic representation of the steps needed to obtain the longitudinal momentum distribution of the fragments that are produced in the ground state. The full explanation of these steps is given at the text, together with the nomenclature used at the figure. The abreviation "eff." stands for the efficiency of the NaI array at the energy of the peak in which we set the gate. The dashed box represents the equation 3.8.

6. the next step is to determine the efficiency of the NaI array at the energy of the gate (ϵ)

7. after this, we apply equation 3.8 to obtain the fragment momentum distribution when gating at the peak in the γ-ray spectrum, without background, and corrected from the NaI array efficiency (it corresponds to the fragments produced in any excited state) $dN_{es}(p)$. ρ is a factor that will be commented later, for the moment let us assume $\rho = 1$

$$dN_{es}(p) = [\frac{dN_g(p)}{N_g} - \frac{dN_b(p)}{N_b} \cdot (1 - \frac{N_p}{N_s})] \cdot \frac{N_s}{\rho \cdot \epsilon} \tag{3.8}$$

8. finally, if the total momentum distribution is called $dN(p)$, we calculate the momentum distribution when the fragment is produced in the ground state

$dN_{gs}(p)$: $dN_{gs}(p) = dN(p) - dN_{es}(p)$. Note that the total momentum distribution that must be used here is the one obtained with the same cuts as the ground- and excited-state ones, except any cut referring to the γ-ray spectrum

There are still some considerations related to this procedure that must be taken into account:

3.5.1 Background

The background is assumed to be due mainly to neutrons, because these particles are not easily distinguished from the γ rays at the time spectrum of the γ array due to the long tail of the neutron distribution (see *the time spectrum* section).

The observed profile for this undesired contribution to the energy spectrum is an exponential decay. This profile is subtracted in the energy spectrum in order to "remove" the background contribution when doing the calculations to obtain the ground- and excited-state momentum distributions.

There are some problems arising from this procedure of subtracting: when we have low intensity peaks over a big background, the error in the determination of what is peak and what is background related to the number of counts that belong to the peak increases a lot. This big relative error is propagated all across the method to obtain the ground- and excited-state momentum distributions. In conclusion, for these difficult cases one must be aware of the results.

3.5.2 Efficiency

The method used to calculate the efficiency was based on a complete simulation of the NaI γ array with GEANT [GEANT, Fer01]. The efficiency of the array for each particular case was obtained with the formula: $\epsilon = \frac{N_{detected}}{N_{emitted}}$ where "emitted" and "detected" refers to γ rays.

The number of emitted γ rays is one of the input parameters of the simulation. In order to obtain the number of detected γ rays we must be cautious. It is not only the number of events that go to the photopeak, but in some cases also, and due to the Doppler shift (that approximates) and broadening (that merges), the Compton edge and the pair production escape peaks (see figure 3.13).

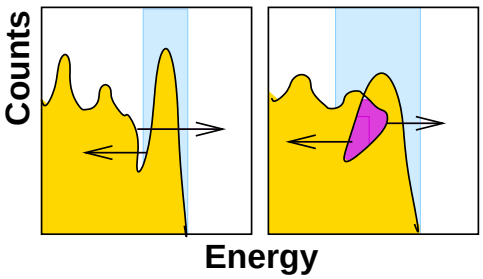

Figure 3.13: Schematic representation of the merging effect that the Doppler shift and Doppler broadening effects cause between photopeak, Compton edge and pair production escape peaks. Left panel: Spectrum obtained with the sources emitting at rest. Right panel: Spectrum obtained for the same sources, not emitting at rest, and after Doppler correction. The arrows show the movement of the critical parts. The shadowed area represents what is recognized as peak in both cases.

As a numerical example we will consider the case of the ^{22}O produced in the first excited state after one-neutron removal from ^{23}O. It decays to the ground state emitting a γ ray of around $3.1\ MeV$. The γ ray is emitted from a source moving with a speed of 0.8667c, so the effective energy of the γ ray seen by the array is around $6.2\ MeV$. The photopeak will be at approximately $6.2\ MeV$. The Compton edge position will be given by equation 3.9:

$$E_{Compton\ edge} = \frac{2E_\gamma^2}{m_e c^2 + 2E_\gamma} \tag{3.9}$$

Where E_γ is the energy of the γ ray and m_e is the electron mass at rest.

In our case, the Compton edge is located at approximately $6.0\ MeV$. The pair production single escape peak appears at approximately $5.7\ MeV$, and the double escape peak is at approximately $5.2\ MeV$. After Doppler correction these energies will be 3.1, 3.0, 2.8 and $2.6\ MeV$, respectively. We thus see that the Doppler shift causes that the differences in energy are reduced to *half* their initial values. The Doppler broadening completes the procedure of making them undistinguishable, and together with the intrinsic resolution of the array (at effective energies around $6.2\ MeV$, twice $3.1\ MeV$) the result is a much broader than expected peak made of photopeak, Compton, and pair production escape peaks. Note that the center of this peak will be at an energy lower that the photopeak energy, as is illustrated in figure 3.10, where the center of the peak is at approximately $2.8\ MeV$ and not at approximately $3.1\ MeV$.

We have performed a detailed study of the efficiency for each case, with the experimental conditions fully reproduced. We present in table 3.2 the efficiencies obtained for the energies of the peaks where we set the gates, for the different nuclides that presented peaks in their γ-ray spectra.

Table 3.2: Efficiencies at the peaks used to establish the gates for the coincidences. The label "isotope" indicates the corresponding core fragment.

Isotope	Energy (MeV)	ϵ (%)	$\Delta\epsilon$ (%)
^{17}N	1.3	5.93	0.59
^{19}N	1.0	5.81	0.58
^{20}O	1.6	5.38	0.54
^{22}O	2.8	4.79	0.48
^{22}F	1.6	5.28	0.53

3.5.3 Specific treatment of the different nuclides

Each nuclide is different from the others and some cases need special treatment. It is important here to individually analyze the level schemes, because they give information that can help to interpret the γ-ray spectra obtained with the NaI array. Different transitions in the level scheme can produce γ rays of similar energy, in such a way that it is not possible to distinguish between them in the γ-ray spectrum when we have limited energy resolution. Although we are not able to distinguish between these contributions in the γ-ray spectrum, we can still guess the different components that contribute to a given peak comparing with the level scheme if it is known.

In order to precise the contribution from each component we use the GEANT simulation [GEANT, Fer01]. The main input parameters for this simulation are the energy and emission probability of the γ ray. The procedure to obtain the contribution of the different components to one peak consists in finding the population probabilities (for the different levels) that best reproduce the experimental γ-ray spectrum.

We will face in our analysis contributions to one peak limited to only one or two components (or more that are negligible). The case in which the peak is only due to one particular transition is not problematic at all, but when there are

two components, some additional analysis is required.

As starting point we assume that before the breakup reaction the projectile is made of a contribution of the core in the ground state and, either a single configuration of the core in an excited state or a superposition of different configurations of excited states.

In the first case, and assuming that the reaction does not affect the core, the fragment remains in the same state as it was inside the projectile. If this is an excited state for the fragment nucleus, it will decay through different excited states to the ground state, by emitting γ rays. If two of those emitted γ rays have similar energy and fall inside the gate in the spectrum we will have *one* excited state counted twice, and this will give us an invalid number of excited states that must be corrected. For this purpose we placed the factor ρ in equation 3.8 to obtain the correct ground state distribution.

In the case of having different excited states contributing to the configuration of the core inside the projectile, the situation is more complicated than the one analyzed before, although the problematic is the same.

To understand the necessity for this additional correction that introduces the ρ factor we will study the case in which we produce N fragments that can be in the ground, in the first excited or in the second excited state. We will consider only the excited states that contribute to the peak (both of them in this example). Let us suppose that the fragments produced in the second excited state (with a population probability of α) deexcite via the first excited state by emitting a cascade of two γ rays with similar energy. The probability for direct population of the first excited state will be $(1-\alpha)$ (remember that we are only considering the excited states).

If we populate the first excited state, the probability for the detection of a single γ ray is equal to the total efficiency ϵ. In case that we populate the second excited state, remembering that we have set the multiplicity to 1, we can detect the γ ray that corresponds to the transition from the second to the first excited state, with the condition that we do not detect the other γ ray (that is: $\epsilon(1-\epsilon)$), or vice versa ($(1-\epsilon)\epsilon$), resulting in a total probability of $2\epsilon(1-\epsilon)$.

We can now add all the contributions to the peak at the γ-ray spectrum:

$$\epsilon(1-\alpha)N + 2\epsilon(1-\epsilon)\alpha N = (1+\alpha-2\epsilon\alpha)\epsilon N \tag{3.10}$$

And define the ρ factor for this particular case as:

$$\rho = (1 + \alpha - 2\epsilon\alpha) \tag{3.11}$$

We observe that in order to obtain the value for this factor we need to know α (the population probability for the second excited state) and the total efficiency at the peak energy: ϵ.

These values can be obtained with the help of the GEANT simulation [GEANT, Fer01]. α is an input parameter that is selected to be the one that gives the best agreement between the simulation and the experiment. ϵ is an output parameter of the simulation that is obtained by dividing the number of counts under the peak at the spectrum by the number of emitted γ rays.

Remember that we have assumed (as a requisite) for our coincidence method that all the de-excitations from excited states go through the emission of one particular γ ray. This γ ray contributes to one peak, and we establish the gate for the coincidences in that peak. We normalize to 100 % the most probable γ ray. In the previous example, the probability for the emission of the γ ray that corresponds to the transition from the second to the first excited state is $\alpha \cdot 100$ %, while the probability for the other γ ray is $[\alpha + (1-\alpha)] \cdot 100$ % $= 100$ %.

In conclusion, when applying the coincidence method, each case has to be treated in a particular way. The level scheme can help us to detect peaks with contributions from different levels. In our analysis we have found that we needed to use the ρ factor only with ^{21}O going to ^{20}O, and ^{23}O going to ^{22}O.

Chapter 4

Results on $^{17-21}$N, $^{19-24}$O and $^{21-27}$F

In this chapter we will present all the results obtained for the different observables studied in this experiment using the procedures explained in chapter **3**.

This chapter is organized in four main sections corresponding to the different studied observables. The valence nucleon removal cross-sections of the different reaction channels are presented first, they are followed by the detailed analysis of the momentum distributions of the core fragments, then we present the γ-ray spectra corresponding to those core fragments produced in excited states, and we finish with the most interesting section: the coincidences between the momentum distribution of the core fragments and their gamma de-excitation.

It is important to note that all the interpretations done in this chapter are very intuitive and take the single particle picture as basic point of view, although sometimes deeper insights are given.

4.1 Valence nucleon(s) removal cross-sections

The **X**-nucleon removal cross-section measurement can provide information about the role played by those **X** nucleons when they where part of the projectile just before the reaction.

This information is mainly related to the quantum state, that indeed affects the behaviour of the other components inside the nucleus (exotic projectile).

It is important to note that the validity of the previous affirmation relies on the fact that the reaction must be peripheral: the **X** nucleons removed are the most external ones, leaving the rest of the projectile (the "core") unaffected. These were the conditions that we had in our experiment.

4.1.1 One-neutron removal

The study of the cross-section in 1n-removal reactions provides a first insight in the valence nucleon structure of the projectile nucleus (exotic projectile). We have studied mainly the case of nuclear breakup using a carbon target, although the Coulomb breakup was also studied for several cases (lead target).

4.1.1.1 Carbon target: projectiles $^{17-20}$N, $^{19-23}$O and $^{21-26}$F

In figure 4.1 we represent the *one-neutron removal cross-sections* for different isotopes of nitrogen, oxygen and fluorine approaching the neutron dripline measured in our experiment. The target used in this case was carbon. As a consequence, the reaction was dominated by the nuclear force.

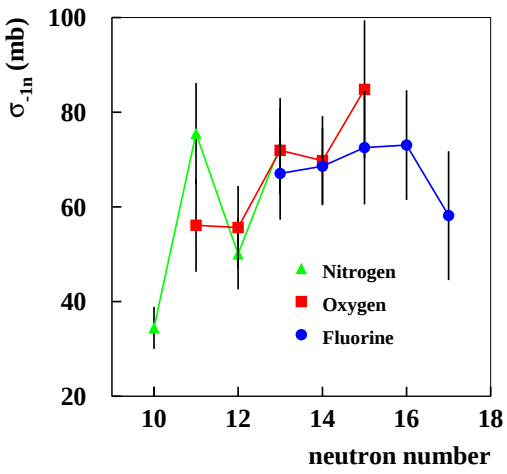

Figure 4.1: One-neutron removal cross-sections for different isotopes of nitrogen (triangles), oxygen (squares) and fluorine (circles) on a carbon target. We represent in the x-axis the number of neutrons of the isotope, and in the y-axis the corresponding cross-section.

The numerical values (with their corresponding errors) of the one-neutron removal cross-sections on a carbon target for the different isotopes of nitrogen, oxygen and fluorine are shown in table 4.1. The lower and bigger values correspond to ^{17}N and ^{23}O, respectively.

The main error sources in the determination of the cross-sections are the statistical errors associated to the number of ions recorded at $S2$ and $S4$ and the incertitude coming from the MOCADI simulation needed to calculate the transmission of the FRS from $S2$ to $S4$,

which is estimated to introduce an error of around 10% relative to the transmission value. This transmission has been shown in table 3.1.

Table 4.1: Values of the one-neutron removal cross-sections (with their corresponding errors) for the different isotopes of nitrogen, oxygen and fluorine on a carbon target. The main error sources are: the statistical error associated to the number of ions recorded at $S2$ and $S4$, and the error of around 10% estimated for the MOCADI simulation needed for the calculation of the transmission from $S2$ to $S4$.

Projectile	σ_{-1n} (mb)	$\Delta\sigma_{-1n}$ (mb)
^{17}N	34.5	4.5
^{18}N	75.	11.
^{19}N	50.1	7.5
^{20}N	73.	10.
^{19}O	56.1	9.8
^{20}O	55.6	8.8
^{21}O	71.9	8.9
^{22}O	69.8	9.4
^{23}O	85.	15.
^{22}F	67.1	9.8
^{23}F	68.6	8.1
^{24}F	73.	12.
^{25}F	73.	12.
^{26}F	58.	14.

The first thing that can be appreciated in these results is the strong dependence of the cross-section on the number of neutrons that the projectile has, for a fixed specie (nitrogen, oxygen or fluorine). If the isotope has an even number of neutrons, these couple together and form pairs, resulting in a very stable configuration.

When the number of neutrons is odd, one remains unpaired, and results into a more unstable situation. It is easier to remove this *less bound* neutron. The consequence is that the probability of the reaction will be higher for those isotopes with an odd number of neutrons.

We present in figure 4.2 the results for each isotopic chain compared to the values presented by *E. Sauvan* in [Sau00a] for the cross-sections measured at a lower energy (around $60\ AMeV$). Apart from the fact that our cross-sections are

lower (as it would be expected, since we work at higher energies), it is possible to observe a similar behaviour between both set of data for all the studied nuclear species.

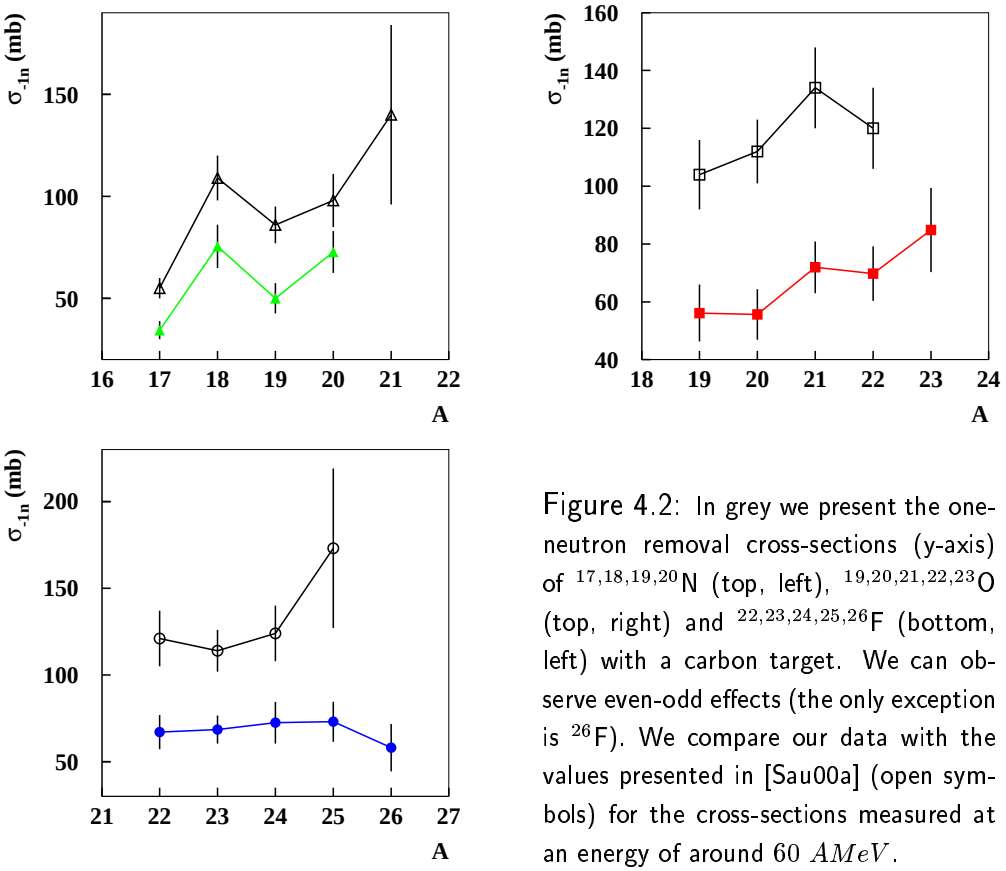

Figure 4.2: In grey we present the one-neutron removal cross-sections (y-axis) of ^{17,18,19,20}N (top, left), ^{19,20,21,22,23}O (top, right) and ^{22,23,24,25,26}F (bottom, left) with a carbon target. We can observe even-odd effects (the only exception is ^{26}F). We compare our data with the values presented in [Sau00a] (open symbols) for the cross-sections measured at an energy of around $60\ AMeV$.

Another effect that can be observed is the gradual increase of the removal cross-section with respect to the *mass number*. This effect appears superposed to the even-odd effect. It is logical to observe an increase in size of the valence neutron distribution when the mass number increases. Therefore, the probability to interact with the target will be also larger.

The *removal cross-section* of ^{23}O does not present a strong increase compared to the general trend of its neighbours, as has been observed in the case of the *interaction cross-section* in a recent experiment [Oza01]. This fact,

togheter with the relatively high value of the one-neutron separation energy (S_n=$2.74 \pm 0.12\ MeV$) that ^{23}O has, does not seem to support the idea of ^{23}O being a halo nucleus. We will discuss more about this topic in section 4.4.4.

The increase in the one-neutron removal cross-section of ^{23}O is justified because:

- ^{23}O has an *odd neutron number* (N=15)
- the wave function of its valence neutron presents a *large spatial distribution*, as we will see when we discuss the core fragment momentum distributions in section 4.2
- the protons and the neutron core *fill the levels completely up to* $1d_{5/2}$ (assuming the single particle picture), which is a relatively stable configuration

These three facts increase the probability of the reaction in which the valence neutron is removed without affecting the rest of the nucleus, thus increasing the corresponding cross-section.

Let us now discuss the behaviour of ^{26}F, whose cross-section seems to be too low compared to its neighbours'. From a single particle point of view, in ^{26}F the valence neutron should be **alone** in the $1d_{3/2}$ level. This also means that the neutron core should fill the levels completely up to $2s_{1/2}$, and be quite stable. The probabilities for a reaction in which we remove the aparently losely bound valence neutron, leaving the core unaffected, are expected to be high, but in turn we observe a rather low removal cross-section, compared to that of its neighbour ^{25}F. The explanation for this is not clear at the moment. We will comment more about ^{26}F particularities when we present the momentum distributions.

4.1.1.2 Lead target: projectiles ^{19,20}N, ^{22,23}O and ^{25,26}F

The main reason to make measurements with a different target was to study the role played by the dominant reaction mechanism. In this way we chose a heavier target (lead), which has a high Z number, and increases the influence of the Coulomb force on the reaction. In this case, the breakup is dominated by the Coulomb component, and not by the nuclear force as in the case of the carbon target. Although the nuclear component is masked by the stronger Coulomb one, we must remember that it is still there.

The Coulomb interaction is a long range interaction. As a consequence, the area of influence of the reaction gets considerably extended and the removal cross-sections are increased, as can be seen in figure 4.3.

In this figure we plot simultaneously the results obtained for the three species: nitrogen, oxygen and fluorine. We can observe again the even-odd effects depending on the neutron number of the isotope.

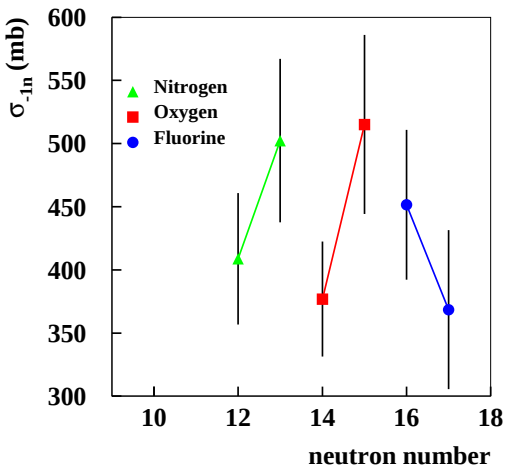

Figure 4.3: One-neutron removal cross-sections for different isotopes of nitrogen (triangles), oxygen (squares) and fluorine (circles) on a lead target. We represent in the x-axis the number of neutrons of the isotope, and in the y-axis the cross-section.

The values (with their corresponding errors) of the one-neutron removal cross-sections on a lead target for the different isotopes of nitrogen, oxygen and fluorine measured in our experiment are presented in table 4.2. The main error sources for the cross-sections are the same as the ones already presented for *one-neutron removal* on carbon. The values of the removal cross-sections here are considerably bigger than the ones obtained with the carbon target, which is normal since the lead target interacts more with the projectiles, due to the Coulomb force, predominant here.

Table 4.2: Values of the one-neutron removal cross-sections (with their corresponding errors) for the different isotopes of nitrogen, oxygen and fluorine on a lead target. The error sources are the same as those for the carbon target.

Projectile	σ_{-1n} (mb)	$\Delta\sigma_{-1n}$ (mb)
^{19}N	409.	52.
^{20}N	502.	65.
^{22}O	377.	45.
^{23}O	515.	71.
^{25}F	452.	59.
^{26}F	369.	63.

4.1.2 Two-neutron removal on a carbon target: projectiles ^{21}N, ^{24}O and ^{27}F

The *two-neutron removal* channel was explored for some isotopes candidates to *two-neutron* halos. In this way we studied the reaction for ^{24}O and ^{27}F. The not so exotic ^{21}N was produced in the same setting with a relatively high transmission, and it was studied in order to make a comparison with the other two isotopes (^{24}O and ^{27}F).

The values of the removal cross-sections (with their corresponding errors) are presented in table 4.3. The main error sources are of two origins. One statistical, associated to the counts recorded by the SEETRAM and by the plastic scintillator located at $S4$. The other one is estimated to be around 10% for the MOCADI simulation needed to calculate two transmissions this time: from the SEETRAM position to $S2$, and from $S2$ to $S4$.

The low values obtained for ^{21}N and ^{24}O are coherent since both of them present a filled level structure ($1d_{5/2}$ the ^{21}N, and $2s_{1/2}$ the ^{24}O) from a single particle point of view, and it is difficult to remove the last two neutrons without disturbing (and eventually breaking) the remaining part of the nucleus. As the reaction mechanism is not so simple in the case of two-neutron removal reactions, we must make the assumption that the breakup reaction does not remove both neutrons simultaneously, but sequentially:

The last two neutrons in ^{24}O are supposed to be paired in a $2s_{1/2}$ level. In principle, it would not be very difficult to remove **at the same time** both of them without disturbing too much the remaining closed level ($1d_{5/2}$) core, but this is not what we observe in our results.

From a mathematical point of view, the fact that one single interaction between the projectile and the fragment results into a simultaneous removal of two neutrons from the projectile is much more unprobable than a two-step one. In this last case we can have:

- A first interaction with the target that removes one of the $2s_{1/2}$ neutrons, followed (soon or later) by another interaction (mainly with the target) that removes the second $2s_{1/2}$ neutron (that can be in an excited state of ^{23}O)

- A first interaction with the target that removes one of the $2s_{1/2}$ neutrons, followed by the (more or less delayed) emission of the remaining $2s_{1/2}$

neutron, that was excited with enough energy to scape the resulting ^{23}O nucleus

These two possibilities have as first step the removal of a well bound $2s_{1/2}$ neutron, which reduces the probability of the reaction, resulting in a low value for the cross-section. This reasoning can be applied in a "similar" way to the ^{21}N case.

With ^{27}F things are different: the neutrons probably removed in the reaction are the ones in the $1d_{3/2}$ level. We can put up to four neutrons in this level, but we only have two in this case (the level is not full). Therefore, it is more probable to remove both neutrons without disturbing the nucleus too much. Note also that the big error ($\pm$80 mb) that we have in this case makes the result compatible with a two-neutron removal cross-section of 59 mb, which is not very large and would make our interpretation of the datum debatable. The same discourse can be applied to ^{24}O (with error equal to $\pm$30 mb).

Table 4.3: Values of the two-neutron removal cross-sections (with their corresponding errors) for the different isotopes of nitrogen, oxygen and fluorine on a carbon target. The main error sources here are: statistical associated to the counts recorded by the SEETRAM and by the scintillator at $S4$, and the error of 10% estimated for MOCADI (used this time to calculate two transmissions: from the entrance of the FRS -position of the SEETRAM- to $S2$, and from $S2$ to $S4$).

Projectile	σ_{-2n} (mb)	$\Delta\sigma_{-2n}$ (mb)
^{21}N	27.	12.
^{24}O	55.	30.
^{27}F	139.	80.

A different interpretation that could explain the differences in the cross-sections values for ^{24}O and ^{27}F, can be made if we accept the appearance of a new magic number at $N = 16$. Under this point of view, ^{24}O is a double closed shell nuclei, so it is rather stable against neutron removal, and the corresponding cross-section should be small. On the other side, ^{27}F is a two-neutron off-shell nucleus and the ^{25}F core presents a closed shell structure for neutrons (thus resulting quite stable), as a consequence, for ^{27}F the cross-section should be large.

However, one open question appears if we accept the reasoning done in the last paragraph: within this image, ^{26}F is a one-neutron off-shell nucleus and

should present a large one-neutron removal cross-section, but we do not observe this in our data.

In conclusion, from the results obtained here, and taking into account the corresponding errors (quite big in some cases) and the incertitude related to the way in which the reaction mechanism takes place, we can say that:

- ^{24}O is probably not a two-neutron halo nucleus

- It would be interesting to study more the ^{27}F case, because the value obtained for the two-neutron removal cross-section is quite high and could imply a two-neutron halo structure

4.2 Momentum distributions of core fragments

The study of the "core fragment momentum distribution" emerges from the necessity of obtaining a more extensive experimental information than the single one provided by the corresponding cross-section.

We must remember that the momentum distribution of the core fragment is related to the Fourier transform of the probability density of the valence nucleon(s) removed in the reaction. The core fragment momentum distribution together with the valence nucleon(s) removal cross-section represent a very complete picture of the exotic projectile outer structure.

In this section we will present core fragment momentum distributions corresponding to the performed removal reactions. We have studied longitudinal and transversal components with carbon and lead targets in the 1-n removal channel, and only carbon target in the 2-n removal channel.

It is important to mention at this point that the figures with core fragment momentum distribution profiles are always presented without subtracting the intrinsic resolution of the FRS, while the data related to the Full Widths at Half Maximum (FWHM) of these distributions are always presented **after subtracting** the corresponding intrinsic resolution. In order to provide additional information, the root-mean-square (RMS) of each distribution (without subtracting the intrinsic resolution) is also shown. The FWHM and error associated to the intrinsic resolution of the FRS was obtained by *Gaussian* fit (see figure 4.7).

4.2.1 One-neutron removal: Longitudinal component

We will first present the component of the core fragment momentum distribution that is longitudinal with respect to the reference coordinates (**z** in our experiment). This observable is in principle the less affected by experimental errors, because the procedure to obtain it is the most direct. We present in figure 4.4 an example of the core fragment longitudinal momentum distributions obtained for different studied nuclides with carbon target showing the evolution of this observable when we approach the neutron dripline.

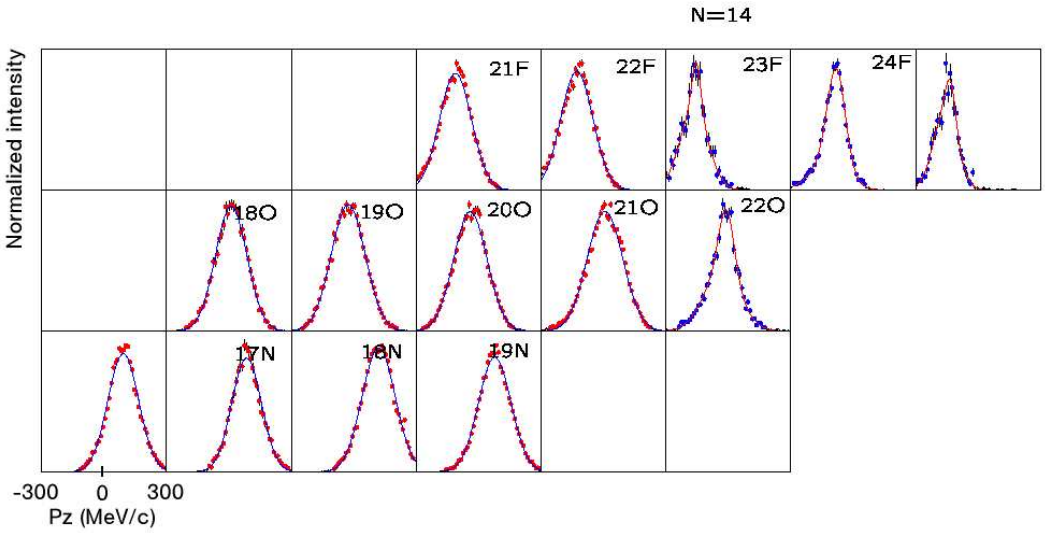

Figure 4.4: Longitudinal momentum distributions of the different fragments of nitrogen, oxygen and fluorine obtained after a one-neutron removal reaction on a carbon target. All the distributions cover the same range in the x-axis. The y-axis represents normalized intensities.

4.2.1.1 Carbon target: projectiles $^{17-20}$N, $^{19-23}$O and $^{21-26}$F

We present in figure 4.5 (left) the FWHM (Full Width at Half Maximum) of the longitudinal momentum distributions of the fragments in the reaction with the carbon target. We show the results for the three studied species (nitrogen, oxygen and fluorine) after subtracting the particular intrinsic resolution of the FRS for each case (measured in a different setting in which the projectiles were

transmitted to the final focal plane, as we explained in chapter **3**). The intrinsic resolution was in this case of the order of $18\ MeV/c$ of FWHM (as is illustrated in figure 4.7 for the case of ^{21}O). On the right side of the figure 4.5 we present a comparison between our results and those presented in [Sau00a]. There is a very good agreement between both set of data, even though the measurements have been done at different energies (around $1\ AGeV$ and $60\ AMeV$, respectively), which shows that the longitudinal component of the core fragment momentum distribution seems to be independent of the energy.

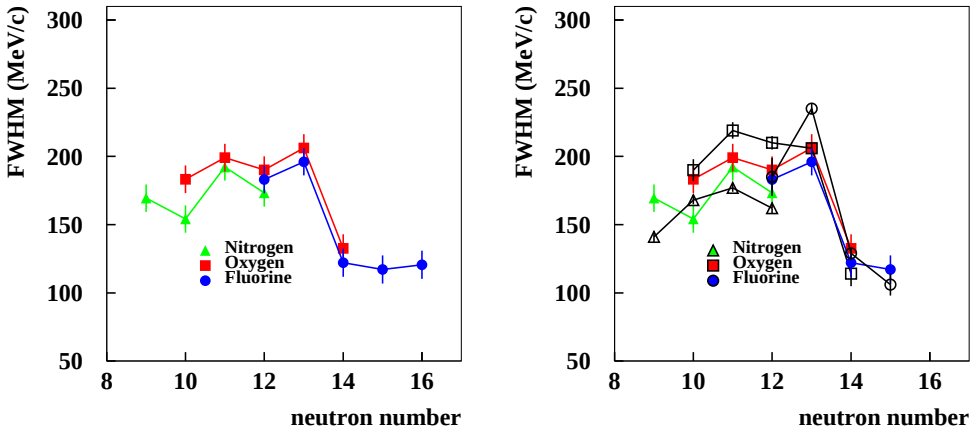

Figure 4.5: Left panel: FWHM's of the longitudinal momentum distribution of different core fragments of nitrogen (triangles), oxygen (squares) and fluorine (circles) after one-neutron removal on a carbon target. We represent in the x-axis the number of neutrons of the isotope, and in the y-axis the corresponding FWHM. Right panel: Comparison of our data with the values presented in [Sau00a] (shown here in open symbols) measured at an energy of around $60\ AMeV$.

The first thing that can be appreciated is a similar behaviour in the three species, which seems to indicate a relative "independence" on the proton number.

We also observe a rather constant behaviour and a strong decrease in the FWHM's when we reach a fragment neutron number N=14. If assume that the simple picture relating the momentum distribution to the Fourier transform of the spatial distribution is valid, we can intepret the observed *decrease* in the width of the *momentum* distribution profile as an *increase* in the width of the *spatial* distribution profile of the valence neutron removed in the reaction.

This can be explained from a single particle point of view. At N=14 (for the projectile) the $1d_{5/2}$ level is full of neutrons. If we add a new one (N=15), we start filling the $2s_{1/2}$ level, which is a spatially more extended level than the $1d_{5/2}$ one, (because it is an *s* level and because it is the *second* s level).

So we can expect a reduction of the width associated to the momentum distributions for the fragment neutron numbers N=14 and N=15 (corresponding to the filling of the $2s_{1/2}$ level). When we reach N=17, in the projectile, (we start filling the $1d_{3/2}$ level) we should see an increase in the value of the FWHM (case of ^{25}F coming from ^{26}F), but we do not observe this effect in our data.

Finally, we also observe what seems to be an even-odd effect. Projectile isotopes with an odd number of neutrons have fragments that present a FWHM smaller than their neighbours (projectiles with an even number of neutrons). This means that the spatial distribution of the wave function of the valence (and removed) neutron is larger. This is coherent since the odd neutron is less bound.

In table 4.4 we present the values of the FWHM's (with their corresponding errors) assigned to the longitudinal momentum distribution of the different isotopes of nitrogen, oxygen and fluorine after a **one-neutron removal breakup reaction** on a **carbon** target (which have been obtained by direct evaluation on the histogram) compared to the *Gaussian* fits. The RMS of each distribution is also shown.

The main error source in this observable comes from the fact that we do not know the function to which we must fit the distribution profile in order to calculate the FWHM. We considered three posibilities: *Gaussian*, double *Gaussian* and *Lorentzian*. The *Lorentzian* profile was not suitable, so we focussed on comparing the results with *Gaussian* and double *Gaussian*, and we observed a mean difference in the FWHM obtained with both fits equal to $|10\ MeV/c|$, so we decided to set the error bars for the FWHM of the core fragment longitudinal momentum distributions obtained using a carbon target to $\pm 10\ MeV/c$ for all the nuclides. The FWHM's were directly obtained recording the full width at half maximum over the histogram. In some cases the low statistics was another important error source. Additional sources are the intrinsic resolution of the FRS and the precisions of the different detectors in the particular setup used to obtain the core fragment momentum distribution in the *center of mass* system (TPC's, Hall probe, plastic scintillators), but their contributions fall within the error bars assigned above.

Table 4.4: Values of FWHM's (with their corresponding errors) assigned (by direct evaluation on the histogram) to the longitudinal momentum distribution of the different isotopes of nitrogen, oxygen and fluorine after a **one-neutron removal breakup reaction** on a **carbon** target (FWHM) compared to the *Gaussian* fits (g-FWHM). The normalized χ^2s of the *Gaussian* fits, and the RMS of each distribution are also shown.

Fragment	RMS (MeV/c)	FWHM (MeV/c)	g-FWHM (MeV/c)	χ^2/ndf
^{16}N	76.	169. $\pm$ 10.	177.	8.7
^{17}N	73.	154. $\pm$ 10.	168.	4.5
^{18}N	82.	192. $\pm$ 10.	192.	6.2
^{19}N	79.	173. $\pm$ 10.	184.	9.7
^{18}O	78.	183. $\pm$ 10.	183.	1.6
^{19}O	85.	199. $\pm$ 10.	199.	1.9
^{20}O	84.	190. $\pm$ 10.	196.	4.6
^{21}O	89.	206. $\pm$ 10.	206.	13.8
^{22}O	78.	133. $\pm$ 10.	171.	19.4
^{21}F	82.	183. $\pm$ 10.	189.	16.2
^{22}F	86.	196. $\pm$ 10.	196.	28.9
^{23}F	74.	122. $\pm$ 10.	157.	12.2
^{24}F	68.	117. $\pm$ 10.	138.	24.7
^{25}F	64.	121. $\pm$ 10.	139.	3.25

4.2.1.2 Lead target: projectiles ^{19,20}N, ^{22,23}O and ^{25,26}F

In this section we will study the effect of the reaction mechanism over the core fragment longitudinal momentum distribution. For this purpose we use the lead target, for which the interaction probabilities with the projectiles are larger.

We present in figure 4.6 (left) the FWHM of the longitudinal momentum distributions of the fragments after the reaction with the lead target. The results are represented again for the three studied species (nitrogen, oxygen and fluorine) after subtracting the particular intrinsic resolution of the FRS for each case. The intrinsic resolution was in this case around $27\ MeV/c$ of FWHM.

If we compare figures 4.5 and 4.6 (left) we see that the results obtained in both cases are consistent (within the error bars).

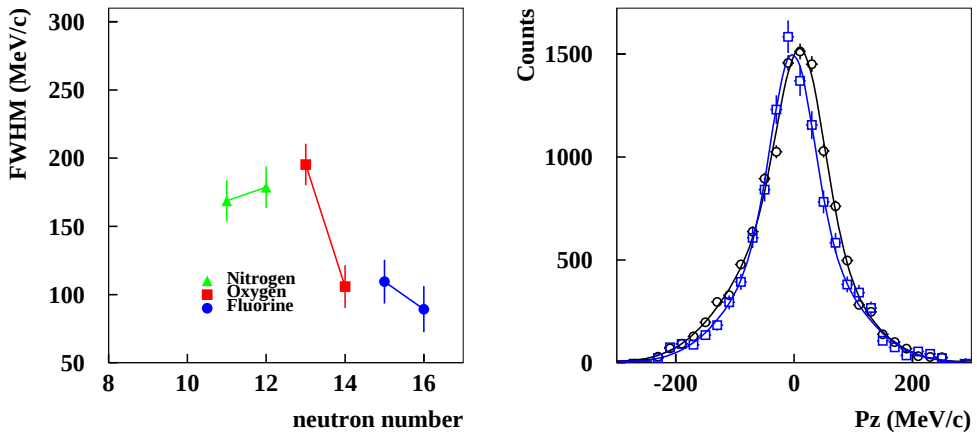

Figure 4.6: Left panel: FWHM's of the longitudinal momentum distribution of different core fragments of nitrogen (triangles), oxygen (squares) and fluorine (circles) after one-neutron removal on a lead target. We represent in the x-axis the number of neutrons of the isotope, and in the y-axis the corresponding FWHM. Right panel: Comparison of the measured longitudinal momentum distributions of ^{22}O after one-neutron removal on a carbon (open circles) and on a lead target (open squares). Both distributions have been normalized arbitrarily in order to compare their profiles in a proper way and have not been corrected by the intrinsic resolution of the FRS yet.

We present in figure 4.6 (right) the longitudinal component of the momentum distribution of ^{22}O after 1n-removal on lead compared to that on carbon before subtracting the intrinsic resolution of the FRS for each case. Both distributions appear to be very similar, showing that the core fragment longitudinal component seems to be independent of the target, even before subtracting the intrinsic resolution.

We present in table 4.5 the values of the FWHM's (with their corresponding errors) assigned to the longitudinal momentum distribution of the different isotopes of nitrogen, oxygen and fluorine after a **one-neutron removal breakup reaction** on a **lead** target (which have been obtained by direct evaluation on the histogram) compared to the *Gaussian* fits. The RMS of each distribution is also shown. The error sources are those already discussed for the carbon target (the selected error bar was this time of $\pm 15\ MeV/c$) and the added contribution of the error that comes from subtracting the intrinsic resolution of the FRS. In this case, the errors associated to the intrinsic resolution of the FRS were bigger, specially for the fragments ^{22}O, ^{24}F and ^{25}F.

Table 4.5: Values of FWHM's (with their corresponding errors) assigned (by direct evaluation on the histogram) to the longitudinal momentum distribution of the different isotopes of nitrogen, oxygen and fluorine after a **one-neutron removal breakup reaction** on a **lead** target (FWHM) compared to the *Gaussian* fits (g-FWHM). The normalized χ^2s of the *Gaussian* fits, and the RMS of each distribution are also shown.

Fragment	RMS (MeV/c)	FWHM (MeV/c)	g-FWHM (MeV/c)	χ^2/ndf
^{18}N	73.	169. $\pm$ 15.	169.	6.0
^{19}N	77.	179. $\pm$ 15.	179.	2.9
^{21}O	85.	195. $\pm$ 15.	195.	4.0
^{22}O	76.	106. $\pm$ 16.	159.	5.4
^{24}F	61.	109. $\pm$ 16.	120.	6.9
^{25}F	58.	89. $\pm$ 17.	106.	2.4

4.2.2 One-neutron removal: Transversal components

We will discuss now the analysis of the transversal components of the core fragment momentum distribution (**x** and **y** in our experiment). We will follow the same path we took in the case of the longitudinal component and start with the carbon target.

The FWHM's have been obtained in the same way as in the case of the longitudinal component of the core fragment momentum distribution.

4.2.2.1 Carbon target: projectiles $^{17-20}$N, $^{19-23}$O and $^{21-26}$F

As we have already mentioned, the transversal components are affected by an additional imprecision that the longitudinal component does not have, since they are obtained from the longitudinal component itself and from the angular dispersion of the fragments in x and y just after the breakup target.

This imprecision makes the transversal components less reliable than the longitudinal component when showing the behaviour of the FWHM with respect to the neutron number of the isotope.

In another hand we have to keep in mind that the transversal components are more affected by the reaction. This will be explained more in detail in chapter **5**.

These two effects are also true for the intrinsic resolution of the FRS, that in this case perturbs the shape of the distribution in a non negligible way (see figure 4.7 for a graphical comparison of the three components of the intrinsic resolution with a carbon target used in the case of ^{21}O).

As a consequence, the FWHM's after intrinsic resolution correction are not very accurate and present big error bars. The intrinsic resolutions in the directions x and y using a carbon target present FWHM's around 121 MeV/c and 109 MeV/c, respectively.

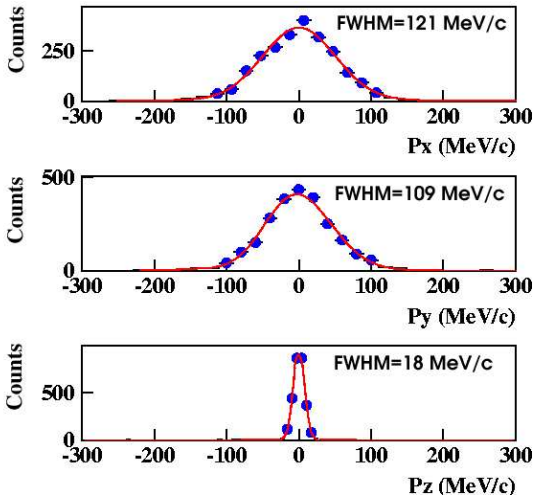

Figure 4.7: Comparison of the FRS intrinsic resolution in x, y and z used in the case of ^{21}O one-neutron removal on a carbon target. As can be seen, the resolution is much better for the longitudinal component.

This can be seen on the left side (top and bottom) of the figure 4.8 (corresponding to the x- and y-components), where the nuclear structure effects that we were able to transparently see in the longitudinal component are less clear in this case. On the right side of the figure we show the comparison with the results presented in [Sau00a] for the transversal components of the momentum distribution for the same isotopic chains measured at lower energies. The data seem to be consistent within the error bars that have been assigned.

In tables 4.6 and 4.7 we present the values of the FWHM's (with their corresponding errors) assigned to the transversal momentum distributions (in **x** and **y**) of the different isotopes of nitrogen, oxygen and fluorine after a **one-neutron removal breakup reaction** on a **carbon** target (which were obtained by direct evaluation on the histogram) compared to the *Gaussian* fits. The RMS of each distribution is also shown. The main error sources are the same that we had discussed in the case of the longitudinal component with a carbon target. We have to add now the imprecision derived from the determination of the angle of the trajectory of the fragments in x and y, just after they are produced. Finally, the intrinsic resolution of the FRS, worse for the transversal components, contributes to enlarge the associated errors.

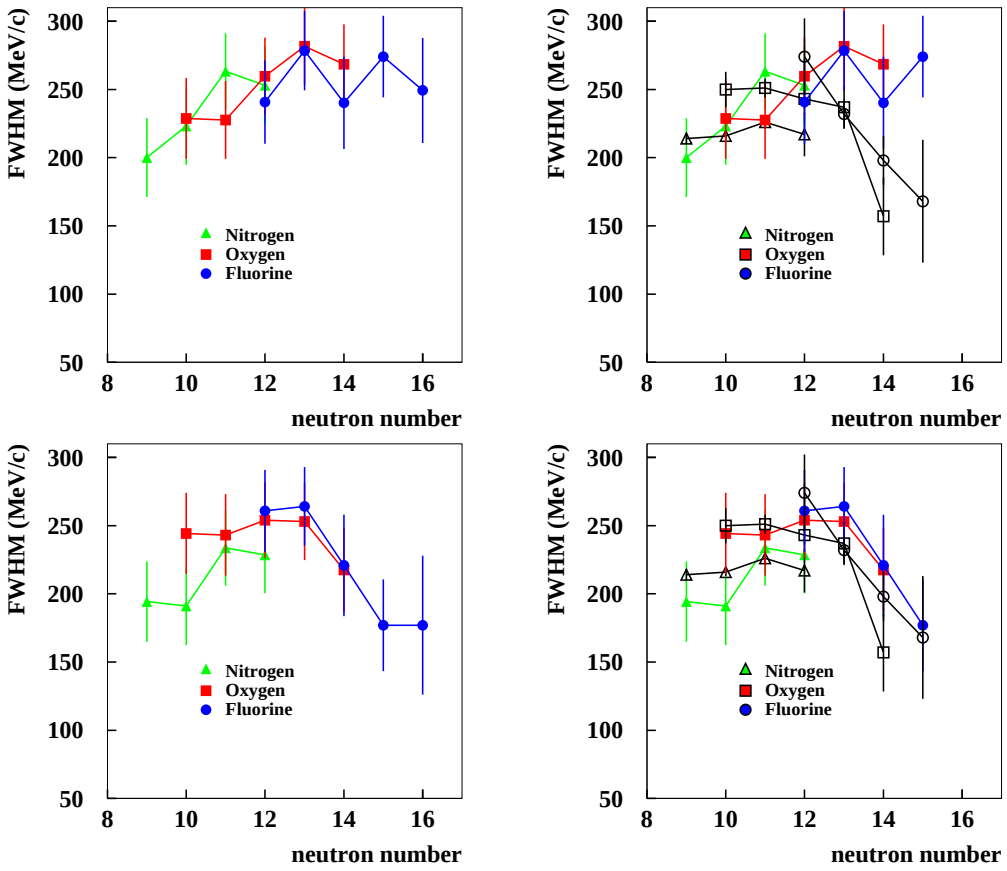

Figure 4.8: Left panel: FWHM's of the transversal momentum distribution in the x- (top) and y-direction (bottom) for different isotopes of nitrogen (filled triangles), oxygen (filled squares) and fluorine (filled circles) after one-neutron removal on a carbon target. We represent in the x-axis the number of neutrons of the isotope, and in the y-axis the corresponding FWHM. Right panel: Comparison of our data with the values presented in [Sau00a] (shown here in open symbols) for the FHMS's measured at an energy of around 60 $AMeV$.

4.2.2.2 Lead target: projectiles ^{19,20}N, ^{22,23}O and ^{25,26}F

We will present now the transversal components of the momentum distribution when the reaction takes place on a lead target. We show in figure 4.9, the transversal components of the momentum distribution of ^{22}O after 1n-removal on lead compared to those on carbon before subtracting the intrinsic resolution of the FRS for each case (FWHM around 345 MeV/c for the x component and

Table 4.6: Values of FWHM's (with their corresponding errors) assigned (by direct evaluation on the histogram) to the transversal momentum distributions (in **x**) of the different isotopes of nitrogen, oxygen and fluorine after a **one-neutron removal breakup reaction** on a **carbon** target (FWHM[x]) compared to the *Gaussian* fits (g-FWHM[x]). The normalized χ^2s of the *Gaussian* fits, and the RMS of each distribution are also shown.

Fragment	RMS[x] (MeV/c)	FWHM[x] (MeV/c)	g-FWHM[x] (MeV/c)	$\chi^2[x]/ndf$
^{16}N	100.	200. ± 29.	214.	13.0
^{17}N	110.	223. ± 28.	238.	4.9
^{18}N	114.	263. ± 28.	263.	7.8
^{19}N	114.	253. ± 29.	253.	6.7
^{18}O	105.	229. ± 30.	229.	2.4
^{19}O	105.	228. ± 29.	228.	4.6
^{20}O	116.	260. ± 28.	260.	5.4
^{21}O	122.	282. ± 28.	282.	1.9
^{22}O	118.	268. ± 29.	269.	2.2
^{21}F	112.	241. ± 31.	241.	3.8
^{22}F	123.	278. ± 29.	277.	3.8
^{23}F	114.	240. ± 34.	240.	1.3
^{24}F	121.	274. ± 30.	274.	2.7
^{25}F	119.	249. ± 38.	249.	3.2

around $315\ MeV/c$ for the y component). In contrast with the situation obtained for the longitudinal component, the target influences the profile of the transversal component before subtracting the intrinsic resolution: The momentum distribution is significantly wider for lead.

In figure 4.10 we can see the FWHM of the momentum distributions in **x** and **y** for the three studied species (nitrogen, oxygen and fluorine) with the lead target, after subtracting the particular intrinsic resolution of the FRS for each case. The error bars are considerably large, making difficult any possible quantitative analysis of the data. This is due to the fact that the transversal components are much more sensitive to the reaction mechanism than the longitudinal component is. As a consequence, the dispersion is more important, and the errors associated to the angle of emission of the core fragments in x and y just after the breakup target are also larger.

The values obtained for the FWHM's (within the error bars) fall in the area

Table 4.7: Values of FWHM's (with their corresponding errors) assigned (by direct evaluation on the histogram) to the transversal momentum distributions (in **y**) of the different isotopes of nitrogen, oxygen and fluorine after a **one-neutron removal breakup reaction** on a **carbon** target (FWHM[y]) compared to the *Gaussian* fits (g-FWHM[y]). The normalized χ^2s of the *Gaussian* fits, and the RMS of each distribution are also shown.

Fragment	RMS[y] (MeV/c)	FWHM[y] (MeV/c)	g-FWHM[y] (MeV/c)	$\chi^2[y]/ndf$
^{16}N	103.	194. $\pm$ 29.	224.	11.6
^{17}N	107.	191. $\pm$ 29.	233.	6.7
^{18}N	105.	234. $\pm$ 28.	234.	14.3
^{19}N	104.	229. $\pm$ 28.	227.	17.5
^{18}O	111.	244. $\pm$ 30.	244.	3.0
^{19}O	111.	243. $\pm$ 30.	243.	3.5
^{20}O	114.	254. $\pm$ 28.	254.	6.7
^{21}O	113.	253. $\pm$ 28.	253.	5.9
^{22}O	105.	217. $\pm$ 31.	217.	4.6
^{21}F	117.	261. $\pm$ 30.	261.	3.2
^{22}F	119.	264. $\pm$ 29.	264.	8.1
^{23}F	111.	221. $\pm$ 37.	221.	1.9
^{24}F	106.	177. $\pm$ 34.	215.	8.1
^{25}F	100.	177. $\pm$ 51.	177.	3.8

that we expected from the data obtained with the carbon target.

We record in table 4.8 the values of the FWHM's (with their corresponding errors) assigned to the transversal momentum distributions (in **x** and **y**) of the different isotopes of nitrogen, oxygen and fluorine after a **one-neutron removal breakup reaction** on a **lead** target (which have been obtained by direct evaluation on the histogram) after subtracting the intrinsic resolution of the FRS compared to the *Gaussian* fits. The RMS of each distribution is also shown. The main error sources here are the same as for the transversal components with a carbon target, but the statistics is lower and the intrinsic resolution of the FRS with this target worse introducing a larger error.

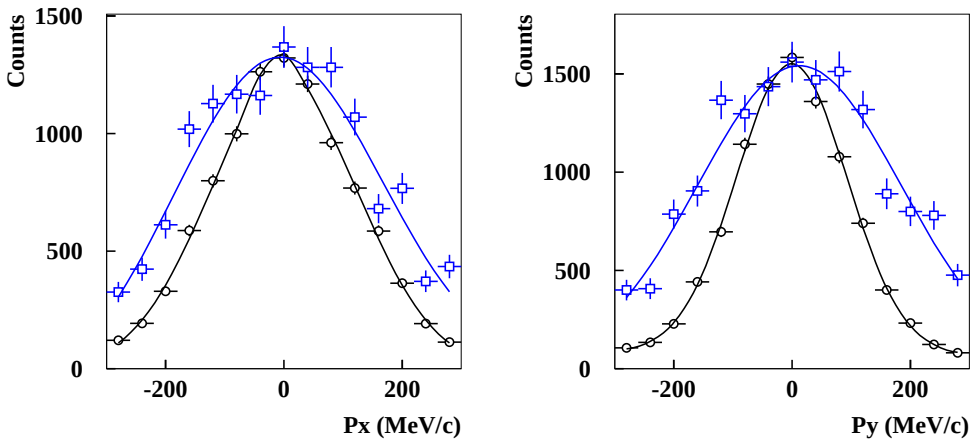

Figure 4.9: Comparison between the measured transversal momentum distributions (Left panel: in the x-direction. Right panel: in the y-direction) of ^{22}O after one-neutron removal on a carbon (open circles) and on a lead target (open squares). Both distributions have been normalized arbitrarily in order to compare their profiles in a proper way. The results presented here have not been corrected by the intrinsic resolution of the FRS yet.

4.2.2.3 Two-neutron removal on a carbon target: projectiles ^{21}N, ^{24}O and ^{27}F

We show in table 4.9 the values of the FWHM's (with their corresponding errors) assigned to the momentum distributions in **z**, **x** and **y** (after subtracting the intrinsic resolution of the FRS that corresponds for each case), to the different isotopes of nitrogen, oxygen and fluorine after a **two-neutron removal breakup reaction** on a **carbon** target (which have been obtained by direct evaluation on the histogram) compared to the *Gaussian* fits. The RMS of each distribution is also shown. The low statistics is the main error source associated to these measurements. Additional error sources are the ones already mentioned in the case of the *one-neutron removal case*.

The intrinsic resolution FWHM is around 191 MeV/c, 129 MeV/c and 35 MeV/c for P_x, P_y and P_z, respectively.

We will center our discuss here on the core fragment longitudinal momentum distributions data: In the case of ^{19}N and ^{22}O, we observe quite broad momentum distributions, while the situation is the opposite in the case of ^{25}F. This last nuclide comes from ^{27}F, which we pointed out as a "possible" two-neutron halo when we discussed the two-neutron removal cross-sections in section 4.1.2.

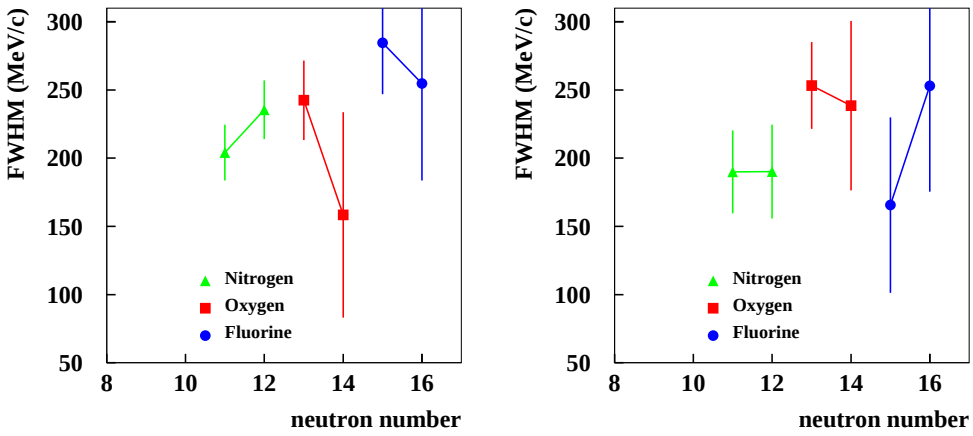

Figure 4.10: Left panel: FWHM's of the transversal momentum distribution in the x-direction for different isotopes of nitrogen (triangles), oxygen (squares) and fluorine (circles) after one-neutron removal on a lead target. We represent in the x-axis the number of neutrons of the isotope, and in the y-axis the corresponding FWHM. Right panel: FWHM's of the transversal momentum distribution in the y-direction, represented with the same conventions as left.

It is clear that a two-neutron removal reaction, that happens mainly in two steps, is not so simple as a one-neutron removal reaction, and the considerations that allowed us to "translate" a narrow momentum distribution into a spatially extended wave function of the removed neutron when it was still in the projectile in the case of the one-neutron removal cannot be used here. In conclusion we can only point out that the different behaviour presented by the momentum distribution of ^{25}F, compared to the other two cases studied here (^{19}N and ^{22}O), implies that the **internal structure** of ^{27}F and the **reaction mechanism** that transforms it into ^{25}F, are quite different (both neutrons, or at least one of them) to those of the other two studied cases. This fact, together with the value obtained for the two-neutron removal cross-section of ^{27}F, the particular behaviour presented by ^{26}F in the one-neutron removal, and finally, the proximity of the neutron dripline, promote interest in a dedicated study around such fluorine isotopes in order to establish definitive conclusions.

Table 4.8: Values of FWHM's (with their corresponding errors) assigned (by direct evaluation on the histogram) to the transversal momentum distributions (in **x** and **y**) of the different isotopes of nitrogen, oxygen and fluorine after a **one-neutron removal breakup reaction** on a **lead** target (FWHM[x] and FWHM[y]) compared to the *Gaussian* fits (g-FWHM[x] and g-FWHM[y]). The normalized χ^2s of the *Gaussian* fits, and the RMS of each distribution are also shown.

Fragment	RMS[x] (MeV/c)	FWHM[x] (MeV/c)	g-FWHM[x] (MeV/c)	$\chi^2[x]/ndf$
^{18}N	132.	204. ± 20.	204.	3.5
^{19}N	135.	235. ± 21.	235.	3.8
^{21}O	141.	242. ± 29.	242.	2.7
^{22}O	139.	158. ± 75.	158.	2.7
^{24}F	149.	284. ± 38.	284.	3.8
^{25}F	148.	255. ± 71.	255.	3.0
Fragment	RMS[y] (MeV/c)	FWHM[y] (MeV/c)	g-FWHM[y] (MeV/c)	$\chi^2[y]/ndf$
^{18}N	130.	190. ± 30.	190.	3.2
^{19}N	131.	190. ± 34.	190.	1.3
^{21}O	139.	253. ± 32.	253.	2.7
^{22}O	141.	238. ± 62.	238.	2.4
^{24}F	142.	166. ± 64.	166.	3.2
^{25}F	151.	253. ± 78.	253.	3.6

4.3 γ-ray spectra of core fragments of projectiles $^{17-21}$N, $^{19-24}$O and $^{21-27}$F

The γ-ray spectrum of a nucleus provides information concerning its excited states. In this section, we will present all relevant γ-ray spectra obtained with our NaI array for fragments arising from specific studied reaction channels.

Level schemes contained in the *Table of Isotopes*, *Richard B. Firestone* [Fir96], proved to be very useful in the interpretation of our results.

The following γ-ray spectra were recorded:

- ^{16,17,18,19}N resulting from ^{17,18,19,20}N, with a carbon target
- ^{18,19,20,21,22}O resulting from ^{19,20,21,22,23}O, with a carbon target

Table 4.9: Values of FWHM's (along with their corresponding errors), assigned (by direct evaluation on the histogram) to the momentum distributions in **z**, **x** and **y** of different isotopes of nitrogen, oxygen and fluorine following a **two-neutron removal breakup reaction** on a **carbon** target (FWHM[i]) in comparison to the *Gaussian* fits (g-FWHM[i]). The normalized χ^2's of *Gaussian* fits, and the RMS of each distribution are also shown.

Fragment	RMS[z] (MeV/c)	FWHM[z] (MeV/c)	g-FWHM[z] (MeV/c)	$\chi^2[z]/ndf$
^{19}N	85.	187. $\pm$ 10.	187.	18.5
^{22}O	94.	218. $\pm$ 11.	218.	3.4
^{25}F	70.	127. $\pm$ 11.	140.	2.6
Fragment	RMS[x] (MeV/c)	FWHM[x] (MeV/c)	g-FWHM[x] (MeV/c)	$\chi^2[x]/ndf$
^{19}N	122.	267. $\pm$ 35.	267.	4.6
^{22}O	115.	212. $\pm$ 44.	212.	4.3
^{25}F	113.	118. $\pm$ 71.	118.	3.4
Fragment	RMS[y] (MeV/c)	FWHM[y] (MeV/c)	g-FWHM[y] (MeV/c)	$\chi^2[y]/ndf$
^{19}N	112.	249. $\pm$ 31.	249.	5.1
^{22}O	113.	237. $\pm$ 34.	237.	6.4
^{25}F	116.	170. $\pm$ 39.	170.	5.7

- ^{21,22,23,24,25}F resulting from ^{22,23,24,25,26}F, with a carbon target
- ^{18,19}N resulting from ^{19,20}N, with a lead target
- ^{21,22}O resulting from ^{22,23}O, with a lead target
- ^{24,25}F resulting from ^{25,26}F, with a lead target
- ^{19}N resulting from ^{21}N, with a carbon target
- ^{22}O resulting from ^{24}O, with a carbon target
- ^{25}F resulting from ^{27}F, with a carbon target

The low statistics, intrinsic to secondary beam reaction products, together with the limited geometrical coverage of the array only made it possible to observe *clear* peaks in the spectra of ^{17,19}N, ^{20,22}O and ^{21}F. This was specially true in the case of *one-neutron removal* reaction with carbon target. For *one-neutron*

removal with lead target, and *two-neutron removal* with carbon target, the statistics were a real limitation, and only in the case of ^{19}N a sharp peak appeared in the spectrum.

If we assume that the reaction is so peripherical that fragments are not excited in it, the observation of peaks in the γ-ray spectrum for certain fragments would indicate that these fragments were previously in an excited state while inside the projectile.

We will now proceed to describe the obtained γ-ray spectra.

4.3.1 γ-ray spectra of core fragments of projectiles ^{18}N and ^{20}N

In figure 4.11 we can see the level scheme of ^{17}N (core fragment after one-neutron removal on ^{18}N). If we examine the γ-ray spectrum recorded during the experiment (figure 4.11, right), a peak at approximately $1400\ keV$ can be seen. This peak corresponds to the γ-ray emitted in de-excitation from the first excited state to the ground state. In the level scheme, we see that energy corresponding to this γ-ray is $1373.8\ keV$. It is also possible to observe what appears to be a small "peak" at approximately $1800\ keV$ (corresponding to the $1849.5\ keV$ level de-exciting to the ground state). However, as that fact is not clear, and in the event that a real peak had occurred, its contribution would be minimal, and we will not be considering it.

Examining the level scheme, we find no other γ ray with an energy that could fit inside the observed peak. Therefore, we conclude that only the first excited state and the ground state contribute in a significant way to the ^{18}N configuration and are thus populated in a non negligible way.

^{19}N (core fragment after one-neutron removal on ^{20}N) presents a similar situation. In the γ-ray spectrum (see figure 4.12, right) we observe only one peak at approximately $1100\ keV$. It corresponds to the de-excitation of the first excited state to the ground state, by emission of a $1120\ keV$ γ ray (figure 4.12, left). We have, in this case, assumed that either the level at $1590.0\ keV$ is not populated, or is populated in a negligible way.

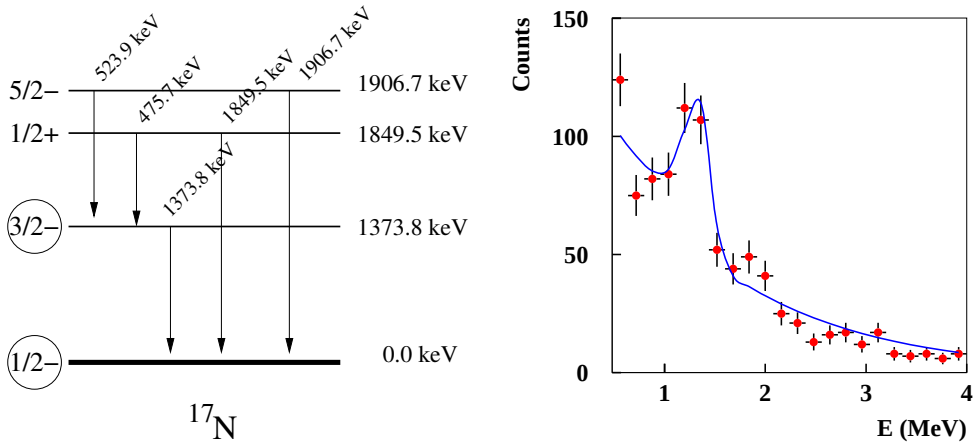

Figure 4.11: Left panel: level scheme of ^{17}N [Fir96]. The states populated in our experiment have spin and parity surrounded by a circle. Right panel: experimental γ-ray energy spectrum of ^{17}N produced after a one-neutron removal breakup reaction on ^{18}N using a carbon target. The dots signify experimental data, while the curve corresponds to a GEANT simulation.

4.3.2 γ-ray spectra of core fragments of projectiles ^{21}O and ^{23}O

The right side of figure 4.13 shows the γ-ray spectrum of ^{20}O (core fragment after one-neutron removal on ^{21}O). Again, a single peak can be appreciated, however it is in fact a combination of two γ rays, as has already been discussed in the previous chapter, corresponding to the energies of 1637.7 and $1932.3\ keV$ (figure 4.13 -left-).

When a ^{20}O nucleus in the first excited state (at $1637.7\ keV$) de-excites, it emits a γ ray of $1637.7\ keV$. If the second excited state is populated (at $3570.0\ keV$), then two γ rays of 1932.3 and $1637.7\ keV$ are emitted in cascade.

To determine whether or not the second excited state is populated in the reaction, we compared the experimental γ-ray spectrum to the spectrum obtained using a GEANT simulation. Simulation under the asumption that two γ rays of 1637.7 and $1932.3\ keV$ with emission probabilities of 100% and (80±20)%, respectively, were emitted, provided the best agreement.

Let us now focus on the ^{22}O (core fragment after one-neutron removal on ^{23}O) spectrum, where we have the added difficulty that there is no level scheme available at [Fir96]. The γ-ray spectrum obtained in our experiment presented

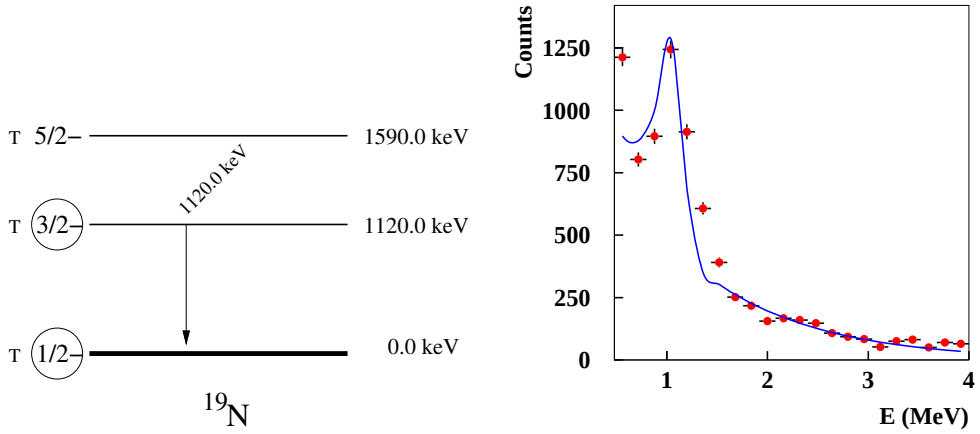

Figure 4.12: Left panel: Level scheme of ^{19}N [Fir96]. The states populated in our experiment have spin and parity surrounded by a circle. Spins and parities assigned to the different levels are theoretical predictions taken from [Sau03] (this fact is indicated by T located on the left of the assignment). Right panel: experimental γ-ray energy spectrum of ^{19}N produced after a one-neutron removal breakup reaction on ^{20}N using a carbon target. The dots signify experimental data, while the curve corresponds to a GEANT simulation.

low efficiency and energy resolution (see figure 4.14 -left-), consequentially, it was not possible to deduce experimentally the level scheme from our measurements. Instead, we chose to work with results from a recent experiment performed at GANIL [Sor01, Sta03], and the predictions of recent shell model calculations [Bro03]. The proposed level scheme is shown in figure 4.14 -left-, where we find three excited states located at 3100, 4400 and 5700 keV. Based on the favourable agreement between the experimental spectrum and the GEANT simulation (figure 4.14 -right-), we assume that these three states, together with the ground state, are the main ^{22}O configurations contributing to the ^{23}O ground state. The first excited state de-excites to the ground state, whereas the second and third excited states de-excite to the first excited state. The energies of emitted γ rays are 3100, 1300 and 2600 keV, respectively.

In the GEANT simulation we assumed three γ rays of energies 1300, 2600 and 3100 keV and their emission probabilities were set to (40$\pm$10)%, (30$\pm$10)% and 100%, respectively, in order to match the experimental spectrum.

Due to severe Doppler broadening that we had in our experiment, γ rays of energy as different as 2600 and 3100 keV could become mixed and appear as only one broad peak in the spectrum. This results in an experimental spectrum

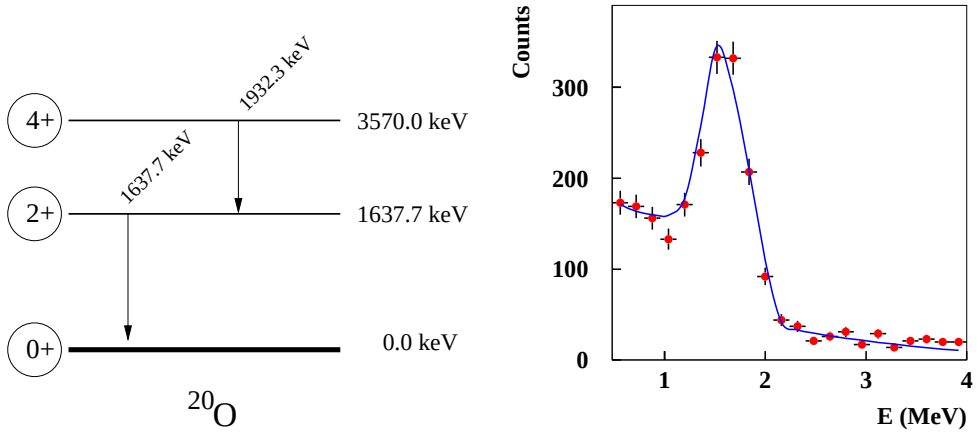

Figure 4.13: Left panel: Level scheme of ^{20}O [Fir96]. The states populated in our experiment have the spin and parity surrounded by a circle. Right panel: experimental γ-ray energy spectrum of ^{20}O produced after a one-neutron removal breakup reaction on ^{21}O using a carbon target. The dots are the experimental data, the curve corresponds to a GEANT simulation.

with only two peaks: one at $1300\ keV$ and other at $2800\ keV$ (the experiment which took place at GANIL was performed at lower energies and with high resolution germanium detectors. These two factors allowed for the observation of the three peaks at the energy spectrum).

4.3.3 γ-ray spectrum of core fragment of projectile ^{22}F

^{21}F (core fragment after one-neutron removal on ^{22}F) is the last case where we can appreciate a clear peak. On the right side of figure 4.15 we see only one peak, while we suspect that three γ rays contribute to it.

This can be understood when we examine the *rather* complex level scheme (for the lowest excited states) of ^{21}F, this is presented on the left side of figure 4.15.

Examining the γ rays present in the level scheme, we can identify three that match the experimentally observed peak:

- γ ray of $1450.3\ keV$, emitted from the third excited state moving to the first excited state

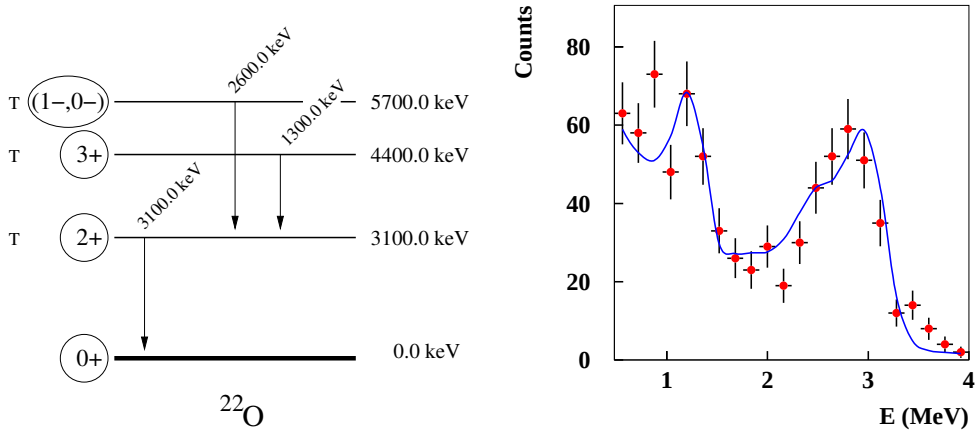

Figure 4.14: Left panel: Level scheme of ^{22}O deduced from results obtained at GANIL [Sor01, Sta03] and from theoretical predictions based in shell model calculations [Bro03]. The states of ^{22}O that contribute to the ^{23}O nuclear structure have a circle surrounding their corresponding spin and parity (the parentheses are set when the spin and parity assignment is not clear). T indicates that the assignment is a theoretical prediction. Right panel: γ-ray energy spectrum of ^{22}O produced after a one-neutron removal breakup reaction of ^{23}O on a carbon target, obtained in the experiment. The dots signify experimental data, while the curve corresponds to a GEANT simulation.

- γ ray of $1730.3\ keV$, emitted from the third excited state moving to the ground state
- γ ray of $1754.9\ keV$, emitted from the fourth excite state moving to the ground state

Again, we had to rely on the GEANT simulation to establish the contribution of each γ ray to the peak. We looked for the configuration which provided the best agreement between the experimental and the simulated spectrum. We obtained it using γ-ray emission probabilities equal to 20%, 100% and 20%, respectively. The uncertainties were in this case quite high and difficult to estimate, due to the fact that there were three γ rays contributing to the same peak.

Another possibility can be that the fourth excited state is not populated, with contribution from two γ rays only.

It is difficult to establish the value for the emission probability of γ rays resulting from de-excitation of the fourth excited state. This is due to the energy of those γ rays, which is very similar to $1730.3\ keV$ (energy of γ rays emitted by

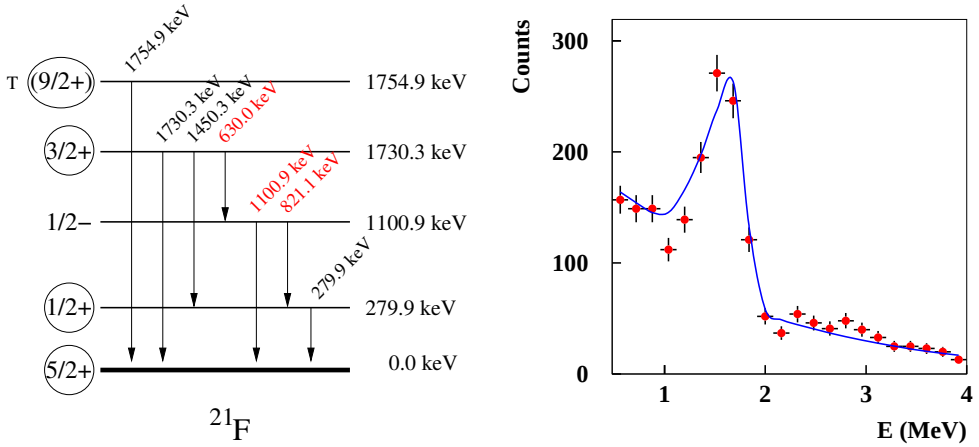

Figure 4.15: Left panel: Level scheme of ^{21}F [Fir96]. The states populated in our experiment have spin and parity surrounded by a circle. T indicates that the assignment is a theoretical prediction, taken in this case from [Sau03]. Right panel: experimental γ-ray energy spectrum of ^{21}F produced after a one-neutron removal breakup reaction on ^{22}F using a carbon target. The dots signify experimental data, while the curve corresponds to a GEANT simulation.

de-excitation from the third excited state). If we remove, in the GEANT simulation, the contribution of $1754.9\ keV$ γ rays to the peak, we do not appreciate a great difference. We suspect that this difference can be masked by statistical errors in the experimental spectrum.

^{21}F Levels up to the fourth excited state appear to contribute to the ^{22}F ground state configuration. Therefore, we should see in the spectrum additional peaks corresponding to other emitted γ rays (see figure 4.15 -left-).

The first excited state (see figure 4.15 -left-) in ^{21}F is located at only $279.9\ keV$. This transition is not observed in the spectrum. To justify this fact, we assume that the first excited state of ^{21}F does not contribute significantly to the ground state configuration of ^{22}F, and suspect that the corresponding peak in the γ-ray spectrum is mixed with the background, which is very important at low energies.

With respect to the remaining γ rays of energies equal to 630.0, 821.1 and $1100.9\ keV$, we do not observe them in our spectrum as they were not observed in previous measurements [Fir96].

4.3.4 Final considerations

It is interesting to note that only γ-ray spectra of fragments with an even number of neutrons present strong peaks. This also appears to be indepentent of the reaction, as can be observed for ^{19}N, where we had sufficient statistics for comparison between the three studied reactions: $^{20}N \longrightarrow ^{19}$N on a carbon target, $^{20}N \longrightarrow ^{19}$N on a lead target, and $^{21}N \longrightarrow ^{19}$N on a carbon target.

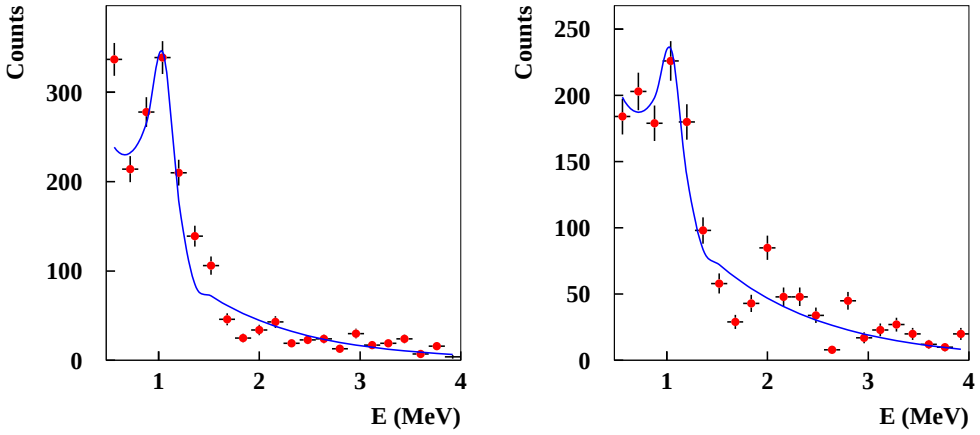

Figure 4.16: Left panel: experimental γ-ray energy spectrum of ^{19}N produced after a one-neutron removal breakup reaction of ^{20}N on a lead target. The peak is not as sharp (while not being less pronounced) than that obtained with the carbon target, due to the low statistics we have in this case. Right panel: experimental γ-ray energy spectrum of ^{19}N produced after a two-neutron removal breakup reaction of ^{21}N on a carbon target. It is more difficult to identify the peak in this situation as a result of the low statistics and the high neutron background we now have (it is important to remember that this is a **two** neutron breakup reaction).

In figure 4.12 we have shown the γ-ray spectrum of ^{19}N after one-neutron removal from ^{20}N on carbon. If we examine now figure 4.16 (Left panel: ^{19}N after one-neutron removal from ^{20}N on lead. Right panel: ^{19}N after two-neutron removal from ^{21}N on carbon), we can see that the difference is almost non-existent, and is probably due to changes in the amount of neutron background (depending on the reaction) and to the different statistics.

4.4 Coincidences between γ rays and momentum distributions of core fragments

In this section we will present the core fragment longitudinal momentum distributions, gated by the previously mentioned γ-ray spectra, configurating what we call "the coincidences". The experimental method used to obtain the coincidences was described in chapter **3**.

The coincidences represent a further advance in the study of the exotic projectile structure: The core fragment inside the projectile can be in different states. At this stage, it is important to determine which core fragment configurations take part in, and how much do they contribute to, the ground state structure of the projectile. Coincidences are complex observables which allow us to **experimentally extract** the cross-sections and momentum distributions for different configurations of the fragment inside the projectile.

We have already seen that the momentum distribution of the fragment after the reaction is related to the quantum state of the fragment while it formed part of the projectile. It would be possible, in principle, to obtain the angular momentum related to the fragment from this momentum distribution. Unfortunately, in some cases the ground state of the projectile is a combination of different states of the fragment. In addition to this, the inclusive momentum distribution (the momentum distribution obtained without the coincidence) results to be a mixture from which it is difficult to extract quantitative information. The solution to this problem is the coincidence, which disentangles the states and gives separated momentum distributions for each configuration.

In order to apply the coincidence method to a certain nucleus we record the corresponding core fragment γ-ray spectrum. If there is no peak at the spectrum, we must *assume* that the projectile is composed of a single configuration, with the core being in the ground state.

As outlined in section 4.3, five exotic projectiles corresponded to core fragment γ-ray spectra exhibiting peaks: ^{18,20}N, ^{21,23}O and ^{22}F. We will discuss them separately in the following sections.

4.4.1 Projectile ^{18}N

The γ-ray spectrum of ^{17}N (core fragment after breakup from ^{18}N) presents one peak generated by a single γ ray (see figure 4.11). We face the simplest case in the analysis of the coincidences in order to separate between configurations involving fragments in the *ground* and the *excited state*.

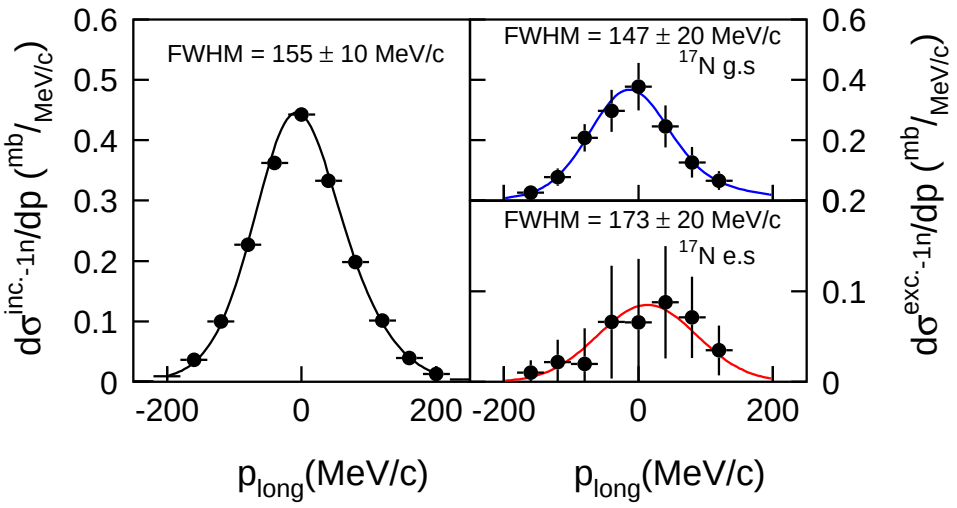

Figure 4.17: Total (left), ground state (right, top) and first excited state (right, bottom) contribution to the longitudinal momentum distribution of ^{17}N after a one-neutron removal breakup reaction from ^{18}N on a carbon target.

We have proceeded as we detailed in chapter **3**. The result can be seen in figure 4.17, where we present the *total*, the *ground state* and the *excited state* momentum distributions of ^{17}N. The distributions are normalized to the removal cross-section that corresponds to each channel.

We can observe that the main contribution to the total momentum distribution is due to the configuration where the ^{17}N fragment is in the ground state, accounting for the **(79±22)%**. The excited state represents the **(21±22)%**.

From the beginning we have assumed that the breakup reaction is peripheral and thus the core is not affected by it. Considering this we can conclude that ^{17}N must be in a superposition of two states inside ^{18}N ground state, being the predominant contribution the ^{17}N ground state.

The profiles of the momentum distributions (see table 4.10) could be used to extract information related to the angular momentum configuration of the valence neutron.

Table 4.10: Values of FWHM's (with their corresponding errors) assigned (by direct evaluation over the histogram) to the total, the ground state, and the first excited state contribution to the longitudinal momentum distribution of ^{17}N after a **one-neutron removal breakup reaction** from ^{18}N on a **carbon** target (FWHM) compared to the *Gaussian* fits (g-FWHM). The normalized χ^2s of the *Gaussian* fits, and the RMS of each distribution are also shown.

Distribution	RMS (MeV/c)	FWHM (MeV/c)	g-FWHM (MeV/c)	χ^2/ndf
Total	73.	154. $\pm$ 10.	168.	4.5
G.S.	72.	146. $\pm$ 20.	164.	0.3
E.S.	78.	172. $\pm$ 20.	171.	0.1

The corresponding one-neutron removal cross-sections for considered reaction channels (in which the core fragment is produced in different states) are presented in table 4.11.

Table 4.11: Experimental one-neutron removal cross-sections (σ_{-1n}) of ^{18}N, for the considered reaction channels, in which the core fragment (^{17}N) is produced in different states (E_c). The total one-neutron removal cross-section is also shown.

E_c (MeV)	σ_{-1n} (mb)
0	59. $\pm$ 19.
1.4	16. $\pm$ 17.
$\sum$	75. $\pm$ 11.

The obtained values indicate a clear contribution of **d** wave to the angular momentum of the valence neutron of ^{18}N (before the breakup) when the core is in the excited state, and a probable (but not definite, as the value is not determinant) **s** wave when the core is in the ground state.

We will accept, as working hypothesis, that when the ^{17}N core is in the ground state, the valence neutron should be predominantly in the $2s_{1/2}$ level, and when

it is in the excited state, the valence neutron should be mainly in a d state, such as $1d_{5/2}$, or $1d_{3/2}$.

4.4.2 Projectile ^{20}N

^{19}N (core fragment after breakup from ^{20}N) presents a similar situation to ^{17}N. We have observed one peak at the spectrum, which results from a single γ ray (see figure 4.12).

We present in figure 4.18, the *total*, the *ground state* and the *excited state* momentum distributions of this nuclide. The distributions are normalized to the corresponding removal cross-sections. The largest contribution to the total momentum distribution comes from the ground state, with **(58±15)%** probability. The excited state accounts for **(42±15)%**.

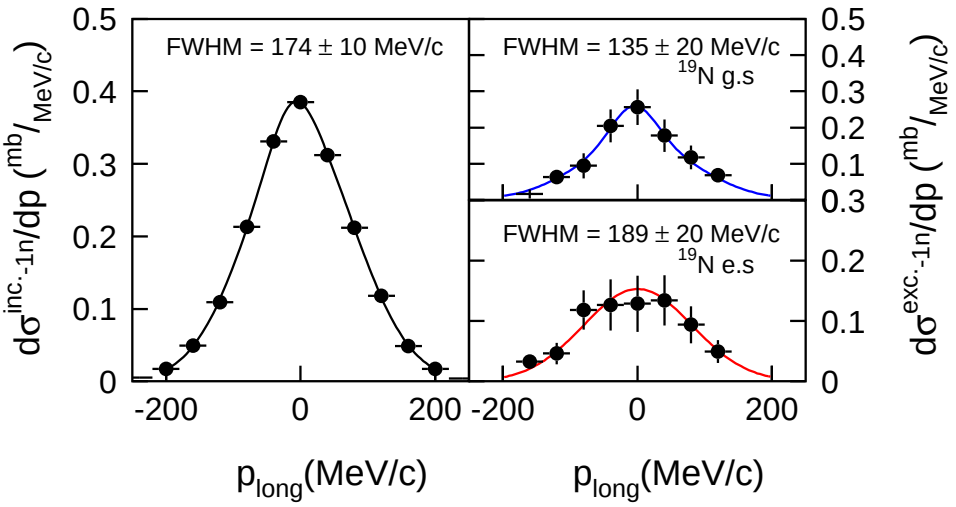

Figure 4.18: Total (left), ground state (right, top) and first excited state (right, bottom) contribution to the longitudinal momentum distribution of ^{19}N after a one-neutron removal breakup reaction from ^{20}N on a carbon target.

Examining the profile of the momentum distributions (see table 4.12), we could attempt to extract information related to the angular momentum configuration of the valence neutron.

Table 4.12: Values of FWHM's (with their corresponding errors) assigned (by direct evaluation over the histogram) to the total, the ground state, and the first excited state contribution to the longitudinal momentum distribution of ^{19}N after a **one-neutron removal breakup reaction** from ^{20}N on a **carbon** target (FWHM) compared to the *Gaussian* fits (g-FWHM). The normalized χ^2s of the *Gaussian* fits, and the RMS of each distribution are also shown.

Distribution	RMS (MeV/c)	FWHM (MeV/c)	g-FWHM (MeV/c)	χ^2/ndf
Total	79.	173. $\pm$ 10.	184.	9.7
G.S.	79.	134. $\pm$ 20.	187.	0.5
E.S.	83.	188. $\pm$ 20.	189.	0.3

Corresponding one-neutron removal cross-sections for the considered reaction channels, in which the core fragment is produced in different states, are presented in table 4.13.

Table 4.13: Experimental one-neutron removal cross-sections (σ_{-1n}) of ^{20}N, for the considered reaction channels, in which the core fragment (^{19}N) is produced in different states (E_c). The total one-neutron removal cross-section is also shown.

E_c (MeV)	σ_{-1n} (mb)
0	42. $\pm$ 12.
1.1	31. $\pm$ 12.
$\sum$	73. $\pm$ 10.

The data also outlines a clear **d** wave contribution ($1d_{5/2}$ or $1d_{3/2}$) to the angular momentum of the valence neutron of ^{20}N (before the breakup) when the core is in the excited state. For the ground state, the main contribution appears to be an **s** wave ($2s_{1/2}$).

4.4.3 Projectile ^{21}O

The situation with this nuclide is more complicated. Two γ rays contribute to the peak in the γ-ray spectrum where we have established our gate for the coincidence method (see figure 4.13).

Analysis of the corresponding γ-ray spectrum allows us to determine contributions to the peak, that can be due to:

- ^{20}O in the first excited state that decays to the ground state by emitting one γ ray. The ratio in this case is: one state to one γ ray
- ^{20}O in the second excited state, that decays to the first excited state, then to the ground state. In this situation, we have two γ rays of similar energy (that contribute to the same peak) emitted in cascade and a single original excited state. The ratio is in this situation: one state to two γ rays

One problematic situation arises, previously commented in chapter **3**: The solution is to use a $\rho \neq 1$ in the determination of the momentum distribution for the core fragment excited states, in order to arrive at the correct number of events.

From the GEANT simulation it is possible to obtain the probability for the emission of the two γ rays contributing to the observed peak (100% and 80% with a total error of $\pm$20%). The total efficiency of the array at the energy of the peak is estimated to be (5.38$\pm$0.54)%. We can therefore apply formula 3.11 to determine the ρ factor:

$$\rho = 1.00 + 0.80 - 2 \cdot 0.0538 \cdot 0.80 = 1.71 \tag{4.1}$$

Using this value in our analysis, we obtain results that are presented in figure 4.19. We represent the *total*, the *ground state* and the *excited state* momentum distributions. The distributions are normalized to the removal cross-section that corresponds to each channel.

In figure 4.19 we can see that the distributions corresponding to the ground state and to the excited states contribute in similar quantities to the total distribution. The ground state accounts for **(53$\pm$15)%**, with the excited states making up the remaining **(47$\pm$15)%**.

Profiles of the momentum distributions indicate that the main contribution to the angular momentum configuration of the valence neutron inside the projectile is a **d** wave for the core fragment ground and excited states.

The profiles of the momentum distributions (see table 4.14) could be used to extract information related to the angular momentum configuration of the valence neutron.

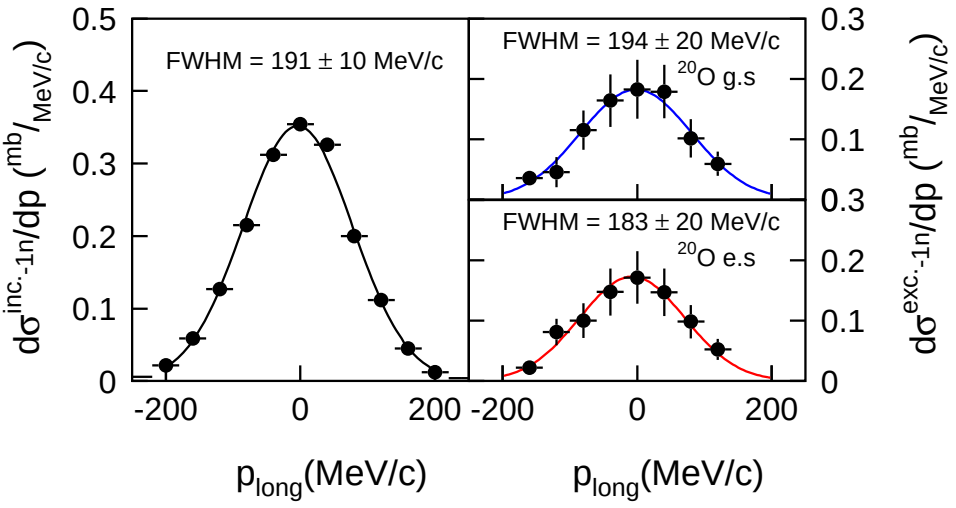

Figure 4.19: Total (left), ground state (right, top) and excited states (right, bottom) contribution to the longitudinal momentum distribution of ^{20}O after a one-neutron removal breakup reaction from ^{21}O on a carbon target.

Table 4.14: Values of FWHM's (with their corresponding errors) assigned (by direct evaluation over the histogram) to the total, the ground state, and the first excited state contribution to the longitudinal momentum distribution of ^{20}O after a **one-neutron removal breakup reaction** from ^{21}O on a **carbon** target (FWHM) compared to the *Gaussian* fits (g-FWHM). The normalized χ^2s of the *Gaussian* fits, and the RMS of each distribution are also shown.

Distribution	RMS (MeV/c)	FWHM (MeV/c)	g-FWHM (MeV/c)	χ^2/ndf
Total	84.	190. ± 10.	196.	4.6
G.S.	83.	193. ± 20.	194.	0.2
E.S.	79.	182. ± 20.	182.	0.2

The corresponding one-neutron removal cross-sections for considered reaction channels, in which the core fragment is produced in different states, are presented in table 4.15. The contribution of each excited state has been calculated with the corresponding branching ratio provided by the GEANT simulation.

The data enable us to conclude that the ^{21}O ground state can be explained as an admixture of ^{20}O core in the ground state coupled to a valence neutron in the $1d_{5/2}$ level, and ^{20}O core in the first two excited states coupled again to

Table 4.15: Experimental one-neutron removal cross-sections (σ_{-1n}) of ^{21}O, for the considered reaction channels, in which the core fragment (^{20}O) is produced in different states (E_c). The total one-neutron removal cross-section is also shown.

E_c (MeV)	σ_{-1n} (mb)
0	38. ± 12.
1.6	6.8 ± 7.2
3.6	27. ± 12.
$\sum$	71.9 ± 8.9

a neutron in the $1d_{5/2}$ level. Another (less probable) possibility for both configurations is that the neutron is in $1d_{3/2}$, however, this level is quite high in the energy spectrum (above the $2s_{1/2}$ level).

In the case of oxygen isotopes, our method gains the following advantage: we have an even-even nucleus decaying after the reaction. We know that its ground state spin and parity is 0^+, and (if there is no **low energy** intruder state) 2^+ and 4^+ correspond to first and second excited states, respectively.

In addition, it is simple to calculate the ground state configuration of the exotic projectile, because there is only one possibility to combine the angular momentum information that we have from the core and the valence neutron. In this case we obtain $J^\pi = 0^+ \otimes 5/2^+ = 5/2^+$ (or perhaps $0^+ \otimes 3/2^+ = 3/2^+$, though this is less probable). For excited states, more possibilities are applicable.

A further difficulty with this nuclide is the fact that the profile of the momentum distribution corresponding to excited states is due to the superposition of the first and the second excited states, in a proportion of *approximately* 20% and 160% (2x80%, as a result of the cascade), respectively (according to the GEANT simulation). The profile of the distribution and the FWHM indicate a **d** wave predominance (valence neutron before breakup in a $1d_{5/2}$ or a $1d_{3/2}$) that can be attributed mainly to a situation where the core is in the second excited state. When the core is in the first excited state, the situation is not as clear, however, a similar configuration for the valence neutron could be anticipated.

In our coincidence method we subtracted the distribution involving any excited state of the core fragment from the total one, in order to obtain the core fragment ground state momentum distribution. The subtracted distribution is not the true excited state momentum distribution, but a distorted one, produced

by the double-weighted contribution of the second excited state (the true excited state momentum distribution should contain *approximately* 20% of first excited state and 80% of second excited state). The fact that both excited states appear to correspond to a similar **d** wave configuration is very important, as it allows us to neglect the effect of this systematic error in the fragment ground state momentum distribution profile.

4.4.4 Projectile ^{23}O

^{22}O (core fragment after breakup from ^{23}O) is probably the most interesting studied case, because from it we can determine information relating to the exotic and controversial ^{23}O.

The γ-ray spectrum of ^{22}O allows us to observe two peaks (see figure 4.14). In order to extract, from the total momentum distribution, the contribution of the ground and the excited states of the core fragment, we apply the coincidence method and establish a gate around the peak at $2800\ keV$. This peak is generated by two γ rays with energies of 2600 and $3100\ keV$. We then assign (based on the GEANT simulation) emission probabilities equal to 30% (with a total error of $\pm$10%) and 100%, respectively. The total efficiency of the array at the energy of the peak at $2800\ keV$ is estimated to be (4.79$\pm$0.48)%.

The $3100\ keV$ γ ray can be emitted due to:

- ^{22}O in the first excited state that decays to the ground state. The ratio being: *one* state to *one* γ ray
- ^{22}O in the second excited state that decays to the first excited state, and then to the ground state. The energy of the two γ rays is very different, therefore, they do not contribute to the same peak and the ratio is: *one* state to *one* γ ray at the peak
- ^{22}O in the third excited state that decays to the first excited state, and then to the ground state. Both γ rays contribute to the same peak, to bring the ratio to: *one* state to *two* γ rays. The other γ ray that contributes to the peak has an energy of $2600\ keV$

A factor $\rho \neq 1$ must be used in establishing the momentum distribution of core fragment excited states. This is because two γ rays are emitted in cascade and contribute to the same peak. In this case, the value of ρ will be:

$$\rho = 1.00 + 0.30 - 2 \cdot 0.0479 \cdot 0.30 = 1.27 \tag{4.2}$$

Figure 4.20 represents the *total*, the *ground state* and the *excited state* core fragment momentum distributions. The distributions are normalized to the removal cross-section that corresponds to each channel.

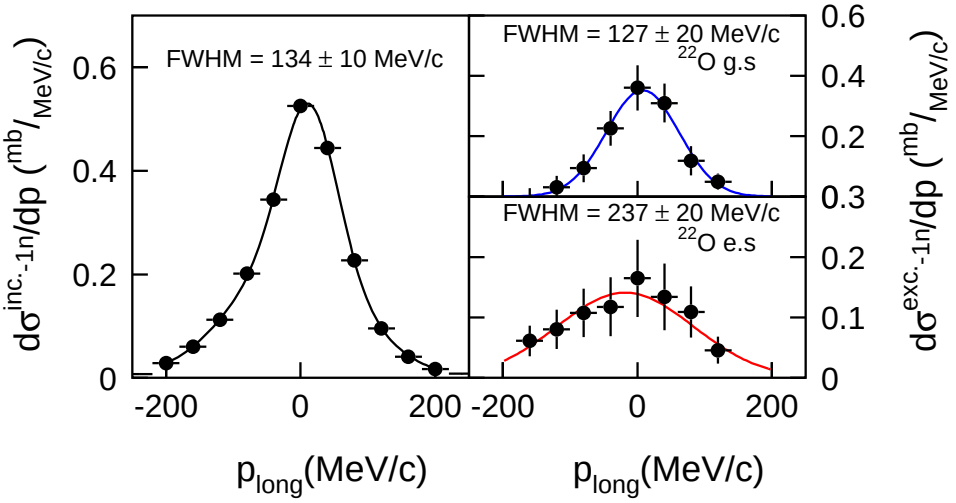

Figure 4.20: Total (left), ground state (right, top) and excited states (right, bottom) contribution to the longitudinal momentum distribution of ^{22}O after a one-neutron removal breakup reaction from ^{23}O on a carbon target.

With respect to the relative contributions of the different states to the total core fragment momentum distribution, the situation is very similar to results obtained for ^{20}O: ground state and excited states contribute in almost equal quantities. The percentages established in this case are **(59±18)%** and **(41±18)%**, respectively.

The profiles of the momentum distributions (see table 4.16) could be used to extract information related to the angular momentum configuration of the valence neutron.

The corresponding one-neutron removal cross-sections for the considered reaction channels, in which the core fragment is produced in different states, are presented in table 4.17. The contribution of each excited state has been obtained

Table 4.16: Values of FWHM's (with their corresponding errors) assigned (by direct evaluation over the histogram) to the total, the ground state, and the first excited state contribution to the longitudinal momentum distribution of ^{22}O after a **one-neutron removal breakup reaction** from ^{23}O on a **carbon** target (FWHM) compared to the *Gaussian* fits (g-FWHM). The normalized χ^2s of the *Gaussian* fits, and the RMS of each distribution are also shown.

Distribution	RMS (MeV/c)	FWHM (MeV/c)	g-FWHM (MeV/c)	χ^2/ndf
Total	78.	133. $\pm$ 10.	171.	19.4
G.S.	70.	126. $\pm$ 20.	125.	0.1
E.S.	88.	236. $\pm$ 20.	237.	0.2

with the corresponding branching ratio obtained using the GEANT simulation.

Table 4.17: Experimental one-neutron removal cross-sections (σ_{-1n}) of ^{23}O, for the considered reaction channels, in which the core fragment (^{22}O) is produced in different states (E_c). The total one-neutron removal cross-section is also shown.

E_c (MeV)	σ_{-1n} (mb)
0	50. $\pm$ 18.
3.1	10.5 $\pm$ 6.2
4.4	14.0 $\pm$ 7.6
5.7	10.5 $\pm$ 6.2
$\sum$	85. $\pm$ 15.

If we examine profiles of the momentum distributions with values of the FWHM's, it is clear that **when the core is in the ground state inside the ^{23}O isotope, the valence neutron has to be mainly in the $2s_{1/2}$ level** to explain the observed narrow distribution.

This is a result of great importance, as ^{23}O ground state spin and parity is still under discussion. Results based on different experiments, which unfortunately provide indirect data that must be helped by theoretical models for the assignment, yield to contradictory assignments.

Thus we proceed to the calculation of the ground state configuration of ^{23}O. As ^{22}O is an even-even nucleus, ^{23}O ground state spin and parity will be:

$$J^{\pi} = 0^{+} \otimes 1/2^{+} = 1/2^{+} \tag{4.3}$$

With respect to excited states, the same problem of the core fragment momentum distribution generated by a superposition of various core excited states arises here. In this case, three states contribute: first, second and third, in a proportion of *approximately* 30%, 40% and 60% (2x30%, caused by the cascade), respectively. Also, the profile of the distribution and the FWHM indicate a **d** wave predominance. The fact that the three excited states contribute in similar quantities, and the substantial value of the FWHM ($199 \pm 20\ MeV/c$) almost excludes any **s** wave neutron contribution related to the excited states.

It must also be noted that the distorted part is not very significant (*around* 30% of 130%). Therefore, we do not expect much change to the profile of the excited momentum distribution.

Based on these two substantial reasons, the effects of the distortion in the ground state momentum distribution profile can, again, be neglected. Therefore, we can conclude that we can trust our results.

4.4.5 Projectile ^{22}F

The situation with this nuclide is not as complicated as it could appear in principle. Examining the level scheme of ^{21}F (figure 4.15, left) we can observe a large quantity of levels de-exciting via γ-ray emission (with more than one de-excitation channel occurring in some cases). However, based on the experimental γ-ray spectrum, we will assume that after the one-neutron breakup reaction of ^{22}F, only the ground, the third excited, and (possibly) the fourth excited state of ^{21}F are populated.

Assuming that the first excited state is not directly populated but only (or at least, mainly) the result of a de-excitation cascade moving through it. This supposition is based on the fact that we cannot confirm the peak corresponding to the de-excitation of this level in the γ-ray spectrum obtained in our experiment. The important background present at these low energies (approximately $279\ keV$) can mask the emission probability of 20%, that has its origin in the de-excitation of the third excited state to the first excited state, and consequent de-excitation of this level. However, the background would not have the capacity to mask an additional non-negligible contribution from a direct population (non-negligible is intended to signify approximately 10%. This would result in a

new emission probability of approximately 30%).

As previously discussed in section 4.3.3., it is presumed that the second excited state is not populated. To clarify the concept we would like to mention that there was no observation of any peak at the energies of the two γ rays that can be emitted from the de-excitation of that level.

Considering these hypotheses, we proceed to analyze the situation and apply our coincidence method. Realizing that **there is no necessity** for a factor $\rho \neq 1$. If we set a gate at the peak that we observe in the γ-ray spectrum, we will be selecting *the core fragment excited states that contribute to the ^{22}F ground state configuration* (the fourth -if populated-, and third excited states). If we look now at the level scheme we see that the ratio is in this case **one excited state** to **one** γ **ray at the peak**, as there is no conflictive de-excitation cascade.

Prior to interpreting the results, it is important to note the fact that it is not vital for the application of the method whether or not the fourth excited state is populated in the reaction. This is due to the fact that it does not affect the general required situation:

- the gate at the γ-ray spectrum selects all core fragment excited states that contribute to the ^{22}F ground state configuration
- the ratio between the number of excited states and emitted γ rays that are included in the gated peak is **one** to **one**

Figure 4.21 provides the results of applying our coincidences method to ^{21}F, with the considerations that we mentioned previously. The *total*, the *ground state* and the *excited state* core fragment momentum distributions are represented. The distributions are normalized to the removal cross-section which corresponds to each channel.

In this case the ground state makes the largest contribution to the total momentum distribution, with a ratio of **(69$\pm$13)%**. The third and fourth excited states account for the remaining **(31$\pm$13)%**. This means that the predominant configuration within the ^{22}F projectile is that in which the ^{21}F core is in the ground state.

Examining the profile of momentum distributions (see table 4.18) we could attempt to extract information related to the angular momentum configuration of the valence neutron.

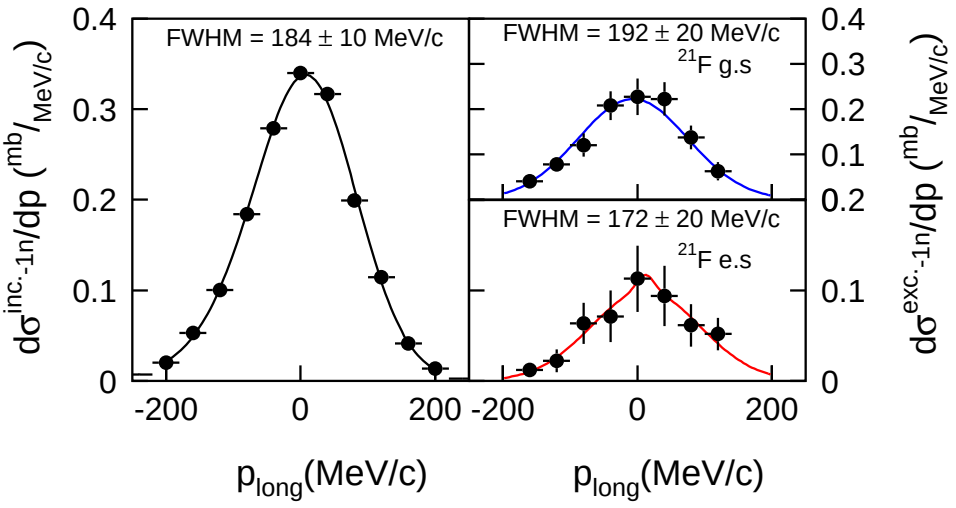

Figure 4.21: Total (left), ground state (right, top) and excited states (right, bottom) contribution to the longitudinal momentum distribution of ^{21}F after a one-neutron removal breakup reaction from ^{22}F on a carbon target.

Table 4.18: Values of FWHM's (with their corresponding errors) assigned (by direct evaluation over the histogram) to the total, the ground state, and the first excited state contribution to the longitudinal momentum distribution of ^{21}F after a **one-neutron removal breakup reaction** from ^{22}F on a **carbon** target (FWHM) compared to the *Gaussian* fits (g-FWHM). The normalized χ^2s of the *Gaussian* fits, and the RMS of each distribution are also shown.

Distribution	RMS (MeV/c)	FWHM (MeV/c)	g-FWHM (MeV/c)	χ^2/ndf
Total	82.	183. ± 10.	189.	16.2
G.S.	81.	191. ± 20.	192.	0.5
E.S.	82.	171. ± 20.	187.	0.2

The corresponding one-neutron removal cross-sections for the considered reaction channels, in which the core fragment is produced in different states, are presented in table 4.19.

It appears that the main configuration is a **d** wave for both, ground and excited state, as can be deduced from the large value of the FWHM's. We can therefore expect, from a single particle point of view, that the valence neutron is in the $1d_{5/2}$ level when the core is in the ground state, inside the projectile.

Table 4.19: Experimental one-neutron removal cross-sections (σ_{-1n}) of ^{22}F, for the considered reaction channels, in which the core fragment (^{21}F) is produced in different states (E_c). The total one-neutron removal cross-section is also shown.

E_c (MeV)	σ_{-1n} (mb)
0	46. $\pm$ 11.
1.7	21. $\pm$ 9.2
$\sum$	67.1 $\pm$ 9.8

In the case of the excited states, there is a superposition of the third and (possibly) the fourth excited state. We can anticipate a population ratio **much higher** for the third excited state, which dominates the longitudinal momentum distribution. Neglecting the influence of the fourth excited state, we conclude, from the inspection of the FWHM's, that the neutron is also in the $1d_{5/2}$ level when the core is in the third excited state.

Chapter 5

Experimental data compared to theory

This chapter is devoted to the interpretation of experimental results by means of theoretical calculations. To achieve this we need to obtain infomation relating to the structure of the different involved nuclei (matter density and wave function of the valence neutron) and a correct description of the reaction mechanism. Many different attempts were made to describe nuclear structure and reaction mechanism. These approaches follow a Glauber model description of the reaction mechanism and differ mainly in the nuclear structure part used in the model calculations. We would like to mention two of them. The first approach [Mad01] uses Gaussian core and target densities for the profile functions. The valence neutron wave function is obtained from a Woods-Saxon potential, using a single particle calculation. This model has been used to investigate the exotic projectiles ^{16,17,19}C [Mad01], and, more recently, has been applied to ^{23}O [Cor03b]. The second approach is based on Shell Model calculations (OXBASH code) and was used to describe experimental results by E. Sauvan *et al.* [Sau03]. In this work, ^{23}O was also studied, together with its neighbours in the oxygen isotopic chain.

The current calculations were obtained using a QRPA/QP-C model developed by *Horst Lenske* [Len90, Eck90, Len03a], whereas the description of the reaction mechanism was accomplished using a Glauber model [Gla55, Gla59, Bar96, Hen96, Bar97, Fes91, Bar00, Lvo01]. We will begin this chapter with a description of necessary ingredients to perform this model calculation. The interested reader can find a more detailed description of the models used, in appendix **A**. We will then evaluate observables measured in the experiment using these models. Finally, we will attempt to draw conclusions from comparisons between theory and experiment.

In this chapter we will concentrate on the description of the oxygen isotopic chain, particularly in ^{21,23}O, exotic projectiles for which we used the coincidence method to separate the ground from the excited states of the corresponding core fragment.

5.1 Theoretical framework

5.1.1 Nuclear structure description

A description of the various theoretical tools used in structure calculations is outlined in this section. We will begin our discussion by noting that we have worked with the formalism of the second quantization [Hey94] (see appendix **A.1**), because it allowed us to work with nucleons (fermions) in a very simple way. In this context, angular momentum can be included where it is needed, and two or more particles can be easily coupled with the help of the Clebsh-Gordan coefficients. We also used the particle-hole picture, where one can simplify expressions to work only with valence particles and holes. It is also important to mention **Wick's theorem** as a great aid in obtaining expected values, because it provides the equivalent in **normal order** (with the creation operators on the left, and the destruction operators on the right) and **contractions** (expected values of pairs of operators in the reference state) of any product of operators.

The second quantization formalism automatically separates the nuclear Hamiltonian into a mean field, long range interaction, which maintains the nucleons in their single particle orbitals, and a short range, residual interaction. The mean field contribution to the expected value of the Hamiltonian directly gives the system of Hartree-Fock (HF) equations (see appendix **A.2**). The residual interaction is mainly a pairing force which tends to scatter the nucleons from their single particles orbitals and form pairs preferably with total $J^\pi = 0^+$ (this is also valid for particle-hole pairs). The pair formation affects the remainder of the nucleus, and if the pairing force is sufficiently strong, it can permanently modify its structure, causing a softening of the Fermi surface.

The preference of the pairing force to form $J^\pi = 0^+$ pairs restores the spherical symmetry of the nucleus. The probability of $J^\pi = 2^+$ pairs formation is considerably smaller, and other configurations result negligible. This fact causes the lowest state (ground state) in even-even nuclei to be 0^+ [May50, Flo52, Rac52, Tal52], and the existance of a big gap (increasing with pairing strength)

between this state and the others. Pairing correlations are stronger in nuclei with non-closed shells, as it is easier to excite nucleons inside a shell, also in the case of low density nuclear matter (dripline nuclei). It is clear then that, for many nuclei, pairing correlations play a fundamental role, giving rise to collective states and modifying the single particle energies, and should be taken into account.

Pairing correlations must be noted for causing a situation whereby the interacting particles are not at definite orbitals, but constantly changing, in such a way that their future energies and wave functions depend on their present energies (this "dependence" is called "self-energy") [Len03b].

Three types of residual interactions are mainly used for calculations [Hey94]: effective two-body matrix elements, where all the parameters remain free, realistic interactions, derived from free nucleon-nucleon interaction, and phenomenological interactions, chosen in such a way that they match the experimental results. We worked with effective two-body matrix elements (this was favored by the second quantization formalism since it uses operators defined by matrix elements).

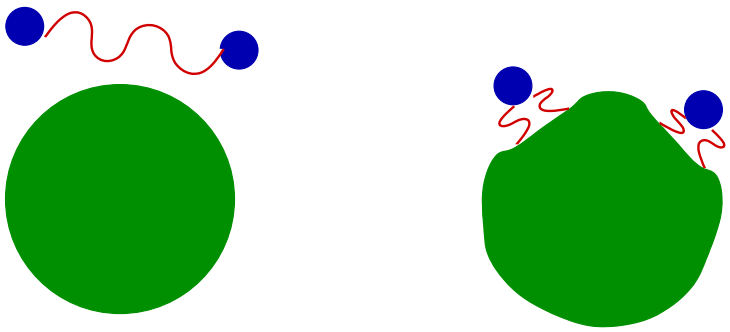

Figure 5.1: Schematic plot representing how the short range pairing correlations between two particles (left) are absorbed in the redefinition of the ground state (deformation of the shape observed in the right picture).

The permanent modification in the structure of the ground state, resulting from the pairing force, can be treated with the help of the superconducting theory (BCS) [Hey94], which redefines the working basis by changing particle and hole operators into quasiparticle operators by means of the canonical Bogoljubov-Valatin transformation (see appendix **A.3**). The net effect of this change in the basis is the masking of the main part of the pairing force, which becomes absorbed by the quasiparticle operators and the superconducting (BCS) ground state (see figure 5.1). This has an important consequence: the BCS ground

state does not present a constant number of nucleons (grand canonical ensemble); only the mean value of the number operator is conserved, by requirement of the BCS ground state definition. Therefore, it is not possible to talk about "particles in the different levels", and we must refer to "occupation probabilities".

The quasiparticle picture proposed by the BCS theory has the advantage that particle (p) and hole (h) dynamics are treated symmetrically, with both types of excitations described in a unified way. This means that 3-QP excitations can describe $3p$, $2p-1h$, $1p-2h$, or $3h$ excitations.

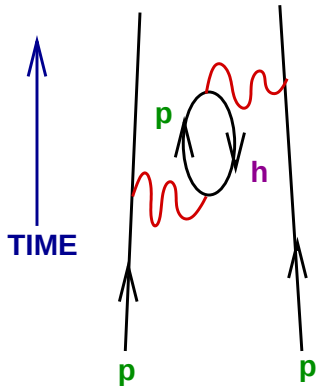

Figure 5.2: Basic diagram (in the single particle picture) contributing to the renormalization of the effective interaction between two particles (p) by particle-hole (p-h) correlations. The loop corresponds to the appearance of a virtual dipole (p-h) which polarizes the nuclear medium (core polarization).

When the (BCS) ground state is established, we can proceed to determine different excited states. For even-even nuclei we can use the Quasiparticle Random Phase Approximation (QRPA) [Hey94, Len03a], which treats the ground and the excited states in a consistent way (see appendix **A.4**). QRPA defines the excitations in terms of operators that act on the ground state by creation and destruction of QuasiParticle (QP) pairs (see figures 5.2 and 5.3).

The effective residual interaction used with QRPA was in our case a density dependent interaction derived from central parts of the $M3Y$ G-matrix [Ber77] by using the DME approximation of *Negele* [Neg74] for the exchange contributions, where the strengths in the different spin-isospin channels were adjusted to reproduce the *Landau-Migdal* parameters [Spe77] in nuclear matter.

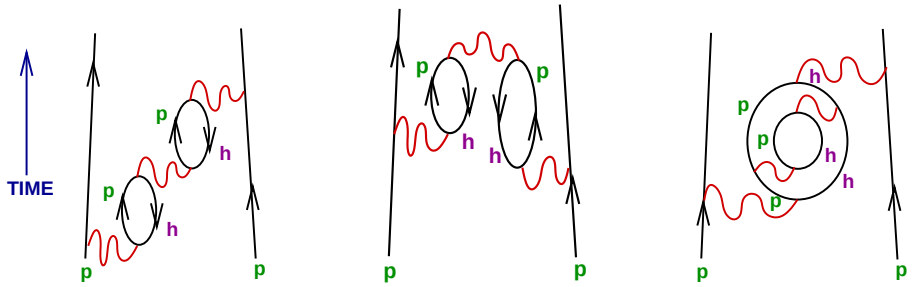

Figure 5.3: Additional polarization diagrams in the single particle picture. From left to right, the first diagram corresponds to the case of quasiboson creation operators only made of pairs of QP creation operators. The second diagram corresponds to general quasiboson creation operators (able to create and destroy pairs of QP). Normal QRPA presents these two basic types of diagrams, although additional corrections can be considered that give rise to higher order QRPAs. This is the case of the third diagram with the "screening" effect, which causes a decreasing in the strength of the pairing correlations.

QRPA is assumed to be valid in the limit of small pairing correlations, where the operators that create and destroy the excited states fulfill approximately boson conmutation relations (quasiboson aproximation [Lan64]). This condition is normally forced by choosing a new ground state for the quasiboson operators. As a consequence, the BCS ground state (named from now "quasiparticle vacuum", since it is no longer the ground state) and the QRPA ground state will differ by admixtures of at least 4-QP. In figure 5.4 we present a schematic plot of the QRPA ground state.

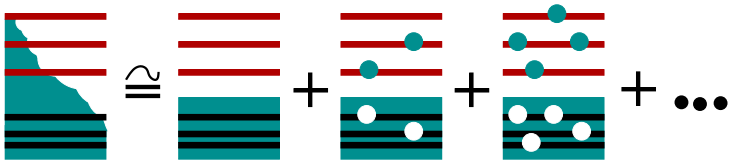

Figure 5.4: Schematic plot of the QRPA ground state (left) interpretation as a superposition (right) of the HF ground state plus two particle-two hole excitations. On the left side of the equation we have used the quasiparticle picture, while on the right side the single particle picture has been chosen for illustrative purposes.

Pairing correlations can present different properties depending on the spin (S) and isospin (T) of the state, resulting in some cases attractive and in other

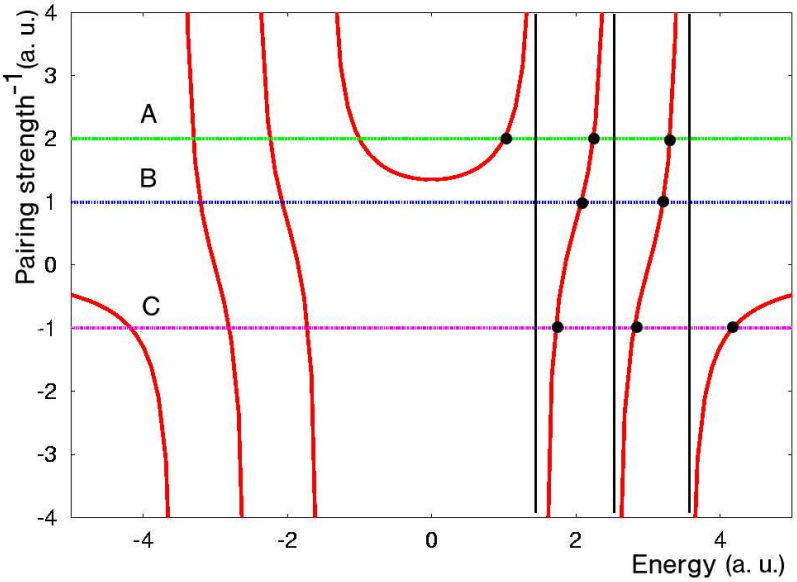

Figure 5.5: Schematic representation of how the QRPA levels behave with respect to the pairing strength. Only the curve for positive energies corresponds to physical solutions. In the example plotted here, the three single particle levels (vertical lines) at energies 1.5, 2.5 and 3.5 (arbitrary units) obtained with HF are modified in such a way that depends on the character and strength of the pairing interaction. Line **A** represents an attractive pairing interaction of strength 2 (arbitrary units). We can see that its net effect is to shift levels to lower energies (black points), specially the lowest one (collective state). If we increase the pairing strength (line **B**), the solution for the collective level becomes complex. This can be interpreted as a growing instability in the vibrational nature of the state and the appearance of a permanent deformation. Finally, line **C** corresponds to a repulsive interaction which shifts the states to higher energies, specially the highest one, which is collective and, if it trespasses the particle emission threshold it becomes a resonance.

cases repulsive. *In general*, because of the short-range attractive character of the nucleon-nucleon interaction, the particle-hole interaction is attractive in light nuclei for $T = 0$ states and repulsive for $T = 1$ states [Row70]. The response of the energy levels calculated with QRPA to this different behaviour is demonstrated in figure 5.5, together with additional considerations relating to QRPA modifications to the single particle levels obtained with HF.

Odd nuclei are considered as composed of two parts: an even-even core described by QRPA and a valence particle (proton or neutron). In order to account for the pairing interaction in a correct form, 1- and 3-QP excitations are

considered. This is achieved with the QuasiParticle-Core coupling model (QP-C) [Len90, Eck90, Len03a]. The 1-QP component couples the core ground state to one quasiparticle, while the 3-QP component couples quasiparticles to core excited states.

The QP-C model follows very closely the QRPA formalism and forces anti-conmutation relations for the quasifermion operators which create the different states of the odd nucleus from the even-even core. It is important to mention that this model, uses as ground state the QRPA ground state (which is not the same as the quasiparticle vacuum), this also makes it possible to obtain 1- and 3-QP excitations by destroying 1-QP and 3-QP in the ground state, similar to what occurred with QRPA. Therefore, the quasifermion creation operators must be composed of linear combinations of 1- and 3-QP creation and destruction operators if we want to cover all the possibilities. Another important characteristic of this model is that the 1-QP component is composed of contributions from different major shells that have the same J^{π}. As a consequence, the "correlated single particle wave functions" for the valence particle (QP-C) will be linear combinations of single particle wave functions (HF) from different major shells (energy mixing). These "correlated single particle wave functions" are what remains from the static mean-field configuration (HF). The remainder of the full wave function is composed of a multitude of configurations where the valence particle is rescattered into other orbitals by interactions with the core [Len03b]. When approaching the dripline, this second part of the wave function becomes more important. This means that, in addition to the static mean-field binding, it is gaining influence another one type of binding due to correlations between the core and the valence neutron (core polarization). For nuclei close to the dripline this last contribution could become dominant (i. e. halo nuclei). Should this happen, shell structures will begin to dissolve and a simple description in terms of a static mean-field plus a residual interaction is no longer acceptable.

Working within this theoretical framework, we performed calculations for oxygen isotopes, obtaining wave functions related to different configurations. Oxygen isotopes are an interesting isotopic chain to study since they have **Z** magic number, alternating even and odd **A**, some nuclei are very close to the dripline (^{22,23}O), a possible shell closure appears (at $N = 16$) for ^{24}O, and the halo candidate ^{23}O is contained in the isotopic chain.

5.1.2 Reaction mechanism description

The reaction occurred at very high energies ($\sim 1AGeV$). Therefore, it is possible to make use of the semiclassical (or *eikonal*) approximation [Fes91, Bar96, Hen96, Bar97, Bar00, Lvo01] to calculate the exotic projectile cross-sections and core fragment momentum distributions. In this approximation the particle "follows a semiclassical path", and when interacting it is dispersed at "forward angles". The *eikonal approximation* (name borrowed from Optics) is also referred to as the **Glauber model** [Gla55, Gla59].

We will focus on the one-neutron removal reaction channel on a carbon target. For our purposes, we have restricted ourselves to **stripping** (the core remains unaffected, the neutron is absorbed) and **diffractive breakup** (the core remains unaffected, the neutron is scattered in an unbound state), neglecting Coulomb breakup. We have also assumed that the projectile does not have bound excited states (what can affect the *diffractive breakup* channel), based on the small expected diffraction contribution (in the order of $10 - 20\%$ the stripping channel [Bar97, Lvo01]). We will consider in the following discussion that *diffractive breakup* and *diffraction* account for the *same* process.

Another simplification consisted in consider the target "structureless", and treat the projectile as composed of two "structureless" parts (core and valence neutron) described as incoming plane waves with the same momentum and outcoming waves with complex phase shifts (*eikonal* waves). Each complex phase shift was obtained independently of an optical potential resulting from the convolution of densities of the target and the corresponding projectile component (zero range interaction). The part of the outcoming wave due to the phase shift is called **profile function**. We can interpret it as an operator which provides what rests of the wave function after the interaction if we apply it to the wave function in the entrance channel. The profile function concept is the basis for the calculation of the cross-section for different reaction channels.

We could treat the projectile components as "independent" because we are working at very high energies where the "frozen limit" approximation can be used. This means that core and neutron do not have time to change their relative positions during the "fast" interaction, and are seen by the potential as "independent" (although the probability that the neutron is at a certain position with respect to the core during the reaction is given by the square norm of its wave function).

We give now a **detailed** description of the path followed to obtain the strip-

ping and diffraction exotic projectile cross-sections and the core fragment momentum distributions for the stripping reaction channel. In the following discussion, the cross-sections (σ) are given in mb, the positions (r) in fm, and the momenta (k) in fm^{-1}. We will use the labels "in" and "out" to refer to the particle wave function *before* and *after* the reaction, respectively. In the space where the reaction takes place we define a Cartesian coordinate system (x, y, z).

The wave function (ψ) for a free particle moving in the z direction with momentum $\hbar k$ can be written as:

$$\psi_{in} = N \cdot e^{ikz} \tag{5.1}$$

Where N is a normalization factor, that we will obviate for the moment. The Schrödinger equation is:

$$H\psi = E\psi \tag{5.2}$$

Which can also be writen in the explicit form:

$$-\frac{h^2}{2m}\nabla^2\psi = (E - V)\psi \tag{5.3}$$

Another way of expressing the wave function is by specifying its dependence with the "action" S (the lagrangian integrated over the time):

$$\psi = e^{iS/\hbar} \tag{5.4}$$

This form is useful, since it is the starting point for the semiclassical (or *eikonal*) approximation [Wen26, Kra26, Bri26]. We first write the "action" as a serie of powers of $\hbar$:

$$S = \sigma_0 + \hbar\sigma_1 + \hbar^2\sigma_2 + \dots \tag{5.5}$$

The semiclassical (or *eikonal*) approximation means that $\hbar \to 0$. We can use it because the beam energy is much higher than the interaction potential. If we substitute the "action" in the Schrödinger equation and cut the serie that results at first order in $\hbar$, we obtain the equation:

$$\nabla\sigma_0 = \sqrt{2m(E - V)} \tag{5.6}$$

Now we make use of the forward-scattering approximation, and only consider variations with respect to the longitudinal component (z). Solving for σ_0, and remembering that $V \ll E$ (semiclassical -or *eikonal*- approximation, $E \approx \frac{\hbar^2 k^2}{2m}$) we obtain:

$$\sigma_0 = \int_{-\infty}^{z} dz' \cdot \sqrt{2m(E-V)} \approx \int_{-\infty}^{z} dz' \cdot (\hbar k - \frac{1}{v}V) \tag{5.7}$$

Where we have made use of the first order approximation of $\sqrt{1+x}$ when $x \to 0$, and denoted the speed of the particle by v. By substituting in the expression 5.4 it results:

$$\psi(x,y,z) = e^{i\delta_0} \cdot e^{ikz+i\chi} \tag{5.8}$$

Where δ_0 is a constant phase which appears after the integration. The other extra phase χ is given by the expression:

$$\chi(x,y,z) = -\frac{1}{\hbar v}\int_{-\infty}^{z} dz' \cdot V \tag{5.9}$$

If we put the condition that the wave function in absence of interaction is ψ_{in} it is required that $\delta_0 = 0$. If the interaction potential is localized in one area, once the particle is outside it, we can write its "wave function" as:

$$\psi(b,z)_{out} = e^{ikz+i\chi(b)} \tag{5.10}$$

Where now $\chi(b)$ is given by:

$$\chi(b) = -\frac{1}{\hbar v}\int_{-\infty}^{\infty} dz' \cdot V \tag{5.11}$$

And $b = \sqrt{x^2+y^2}$.

We have assumed that the problem has cylindrical symmetry (spherical interacting particles). With these considerations we can write:

$$\psi(b,z)_{out} = S(b) \cdot e^{ikz} \tag{5.12}$$

Where the profile function [Bar96, Hen96, Bar97, Bar00, Lvo01] $S(b) = e^{i\chi(b)}$ can be regarded as a factor which distorts the wave function due to the presence of an interaction usually represented by an optical potential. In this work we will make use of the *so called* **zero range approximation**, which allows us to define the following optical potential [Ber99, Lvo01]:

$$V = -\frac{i}{2}\hbar v \frac{\bar{\sigma}_{NN}}{10}\int d^3\vec{r}_0 \cdot A_P\rho_P(\vec{r}_0)A_T\rho_T(\vec{r}-\vec{r}_0) \tag{5.13}$$

In this expression densities (ρ_P, for the particle, and ρ_T, for the target) are given in fm^{-3} and are normalized to unity. Their corresponding mass numbers

are A_P and A_T. The factor 10 dividing the average nucleon-nucleon cross-section [Ray79, Lvo01] ($\bar{\sigma}_{NN}$) is needed to convert from mb to fm^2. The mean total nucleon-nucleon interaction is obtained as:

$$\bar{\sigma}_{NN} = \frac{\tilde{\sigma}_{nn}(N_T N_P + Z_T Z_P) + \tilde{\sigma}_{np}(N_T Z_P + Z_T N_P)}{A_T A_P} \tag{5.14}$$

Where Z_P and Z_T are the atomic numbers corresponding to particle and target, respectively, and $\tilde{\sigma}_{ij} = \sigma_{ij} \cdot (1 - i\alpha_{ij})$, denote complex cross-sections for the nucleon-nucleon interaction made of the corresponding real cross-sections (σ_{ij}) and the imaginary-to-real ratios (α_{ij}).

We have made use of the **optical theorem** to obtain expression 5.13. For a detailed discussion of how this can be done see [Ber99].

The potential is a complex function. The real part does not change the norm of the particle wave function and is related to the elastic scattering. The imaginary part changes the norm of the wave function and is related to all the inelastic processes.

The probability that the particle survives after the interaction, for a given impact parameter (b), is given by [Bar96, Bar97, Bar00]:

$$P^s(b) = < \psi_{out} | \psi_{out} > = < \psi_{in} | (|S(b)|^2) | \psi_{in} > \tag{5.15}$$

Explicitly (and recalling the normalization factor N):

$$P^s(b) = N^2 \cdot |S(b)|^2 \int d^3\vec{r} \cdot |e^{ikz}|^2 = |S(b)|^2 \tag{5.16}$$

The absorption probability during the interaction is given by:

$$P^a(b) = 1 - P^s(b) = 1 - |S(b)|^2 \tag{5.17}$$

Let us assume two *non interacting* particles **1** (core) and **2** (valence nucleon) moving in the z direction (*frozen limit approximation*) with the same momentum $\hbar k$ that pass through the interaction area without changing their relative positions [1]. Having particle **1** an impact parameter b_1, the stripping probability of particle **2** when it is located at a given position with respect to particle **1** can be written as the multiplication of two probabilities:

- the probability that particle **1** survives and particle **2** is absorbed (f_2^{str})

[1] Note that outside the *frozen limit* approximation, particles **1** and **2** do interact, being ϕ the wave function of particle **2** with respect to particle **1**

- the probability to find particle **2** in that specific position relative to particle **1** ($|\phi|^2$)

If we integrate over all possible particle **2** positions, we obtain the stripping probability for a given particle **1** impact parameter b_1:

$$P^{str}(b_1) = \int d^3\vec{r} \cdot |\phi(\vec{r})|^2 \cdot f_2^{str} \tag{5.18}$$

In this equation $\vec{r} = \vec{r}_2 - \vec{r}_1$ (see figure 5.6). This causes that the integration over $\vec{r}$ for a fixed $\vec{r}_1$ removes the dependence over $\vec{r}_2$. We define f_2^{str} as:

$$f_2^{str} \equiv P_1^s(b_1) \cdot P_2^a(b_2) = |S_1(b_1)|^2 \cdot (1 - |S_2(b_2)|^2) \tag{5.19}$$

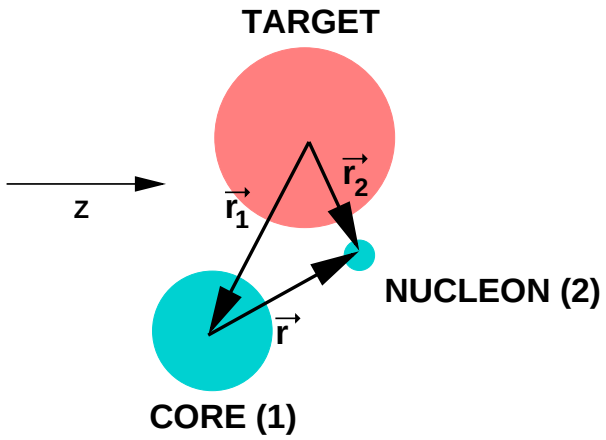

Figure 5.6: Coordinate system used in the Glauber model calculations.

In order to calculate the **stripping cross-section** [Bar96, Hen96, Bar97, Bar00, Lvo01] it is necessary to evaluate the integral of the stripping probability for all possible impact parameters b_1, and average over the different possible magnetic quantum numbers of particle **2**:

$$\sigma^{str} = \frac{10}{2j+1} \sum_m 2\pi \int_0^\infty b_1 db_1 \cdot P^{str}(b_1) \tag{5.20}$$

The factor 10 is necessary to convert from fm^2 to mb.

In order to obtain the diffraction cross-section, we start from the formula 5.12, which gives the distorted wave function after the interaction. We will assume again two particles. The wave function (before the interaction) associated to

particle **1** is again a plane wave, while the wave function associated to particle **2** is made of the usual plane wave and a *slow* motion component with respect to particle **1** (this slow motion component will be represented by ϕ):

$$\psi_{in} = e^{ikz} \cdot \phi \tag{5.21}$$

The scattered part of the wave function can be written as:

$$\begin{aligned} |\psi_{scatt.}> = |\psi_{out}> - |\psi_{in}> = \\ = (S_2(b_2) - 1)|\psi_{in}> \end{aligned} \tag{5.22}$$

The probability that particle **2** has been dispersed and is still in the ground state after the interaction is given by [Bar96, Bar97, Bar00]:

$$\begin{aligned} P_2^{g.s.}(b_2) = |<\psi_{scatt.}|\psi_{out}>|^2 = \\ = |<\psi_{in}|S_2(b_2) - 1|\psi_{in}>|^2 \end{aligned} \tag{5.23}$$

On the other side, the probability to end up in an excited state is:

$$\begin{aligned} P_2^{e.s.}(b_2) = |<\psi_{e.s.}|\psi_{out}>|^2 = \\ = |<\psi_{e.s.}|S_2(b_2) - 1|\psi_{in}>|^2 \end{aligned} \tag{5.24}$$

Which can also be expressed (provided that there are not bound excited states) using the full basis of wave functions ($|\psi_{all}>$):

$$\begin{aligned} P_2^{e.s.}(b_2) = |<\psi_{all}|S_2(b_2) - 1|\psi_{in}>|^2 - \\ - |<\psi_{in}|S_2(b_2) - 1|\psi_{in}>|^2 \end{aligned} \tag{5.25}$$

The first term, after some manipulations, can be written as:

$$\begin{aligned} |<\psi_{all}|S_2(b_2) - 1|\psi_{in}>|^2 = \\ =<\psi_{in}||S_2(b_2) - 1|^2|\psi_{in}> \end{aligned} \tag{5.26}$$

Where we have used that $|\psi_{all}>$ is a complete basis. Finally we can write the probability that particle **2** ends up in an excited state as:

$$\begin{aligned} P_2^{e.s.}(b_2) =<\psi_{in}||S_2(b_2) - 1|^2|\psi_{in}> - \\ - |<\psi_{in}|S_2(b_2) - 1|\psi_{in}>|^2 \end{aligned} \tag{5.27}$$

Diffraction also implies that particle **1** survives the reaction:

$$P_1^s(b_1) = |S_1(b_1)|^2 \tag{5.28}$$

With all these considerations, the diffraction probability at a given impact parameter b_1 can be obtained by the multiplication of 5.27 and 5.28:

$$\begin{aligned} P^{diff}(b_1) =& < \psi_{in}||S_1(b_1)S_2(b_2) - S_1(b_1)|^2|\psi_{in} > - \\ -|& < \psi_{in}|S_1(b_1)S_2(b_2) - S_1(b_1)|\psi_{in} >|^2 = P_1^s \cdot P_2^{e.s.} \end{aligned} \tag{5.29}$$

By Integrating over all possible impact parameters b_1 and averaging over the magnetic quantum number of particle **2** we obtain the **diffraction cross-section** [Lvo01, Bar96, Hen96, Bar97, Bar00]:

$$\sigma^{diff} = \frac{10}{2j+1} \sum_m 2\pi \int_0^\infty b_1 db_1 \cdot P^{diff}(b_1) \tag{5.30}$$

In order to derive the formula of the core fragment longitudinal momentum distribution for the stripping reaction channel, we will start to write down the expressions of the wave function Fourier transforms:

$$\begin{aligned} \phi(z) &= \frac{1}{\sqrt{2\pi}} \int_{-\infty}^{\infty} dk_z \cdot e^{-ik_z z} \tilde{\phi}(k_z) \\ \tilde{\phi}(k_z) &= \frac{1}{\sqrt{2\pi}} \int_{-\infty}^{\infty} dz \cdot e^{ik_z z} \phi(z) \end{aligned} \tag{5.31}$$

The square norm of the wave function, according to the formulas 5.31, can be written as:

$$|\phi|^2 = \phi^* \phi = \int_{-\infty}^{\infty} dk_z \int_{-\infty}^{\infty} dk_z' \cdot \tilde{\phi}^*(k_z') \tilde{\phi}(k_z) \left(\frac{1}{2\pi} \int_{-\infty}^{\infty} dz \cdot e^{i(k_z' - k_z)z} \right) \tag{5.32}$$

The term in brackets can be recognized as the Dirac delta function. Using its properties we can rewrite expression 5.32 as:

$$|\phi|^2 = \int_{-\infty}^{\infty} dk_z \int_{-\infty}^{\infty} dk_z' \cdot \tilde{\phi}^*(k_z') \tilde{\phi}(k_z) \delta(k_z' - k_z) = \int_{-\infty}^{\infty} dk_z \cdot |\tilde{\phi}(k_z)|^2 \tag{5.33}$$

Replacing in equation 5.20 the new expression for the square norm of the wave function (equation 5.33), together with the explicit form of the wave function Fourier transform (equations 5.31), and differentiating both terms with respect

to k_z, we obtain the expression of the core fragment **longitudinal momentum distribution** for the **stripping** channel [Bar96, Hen96, Bar97, Bar00, Lvo01]:

$$\frac{d\sigma}{dk_z} = \frac{1}{2\pi}\frac{10}{2j+1}\sum_m 2\pi \int_0^\infty b_1 db_1 \int d^2\vec{r}_\perp \cdot f_2^{str} \cdot \left| \int_{-\infty}^{\infty} dz \cdot e^{ik_z z} \cdot \phi_{jm}(\vec{r}) \right|^2 \quad (5.34)$$

Once the theoretical background is set we can proceed to detail the process followed during calculations.

5.1.3 Theoretical calculations

Our aim is to evaluate (using the models described in the previous sections) the different observables obtained in our experiment. We will focus our attention on the calculus of exotic projectile one-neutron removal cross-sections and core fragment longitudinal momentum distributions.

In order to obtain one-neutron removal single particle cross-sections and core fragment momentum distributions we used the Glauber model (described in section 5.1.2). This model uses the nucleon-nucleon total cross-sections and real-to-imaginary ratios at $1000\ MeV$ tabulated in reference [Ray79] ($\sigma_{nn} = 47.2\ mb$, $\sigma_{np} = 39.2\ mb$, $\alpha_{nn} = -0.09$, $\alpha_{np} = -0.46$) as input parameters. The matter densities of target and core (in its different states), together with the wave function of the valence neutron, are also needed.

In the case of the core fragment longitudinal momentum distributions, the **black disk model** [Han96, Bar96, Bar97, Baz98, Sme98, Bar00, Lvo01] has also been used in order to perform an additional comparison. In this simple approximation all the particles (core fragments and valence neutrons) that "touch" the target are absorbed. This means that they will not be found scattered at forward angles with velocities close to the beam reference velocity. In order to define the "touch" condition we have used the ${}_eR_{rms}$ (experimental value of the root mean square radius obtained from [Oza01]) of the corresponding nucleus as effective radius (see table 5.1).

In addition, experimentally deduced spectroscopic factors have been calculated from the ratio between the experimental cross-sections and the corresponding theoretical single particle cross-sections calculated within the Glauber model. Spectroscopic factors are later used to weight among different contributions to form inclusive momentum distributions.

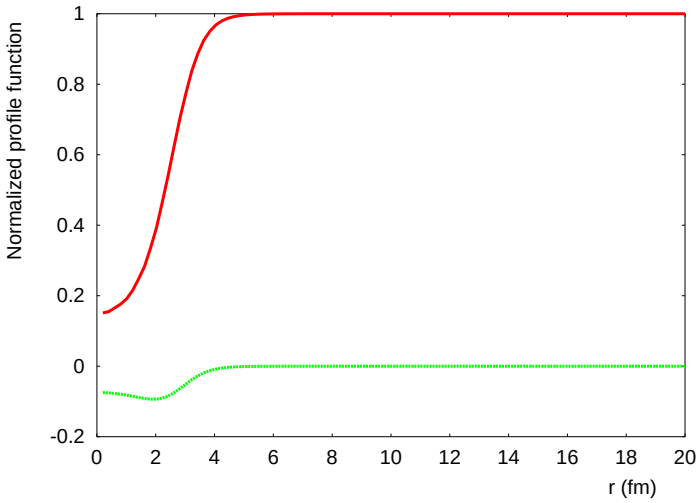

Figure 5.7: Real and imaginary parts of the neutron profile function used in the calculations, determined for the case of the carbon target. The real part (positive) gives the amount of wave function that survives the interaction at a given distance between neutron and target (r). The imaginary part (negative) is related to the scattering of the neutron. This contribution is maximum when the surfaces of both nuclei are in contact. Since the minimum value of the real part is found to be around 20%, we conclude that even in central collisions the neutron is not necessarily absorbed by the target.

Table 5.1: R_{rms} of the oxygen cores obtained theoretically ($_tR_{rms}$) compared to experimental data taken from [Oza01] ($_eR_{rms}$). Since the theoretical values are higher than the experimental ones, it is expected that the theoretical cross-sections will be smaller than the experimental ones. We could adjust theoretical and experimental radii by establishing a higher neutron binding in the HF calculation (with higher separation energies), but we preferred not to do any *ad hoc* manipulation. The corresponding data for the carbon target are also shown.

Nucleus	$_tR_{rms}$ (fm)	$_eR_{rms}$ (fm)
^{18}O	2.81	2.61 ± 0.08
^{19}O	2.84	2.68 ± 0.03
^{20}O	2.94	No data
^{21}O	3.01	2.71 ± 0.03
^{22}O	3.07	2.88 ± 0.06
^{12}C	2.47	2.31 ± 0.02

The neutron profile function obtained at the energy of the experiment, and

evaluated according to equation 5.13, is shown in figure 5.7. This profile function is made of a real and an imaginary part. The real part **of the profile function** is related to the absorption of the neutron by the target. The imaginary part **of the profile function** is related to the scattering of the neutron.

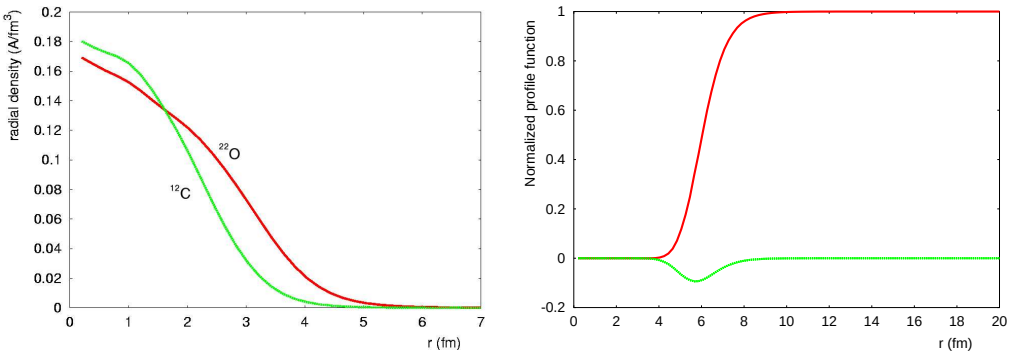

Figure 5.8: Left panel: ground state densities of the ^{12}C target and the ^{22}O core (more extended) obtained after QRPA calculations. Right panel: profile function of the ^{22}O core interacting with the carbon target. In this case there is a minimum impact parameter ($r \approx 4\ fm$) below which no core survives the reaction.

The nuclear density of the corresponding core (see figure 5.8) and the wave function of the valence neutron have been obtained, for odd nuclei, with the help of three chained programs [Len03a], providing:

1. the first program (HF) calculates the HF single particle wave functions of the core
2. the second program (QRPA) is able to obtain the different states of the core taking into account the residual pairing interaction
3. finally, the third one (QP-C) describes the coupling of the core to the valence neutron, again taking into account the residual pairing interaction

In the case of even-even nuclei, the third step (QP-C program) was not necessary.

The HF code was run by setting the core A and Z, and by adjusting its valence proton and neutron binding energies to the corresponding experimental separation energies taken from [Aud95] (see table 5.2). This code estimates the best values for the potential well (made of two Woods-Saxon for protons and two

Table 5.2: Separation energies [Aud95] of the last proton (S_p) and neutron (S_n) of the even-even oxygen isotopes, used in the HF calculation prior to QRPA.

Nucleus	S_p (MeV)	S_n (MeV)
^{18}O	15.942 ± 0.015	8.04439 ± 0.00078
^{20}O	19.353 ± 0.016	7.6080 ± 0.0032
^{22}O	23.24 ± 0.11	6.849 ± 0.058

Woods-Saxon for neutrons) and calculates the core single particle wave functions and energies. In the calculation, the single particle continuum was discretized by enclosing the system in a spherical cavity with radius equal to $40\ fm$, which was large enough for our purposes [Len03a].

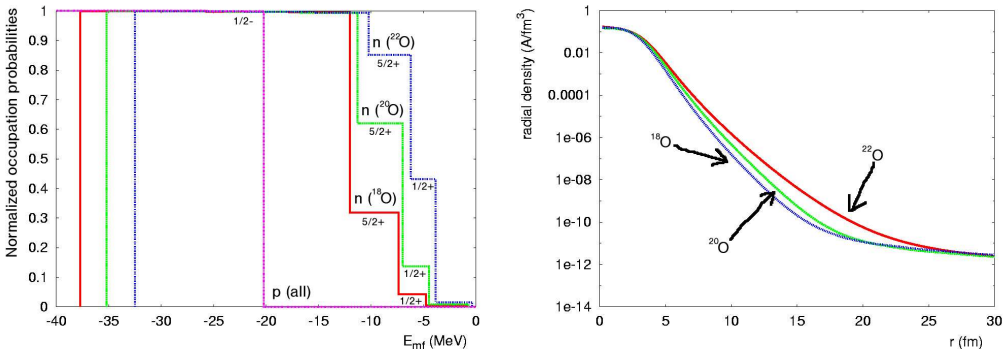

Figure 5.9: Left panel: proton and neutron occupation probabilities for ^{18,20,22}O in the QRPA ground state (only the surface levels in the respective cases are specified: $1p_{1/2} \equiv 1/2-$, $1d_{5/2} \equiv 5/2+$ and $2s_{1/2} \equiv 1/2+$). From a static mean-field calculation point of view, we would not expect to see any neutron in the $2s_{1/2}$ state for these nuclei, but pairing correlations are strong enough to "spread" the valence neutrons, and thus we observe a non negligible occupation probability for the $2s_{1/2}$ state, specially in the ^{22}O case. Right panel: this higher $2s_{1/2}$ component in ^{22}O causes a slower decrease in radial density, compared to the ^{18,20}O cases, observed when we go far from the center of the nucleus (see also figure 5.10).

The QRPA code needs the core A, Z and single particle wave functions as inputs and uses them to solve the QRPA equations with a pairing strength G for BCS given by the user. For protons, this pairing strength was always set to $G = \frac{23}{A}$ (value normally used in the bibliography, because it gives good results [Hey94, Len03a]), but for neutrons it was in the range $\frac{12}{A} - \frac{16}{A}$ [Len03a] (see

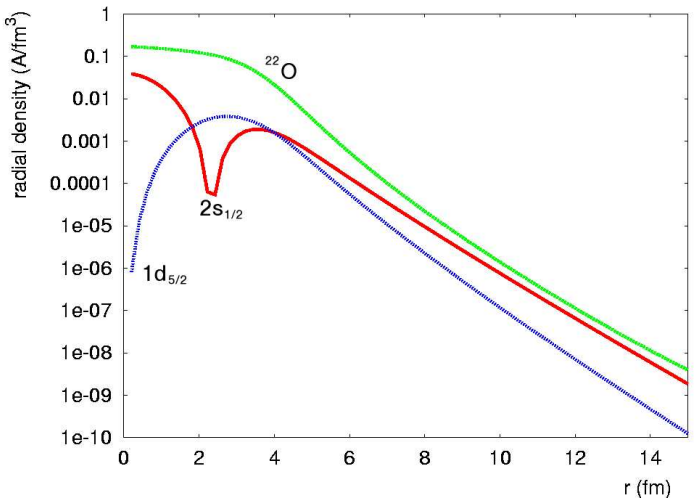

Figure 5.10: Radial density of ^{22}O compared to the radial density of one neutron in a $1d_{5/2}$ and in a $2s_{1/2}$ state. We can see that at long distances from the center, the $2s_{1/2}$ component becomes dominant and leads the behaviour of the ^{22}O radial density.

table 5.3). The neutron pairing force was adjusted in such a way that the first excited states of the even-even nucleus obtained with the QRPA code had the same spin, parity and excitation energy (I^π and E_{ex}) as the corresponding experimental ones (see table 5.4). The QRPA code outputs are: the core collective amplitudes in the definition of the quasiboson operators, the core electromagnetic-response amplitudes, and the core QRPA ground state configuration (occupation probabilities) in the single particle basis (see figures 5.9 and 5.10). For our purposes, we ran the code simultaneously for $I^\pi = 0^+$, 1^+, 2^+, 3^+, 4^+, 5^+, 6^+, 0^-, 1^-, 2^-, 3^-, 4^-, 5^- and 6^- [Len03a]. The maximum excitation energy was set to $30\ MeV$ [Len03a] ($40\ MeV$ in the case of ^{22}O).

QP-C code inputs are:

- A and Z of the **odd** nucleus
- single particle wave functions of the **core** (from HF)
- collective amplitudes conforming excitation operators (for all the I^π's to be considered)
- core ground state configuration (from QRPA)
- strength of the pairing interaction of protons and neutrons (from QRPA)

Table 5.3: Strength of the pairing correlations for protons and neutrons.

Nucleus	G_p (MeV)	G_n (MeV)
^{19}O	1.2	0.63
^{20}O	1.1	0.65
^{21}O	1.1	0.62
^{22}O	1.0	0.73
^{23}O	1.0	0.70

Table 5.4: Comparison between the first exited levels ($_tE_{ex}$) obtained with QRPA for the even-even oxygen isotopes and the experimental ones ($_eE_{ex}$) taken from [Fir96, Sau00a]. In the case of the ^{22}O, the "experimental" I^π assignment is from [Bro03]. We can see that the 2^+ state is already low and goes down in energy from ^{18}O to ^{20}O; a macroscopic explanation [Len03b] for this can be that, when we approach the driplines, nuclei present a lower surface tension and the restoring forces against "external" perturbations are reduced, which increases quadrupole polarizability (an indication is a "low" 2^+ first excited state). ^{22}O does not seem to follow the general trend.

Nucleus	$_tE_{ex}$ (MeV)	$_tI^\pi$	$_eE_{ex}$ (MeV)	$_eI^\pi$
^{18}O	2.0	2^+	2.0	2^+
^{18}O	2.7	0^+		
^{18}O	3.2	4^+	3.6	4^+
^{20}O	1.7	2^+	1.6	2^+
^{20}O	3.1	0^+		
^{20}O	3.4	4^+	3.6	4^+
^{22}O	3.1	2^+	3.1	(2^+)
^{22}O	3.7	0^+		
^{22}O	4.1	3^+	4.4	(3^+)

- core I^π's and E_{ex}'s to be considered
- single particle states to be coupled to core states (in our case: $1s^{1/2}$, $1p^{3/2}$, $1p^{1/2}$, $1d^{5/2}$, $2s^{1/2}$ and $1d^{3/2}$)
- total spin and parity of the odd nucleus states for which the calculation is done (in our case: the ground state J^π)

The QP-C code was used to calculate the 1- and 3-QP amplitudes present in the definition of the quasifermion operators, strength functions (see figure 5.11),

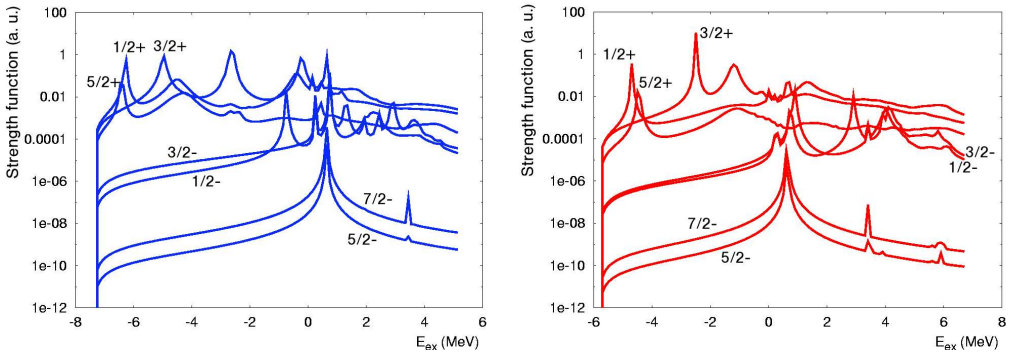

Figure 5.11: Strength functions for ^{21}O (left) and ^{23}O (right), as obtained from QP-C calculations. The strength functions present peaks at the excited states of the corresponding nucleus, while the first peak corresponds to the ground state. Therefore, the ^{21}O and ^{23}O calculated ground states have J^π equal to $\frac{5}{2}^+$ and $\frac{1}{2}^+$, respectively.

and single particle wave functions of the nucleon added to the core.

With all these ingredients we can proceed to compare the experimental data to theoretical predictions. These theoretical predictions come from QRPA and QP-C nuclear structure approaches (see section 5.1.1), together with the Glauber model described in section 5.1.2.

5.2 Comparison between experimental data and theory for projectiles $^{19-23}$O

In the following sections we will present the comparison between the experimental data and the results obtained with the model calculations done for oxygen isotopes. We want now to define two concepts that will be extensively used:

- **Exclusive observable:** obtained for a particular reaction channel (core ground state, core first excited state, ...). When applied to experimental measurements, it signifies "using the coincidences"

- **Inclusive observable:** refers to all the possible channels that can be considered. When applied to experimental measurements, its is equivalent to say "without using coincidences"

5.2.1 Cross-sections

In this section we will discuss the theoretical calculations done for the one-neutron removal cross-sections on a carbon target.

One-neutron removal cross-sections are originated by three principal processes: stripping of the neutron, diffractive breakup and Coulomb breakup (see section 5.1.2). At the energies that we had in the experiment ($\sim 1\ AGeV$), diffractive breakup is around one order of magnitude smaller than neutron stripping. Coulomb breakup contribution depends on the atomic number of the target (Z_t), and it is expected to be negligible compared to the nuclear breakup contribution in the case of a carbon target. Therefore, we have not taken it into account in the following calculations, done in the context of Glauber + QRPA + QP-C.

Table 5.5: Theoretical QP-C spectroscopic factors (${}_tC^2S$) and one-neutron removal cross-sections (${}_t\sigma_{-1n}$) are compared to experimental one-neutron removal cross-sections (${}_e\sigma_{-1n}$) and spectroscopic factors (${}_eC^2S$) deduced from the ratio between experimental one-neutron removal cross-sections and calculated single particle cross-sections (${}_t\sigma_{sp}$). $\sum$ signifies "total contribution", and "-" indicates that there is no contribution to the particular channel.

Proj.	J^π	E_c (MeV)	I_c^π	nlj	${}_t\sigma_{sp}$ (mb)	${}_tC^2S$	${}_t\sigma_{-1n}$ (mb)	${}_eC^2S$	${}_e\sigma_{-1n}$ (mb)
^{19}O	5/2+	0	0+	$1d_{5/2}$	21.	3.56	76	2.67±.47	56.1±9.8
^{20}O	0+	0	5/2+	$1d_{5/2}$	19.	1.67	32	2.93±.46	55.6±8.8
^{21}O	(5/2+)	0	0+	$1d_{5/2}$	19.	2.06	40	2.00±.63	38.±12.
		1.6	2+	$1d_{5/2}$	19.	0.06	1	-	-
		1.6	2+	$2s_{1/2}$	28.	0.14	4	-	-
		1.6	2+	$1d_{3/2}$	29.	0.03	1	-	-
		1.6	2+	$\sum$	-	-	6	-	6.8±7.2
		3.6	4+	$\sum$	-	-	-	-	27.±12.
^{22}O	0+	0	5/2+	$1d_{5/2}$	17.	3.35	58	4.11±.55	69.8±9.4
^{23}O	(1/2+)	0	0+	$2s_{1/2}$	28.	1.04	28	1.79±.64	50.±18.
		3.1	2+	$1d_{5/2}$	18.	0.01	0	-	-
		3.1	2+	$1d_{3/2}$	29.	0.04	1	-	-
		3.1	2+	$\sum$	-	-	1	-	10.5±6.2
		4.4	3+	$\sum$	-	-	-	-	14.0±7.6
		5.7	(1-,0-)	$\sum$	-	-	-	-	10.5±6.2

In table 5.5 we present the comparison between experimental and theoretical one-neutron removal cross-sections and spectroscopic factors. Each "experimen-

tal" spectroscopic factor has been obtained from the *ratio* between the corresponding experimental one-neutron removal cross-section and the theoretical single particle cross-section obtained for the core spin and parity related to the particular channel. The determination of the experimental spectroscopic factor was done when the spin and parity assignment was clear.

With respect to the experimental data, the coincidence method allows us to separate the inclusive cross-sections into contributions of the *ground* and *excited states*. Further partition of the excited states contribution was possible due to the availability of decay branching ratios, which were estimated using the GEANT simulation. From the decay branching ratios and the level scheme it is possible to deduce the occupation probabilities in the case of the different excited states. This makes it possible to obtain the cross-section for each individual reaction channel in which the core was produced in a specific excited state.

From the inspection of table 5.5, it can be seen a general good agreement between theoretical predictions and the experimental data. It is also interesting to mention the agreement, for the ^{22}O ground state channel, between our theoretical model cross-section ($28\ mb$), and the theoretical cross-section calculated at [Sau03] for an energy of $900\ AMeV$ ($27.2\ mb$).

^{23}O presents a spectroscopic factor **very close to unity** for the $\frac{1}{2}^+$ ground state, indicating that its nuclear structure can be well described using the single particle model, as was done in [Bro03]. This fact is related to the supposed N=16 shell closure at ^{24}O: ^{23}O would present, from this point of view, an almost closed shell configuration with just one valence neutron hole. A situation which is known to be well described by the single particle model.

5.2.2 Momentum distributions of core fragments

Core fragment momentum distributions present two types of components: longitudinal and transversal. Transversal components are much more affected by the reaction than the longitudinal component. The origin of this is in the diffractive part of the cross-section: while stripping considers as final state the part of the wave function that did not react, diffraction takes into account the scattered wave function, which can be very different from the initial one, specially when it is emitted in the transversal direction. Therefore, we will only study the longitudinal component, which carries more information about the structure of the exotic projectile. As we have already done for the cross-sections, we restrict ourselves to one-neutron removal on carbon target.

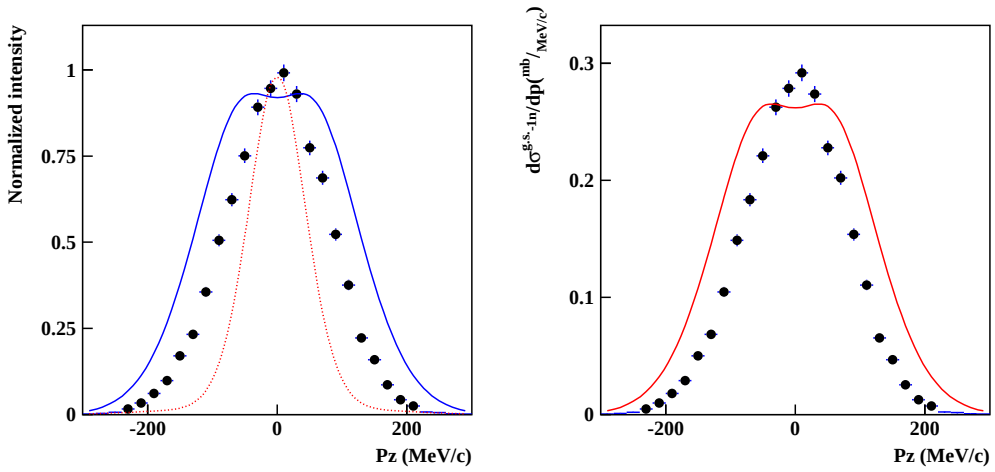

Figure 5.12: One-neutron removal on a carbon target for the ^{19}O exotic projectile. Left panel: comparison between the theoretical (solid curve) and the experimental (points) **profile** of the inclusive core longitudinal momentum distribution. The weigths used in the superposition of the different pure channels are given by the corresponding experimental spectroscopic factors. We have assumed a $1d_{5/2}$ wave for the ground state. The dotted curve corresponds to a pure $2s_{1/2}$ wave and has been plotted for comparison purposes. Right panel: comparison between the theoretical (curve) and the experimental (points) exclusive core longitudinal momentum distribution for the ^{18}O core ground state channel. Note that in this case both the **profile** and the **cross-section** are compared. The weights used in the superposition of the different pure channels are given by the corresponding theoretical spectroscopic factors.

First we consider the inclusive core fragment momentum distributions, where the contribution from ground and excited states is mixed and the resulting distribution profile is a weighted superposition of the different channels. The weight of each individual channel is given by the corresponding spectroscopic factor. They have been deduced both experimentally and theoretically in this work.

The experimental spectroscopic factors are obtained from the experimental exclusive one-neutron removal cross-sections and the corresponding theoretical single particle cross sections. Due to the limited energy resolution of our γ-ray detectors array, the coincidence method was able to separate the inclusive core longitudinal momentum distribution only into two channels: the *core ground state channel*, and the *core excited states channel*. If the removed neutron was *mainly* in a specific level inside the exotic projectile, we could deduce it, by assum-

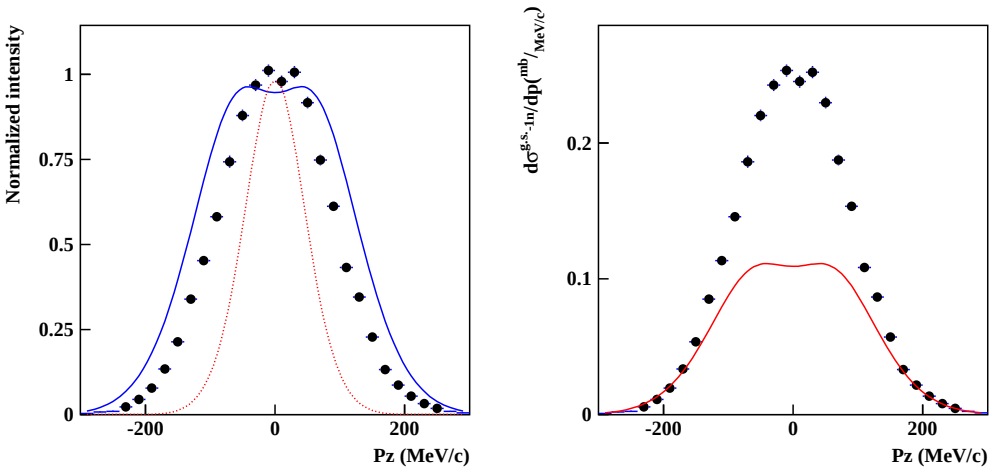

Figure 5.13: One-neutron removal on a carbon target for the ^{20}O exotic projectile. Left panel: comparison between the theoretical (solid curve) and the experimental (points) **profile** of the inclusive core longitudinal momentum distribution. The weigths used in the superposition of the different pure channels are given by the corresponding experimental spectroscopic factors. We have assumed a $1d_{5/2}$ wave for the ground states. The dotted curve corresponds to a pure $2s_{1/2}$ wave and has been plotted for comparison purposes. Right panel: comparison between the theoretical (curve) and the experimental (points) exclusive core longitudinal momentum distribution for the ^{19}O core ground state channel. Note that in this case both the **profile** and the **cross-section** are compared. The weights used in the superposition of the different pure channels are given by the corresponding theoretical spectroscopic factors.

ing a predominant wave ($2s_{1/2}$, $1d_{5/2}$, ...) for that channel. This predominant wave is selected by direct observation of the exclusive experimental core fragment momentum distribution profiles presented in section 4.4.

The theoretical spectroscopic factors, together with the level occupied by the removed neutron when it was inside the exotic projectile, are directly provided by the theoretical calculations.

Once we have, for the different channels, both the spectroscopic factor and the level occupied by the removed neutron, it is possible to reconstruct the inclusive core fragment longitudinal momentum distribution by using, in addition, the theoretical exclusive momentum distribution profile which corresponds to the state of the neutron when it was inside the exotic projectile.

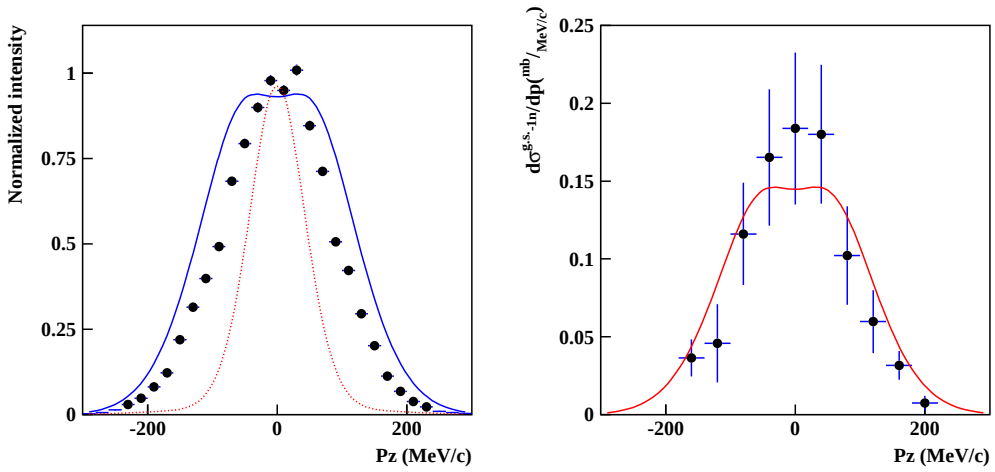

Figure 5.14: One-neutron removal on a carbon target for the ^{21}O exotic projectile. Left panel: comparison between the theoretical (solid curve) and the experimental (points) **profile** of the inclusive core longitudinal momentum distribution. The weigths used in the superposition of the different pure channels are given by the corresponding experimental spectroscopic factors. We have assumed $1d_{5/2}$ waves for both ground and excited states. The dotted curve corresponds to a pure $2s_{1/2}$ wave and has been plotted for comparison purposes. Right panel: comparison between the theoretical (curve) and the experimental (points) exclusive core longitudinal momentum distribution for the ^{20}O core ground state channel. Note that in this case both the **profile** and the **cross-section** are compared. The weights used in the superposition of the different pure channels are given by the corresponding theoretical spectroscopic factors.

The comparison between the experimental inclusive core fragment longitudinal momentum distribution profiles and the approach using experimental spectroscopic factors is shown at the left side of figures 5.12, 5.13, 5.14, 5.15 and 5.16, for different oxygen projectiles (^{19,20,21,22,23}O). The right side of those figures depicts the comparison between the exclusive core fragment longitudinal momentum distribution and the approach using theoretical spectroscopic factors. We want to note that, in this last case, we used the inclusive core fragment momentum distribution instead of the exclusive core fragment momentum distribution for the core ground state channel for those fragments without peaks in their corresponding γ-ray spectrum, because we assume that those core fragments emerged from the reaction mainly in the ground state.

Examining the left side of figures 5.12, 5.13, 5.14 and 5.15, it appears that

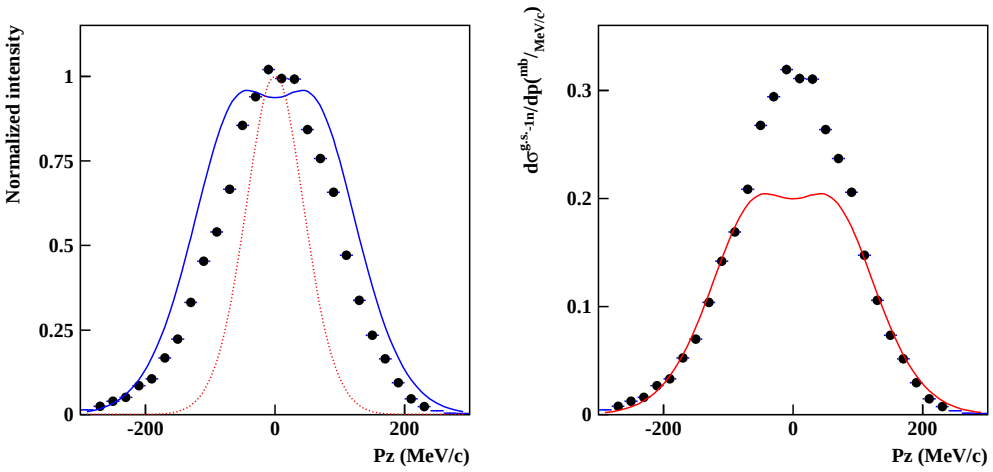

Figure 5.15: One-neutron removal on a carbon target for the ^{22}O exotic projectile. Left panel: comparison between the theoretical (solid curve) and the experimental (points) **profile** of the inclusive core longitudinal momentum distribution. The weigths used in the superposition of the different pure channels are given by the corresponding experimental spectroscopic factors. We have assumed a $1d_{5/2}$ wave for the ground state. The dotted curve corresponds to a pure $2s_{1/2}$ wave and has been plotted for comparison purposes. Right panel: comparison between the theoretical (curve) and the experimental (points) exclusive core longitudinal momentum distribution for the ^{21}O core ground state channel. Note that in this case both the **profile** and the **cross-section** are compared. The weights used in the superposition of the different pure channels are given by the corresponding theoretical spectroscopic factors.

^{18,19,20,21}O core fragments momentum distributions present a predominant d wave component, although a small amount of s wave is needed for better aggreement.

In contrast, ^{22}O core fragment (figure 5.16) exhibits a very different profile, characterised by the clear influence of a s wave. For this nuclide, our experimental assumptions have been: s wave for the ground state and d wave for the excited states. In this way, both contributions are mixed in the figure on the left according to the experimental spectroscopic factors for the core ground and excited states channels obtained using the coincidence method and shown in table 5.5.

The right sides of figures 5.12, 5.13, 5.14 and 5.15 show the theoretical exclusive core fragment momentum distribution ability to reproduce at the same time both the experimental core fragment momentum distribution profile and the

cross-section. From the inspection of these results, it appears that even-odd oxygen isotopes (projectiles) present core fragment momentum distributions which are better reproduced by the theoretical calculations.

Two reasons for the discrepancies observed in those figures are:

- We have already seen that the R_{rms} of the oxygen cores obtained using our theoretical approach are larger than the experimental ones obtained from [Oza01] (see table 5.1), and thus was expected that the theoretical cross-sections were smaller than the experimental ones
- We have followed a semiclassical approach (*eikonal* approximation) to describe the reaction mechanism. It can be anticipated that a more quantizated analysis (for example, DWBA) will provide better results

Let us now turn our attention to the exclusive core fragment longitudinal momentum distribution **profiles**, for the ^{21,23}O exotic projectiles, where the coincidence method could be applied. We have already seen that both nuclides present very different inclusive core fragment longitudinal momentum distributions. We will discuss the reason for this different behaviour.

We show in figure 5.17, ^{20}O core fragment longitudinal momentum distributions after one-neutron removal from ^{21}O, for the ground and excited states channels. Although histograms present quite large error bars, the d wave seems to be the most plausible main component in both channels. In addition, we have seen that the QP-C model predicts a $\frac{5}{2}^+$ ground state for the ^{21}O. This means that if we want to couple a neutron to the 0^+ ground state of ^{20}O to form ^{21}O in its ground state, the neutron must be in a $d_{5/2}$ level. Therefore, we must choose a $1d_{5/2}$ wave for the *ground state* channel. The *excited states* channel presents a profile which is very similar to the *ground state* channel profile, thus we have also chosen a $1d_{5/2}$ wave for it.

The longitudinal momentum distributions for ground and excited states of ^{22}O core fragment after one-neutron removal from ^{23}O, are plotted in figure 5.18. The main contribution to the excited states seems to be, within error bars, a d wave (we selected it to be a $1d_{5/2}$ wave). In the case of the ground state it is **clear** that a s wave must be used. This fact is corroborated by the QP-C prediction for the ground state: $\frac{1}{2}^+$, and makes the difference between ^{20}O and ^{22}O inclusive longitudinal momentum distributions.

To end this chapter, I would like to comment that there exists a certain controversy with respect to ^{23}O ground state nuclear structure: E. Sauvan *et*

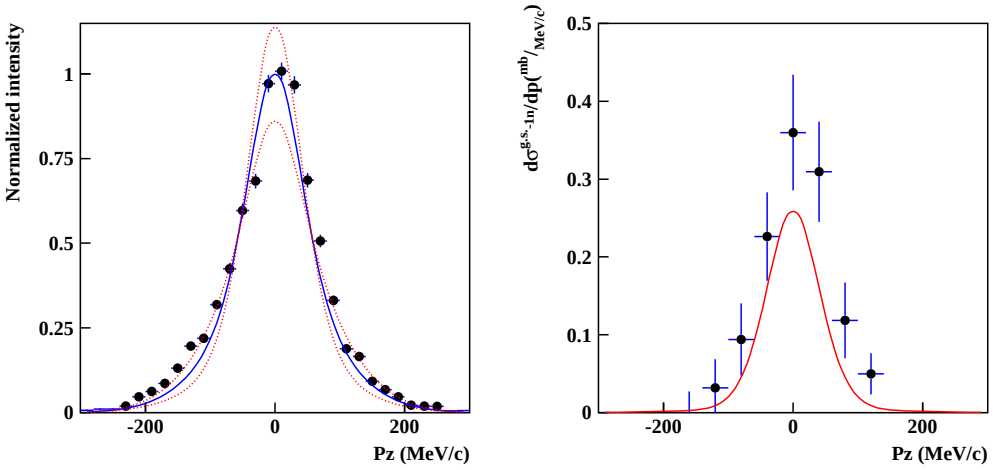

Figure 5.16: One-neutron removal on a carbon target for the ^{23}O exotic projectile. Left panel: comparison between the theoretical (solid curve) and the experimental (points) **profile** of the inclusive core longitudinal momentum distribution. The weigths used in the superposition of the different pure channels are given by the corresponding experimental spectroscopic factors. We have assumed a $2s_{1/2}$ wave for the ground state and a $1d_{5/2}$ wave for the excited states. The dotted curves correspond to the error interval given by the errors in the weights determined by the coincidence method. Right panel: comparison between the theoretical (curve) and the experimental (points) exclusive core longitudinal momentum distribution for the ^{22}O core ground state channel. Note that in this case both the **profile** and the **cross-section** are compared. The weights used in the superposition of the different pure channels are given by the corresponding theoretical spectroscopic factors.

al. [Sau00b] observed a narrow inclusive longitudinal momentum distribution of ^{22}O after the breakup of ^{23}O, and assigned $\frac{1}{2}^+$ to the ^{23}O ground state. On the other hand, R. Kanungo *et al.* [Kan02] assigned $\frac{5}{2}^+$ to the ^{23}O ground state, based in the inclusive longitudinal momentum distribution of ^{21}O after two-neutron removal from ^{23}O. These two different (and thus conflictive) assignments called the attention of B. A. Brown *et al.* [Bro02], who in a recent work indicated that a shell model with **USD** interaction predicted a $\frac{1}{2}^+$ ^{23}O ground state. In that work, B. A. Brown *et al.* also obtained a good agreement to the experimental one-neutron removal cross-section of ^{23}O, measured by R. Kanungo *et al.* [Kan02], by using a single particle $(1d_{5/2})^6(2s_{1/2})^1$ configuration (which implies again a $\frac{1}{2}^+$ ground state). Notwithstanding, R. Kanungo *et al.* [Kan03] have answered that the interaction cross-section of ^{23}O and the longitudinal momentum distribution of ^{22}O after one-neutron removal from ^{23}O cannot be consistently explained

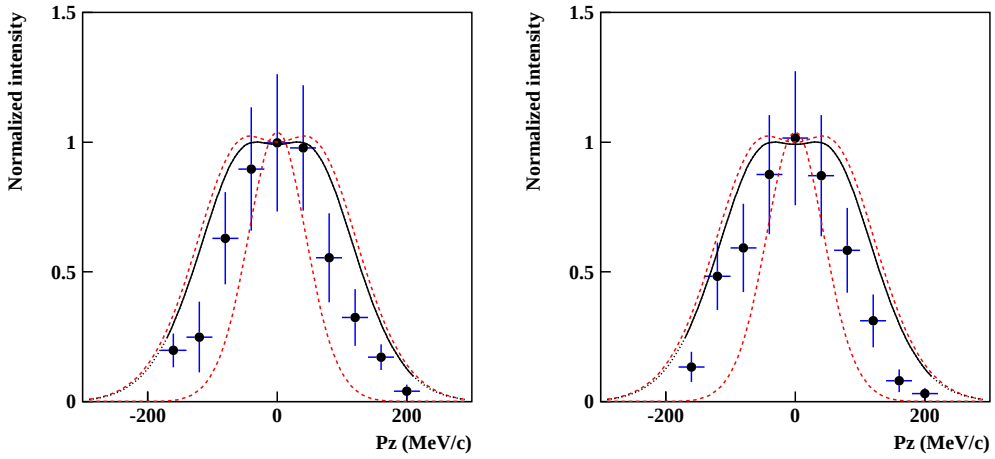

Figure 5.17: Exclusive longitudinal momentum distribution of ^{20}O core fragment produced from ^{21}O, for the core ground state (left) and excited states (right) channels. The dashed curves are the black disc model predictions for $2s_{1/2}$ (narrow) and $1d_{5/2}$ (wide), and are shown for comparison purposes. The solid curve corresponds to the Glauber + QRPA + QP-C prediction for $1d_{5/2}$.

within any present model. In fact, they indicated that in another work by B. A. Brown *et al.* [Bro01] the interaction cross-section was not well reproduced by the shell model used there. Kanungo *et al.* [Kan03] also commented that there exists an inconsistency between the spectroscopic factors calculated using shell model (that can be larger than one, in case of orbitals with more than one neutron) and the present reaction model, which treats the projectile nucleus as a core + one neutron. When treating the knockout of neutrons from orbitals with more than one neutron, some kind of core + multineutron treatment should be used if we want to use shell model spectroscopic factors, and this model is missing.

In this context it is desirable to measure as pure as possible observables, since they result in more transparent interpretations. One important tool in this sense is the coincidence method described and used in this work. This method, applied to core fragment momentum distributions, allows us to obtain a very pure observable: the longitudinal momentum distribution of the residual core fragment produced in the ground and excited states.

An example of the power of this method is the good agreement existing between the profile of the experimental longitudinal momentum distribution of

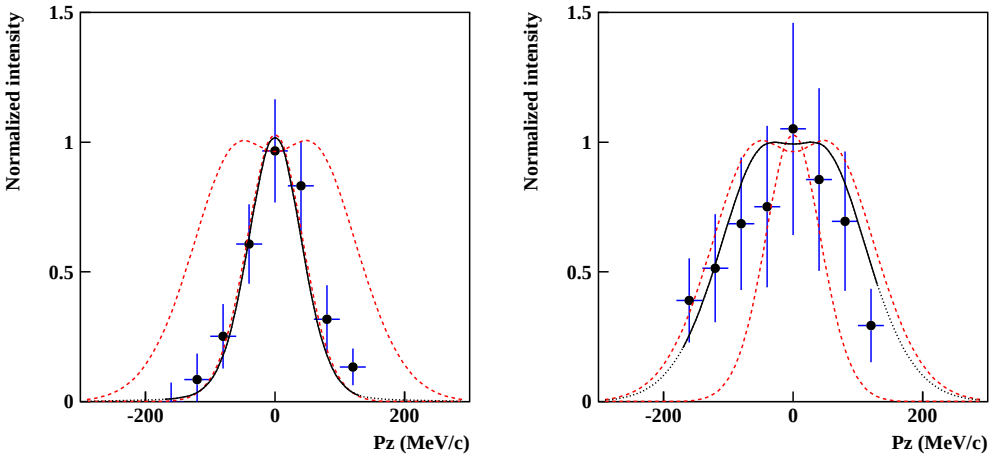

Figure 5.18: Left panel: exclusive longitudinal momentum distribution of ^{22}O core fragment produced from ^{23}O, for the ground state channel. The dashed curves are the black disc model predictions for $2s_{1/2}$ (narrow) and $1d_{5/2}$ (wide), and are shown for comparison purposes. The solid curve corresponds to the Glauber + QRPA + QP-C prediction for $2s_{1/2}$. The agreement is very good in this case. Right panel: exclusive longitudinal momentum distribution of ^{22}O core fragment produced from ^{23}O, for the excited states channel. The dashed curves are the black disc model predictions for $2s_{1/2}$ (narrow) and $1d_{5/2}$ (wide), and are shown for comparison purposes. The solid curve corresponds to the Glauber + QRPA + QP-C prediction for $1d_{5/2}$.

^{22}O produced in the ground state after one-neutron removal from ^{23}O and the theoretical pure $2s_{1/2}$ wave longitudinal momentum distribution obtained in two different cases: realistic profile functions and black disk model (see figure 5.18 -left-). This agreement allows us to estate the important result that the ^{23}O ground state is definitively $\frac{1}{2}^+$.

Chapter 6

Summary and outlook

This work was dedicated to the experimental investigation of the structure of light neutron-rich isotopes in the sd shell, using breakup reactions, with such nuclei being close to the neutron dripline and having neutron numbers at approximately N=16.

Neutron-rich oxygen isotopes near the neutron dripline present very exciting issues for nuclear structure studies. It has been recently shown that ^{22}O with a first excited 2^+ level at $3.17\ MeV$ and ^{24}O with no excited state below $4\ MeV$ appear to be doubly magic nuclei. This finding indicates a persistence of the proton-magic shell at Z=8 and (sub-)shell closures at N=14 and N=16. At the same time, the non-observation of ^{28}O with 20 neutrons is indicative of a weakening of the N=20 shell. Therefore, the last bound oxygen isotope is ^{24}O.

^{23}O is a key nucleus in understanding the structure of light neutron-rich nuclei because it is very close to the neutron dripline, has 15 neutrons (close to the new N=16 magic number) and 8 protons (magic number). In addition, its measured interaction cross-section indicates that this nucleus could be a neutron halo candidate. Moreover, ^{23}O has generated renewed interest as interpretations of different inclusive experimental results indicate different spin and parity assignments for its ground state.

The present experiment was carried out with the FRS facility at GSI. A ^{40}Ar primary beam, at approximately $1\ AGeV$, was used to produce a secondary beam of light neutron-rich isotopes by projectile fragmentation on a beryllium target. Residual core fragments of these secondary projectiles in coincidence with de-excitation γ-rays emitted by those core fragments were measured, using both carbon and lead targets in an event-by-event basis. For the first time, in-beam γ-ray spectroscopy has been used at relativistic energies. The quality of the re-

sults obtained in this thesis clearly validates this technique.

The experimental observables measured in this work are the following:

- one-neutron removal cross-sections and momentum distributions (longitudinal and transversal components) after breakup reaction on a carbon target, for the following exotic projectiles: ^{17,18,19,20}N, ^{19,20,21,22,23}O, ^{22,23,24,25,26}F
- one-neutron removal cross-sections and momentum distributions (longitudinal and transversal components), after breakup reaction on a lead target, for the following exotic projectiles: ^{19,20}N, ^{22,23}O, ^{25,26}F
- two-neutron removal cross-sections and momentum distributions (longitudinal and transversal components), after breakup reaction on a carbon target, for the following exotic projectiles: ^{21}N, ^{24}O, ^{27}F
- γ-ray spectra emitted by residual core fragments produced in the previously mentioned breakup reactions. In several cases which presented good statistics, the measured momentum distributions were gated according to the final states of the residual core fragments. These exclusive distributions were useful to disentangle the angular orbital momentum associated with the valence neutron, determining the spin and parity of the investigated exotic projectile. The selection of final states of the core fragment allowed the evaluation of exclusive one-neutron removal cross-sections. These observables are very sensitive to the structure properties of the exotic nuclei and the reaction mechanism used to describe the reaction

Analysis of these observables leads to the following conclusions:

The measured one-neutron removal cross-sections show a clear odd-even effect while they increase with the mass number A, inside an isotopic chain. These findings have been compared to similar measurements at approximately $60\ AMeV$, showing good overall agreement. Cross-sections measured in lead are higher than those obtained with carbon, a fact that was expected due to the increased Coulomb interaction.

Momentum distributions of residual core fragments in breakup reactions were used to investigate evolution of the shell filling with isospin. Our experiments have proven, once again, an overall agreement with the core fragment momentum distribution profiles measured at lower energies. The results that we obtained using both carbon and lead targets present very similar profiles for core fragment longitudinal momentum distributions. Therefore, we can confirm that the momentum distribution of residual core fragments produced in the breakup reaction

is independent of the energy of the projectile, along with the nature of the target.

The systematics of the core fragment longitudinal momentum distribution Full Widths at Half Maximum (FWHM) obtained in this work shows a significant change in the general trend when we reach N=14. This change coincides with the filling of the $2s_{1/2}$ level in the single particle scheme. A clear even-odd effect was also observed. This effect is understood when one considers that odd nuclei have a valence neutron that is less bound, and thus their corresponding core fragment longitudinal momentum distributions are narrower.

The coincident measurement of fragments after nucleon removal with the γ de-excitation of these fragments was performed to separate ground state from excited state contributions. The coincidence method was applied to those nuclides which presented peaks at the γ-ray spectra. The relative amount of excited states compared to the ground state contribution indicates to a certain extent the proportion of the core polarization, provided that there is no fragment excitation during the reaction.

Finally, the interpretation of results using model calculations yields the following conclusions:

Valence neutron removal cross-sections have been used to identify possible halo candidates, in particular ^{23}O. ^{23}O does not present a very large one-neutron removal cross-section for both carbon and lead targets, compared to its neighbours in the isotopic chain. The increment observed for the one-neutron removal cross-sections of this nuclide can be explained by consideration of the fact that this is an odd nucleus whose valence neutron should be in the $2s_{1/2}$ level. From a single particle point of view, the core should be very stable since the $1p_{1/2}$ level for protons and $1d_{5/2}$ for neutrons are filled. These facts, together with the relatively high value of its neutron separation energy ($2.74 \pm 0.12\ MeV$), appear to indicate that this nucleus is not a halo candidate.

^{26}F presents a smaller one-neutron removal cross-section when compared to its neighbour ^{25}F. This behaviour was not expected, since the single neutron should be in the $1d_{3/2}$ level (from a single particle point of view). It also presents a narrow momentum distribution (FWHM). These two facts could indicate that the core of this nuclide is quite polarized and its valence neutron has a strong probability of being in the $2s_{1/2}$ level.

Two-neutron removal is not a process as direct as one-neutron removal. This means that the conclusions obtained for this channel must be carefully taken into

account.

The two-neutron removal channel studied for ^{24}O shows an apparently "normal" cross-section and momentum distribution (FWHM). These results appear to confirm that ^{24}O is not a two-neutron halo. On the other hand, ^{27}F has a large two-neutron removal cross-section and narrow momentum distribution (FWHM). These two observations could indicate the presence of a halo in this nucleus. It would be interesting to perform a dedicated experiment focusing on ^{26,27}F.

Clear peaks were only observed in γ-ray spectra of residual core fragments after the breakup of exotic projectiles with an odd number of neutrons (^{18,20}N, ^{21,23}O, ^{22}F). This could be an indication of core polarization of these nuclides. The presence of peaks in the spectrum also appears independent of the reaction, as all three γ-ray spectra of ^{18}N (one-neutron removal on carbon and lead, and two-neutron removal on carbon) present the same peak.

The controversial results of the spin and parity assignment for ^{23}O ground state required confirmation based on an *exclusive* knockout experiment similar to that which is presented in this work. The experimental momentum distribution for the one-neutron removal channel leaving the ^{22}O core in its ground state, obtained in this work, has been compared to Eikonal calculations for the knockout process. The distribution corresponding to a $2s_{1/2}$ neutron coupled to the ^{22}O (0^+) core clearly agreed more with the data. We can thus conclude without any doubt that the ground-state spin of ^{23}O is $I^\pi = \frac{1}{2}^+$.

We have not observed γ rays in the spectra of ^{19,21}O. This result is in good agreement with shell-model predictions obtained with the OXBASH code for ^{20,22}O, which indicate that these cores are mainly in the ground state. Therefore, it can be expected that ^{20,22}O would present a dominant single particle behaviour.

The experimental data has also been compared to more sophisticated model calculations (Glauber + QRPA + QP-C), obtaining a good concordance with theoretical predictions for spectroscopic factors of core fragments in their ground state. A reasonable agreement has also been found between our experimental results and theoretical predictions (both single particle and quasiparticle-core) for both the ground state of ^{21}O ($\frac{5}{2}^+$), and the ground state of ^{23}O ($\frac{1}{2}^+$). Calculations with QuasiParticle-Core coupling (QP-C) also predict very close $2s_{1/2}$ and $1d_{5/2}$ levels for these nuclides.

However, we have found some discrepancies when comparing experimen-

tally deduced spectroscopic factors to those obtained using model calculations (Glauber + QRPA + QP-C) for core fragments in excited states. This can be due to the semiclassical approach (eikonal approximation) used for the reaction mechanism. It can be anticipated that a more quantizated analysis (for example, DWBA) will provide better results.

The volume of results obtained in this experiment provide a better understanding of the nuclear structure of light exotic nuclei close to the neutron dripline. These findings provide systematic information with relation to the valence neutron(s) removal cross-sections and momentum distributions of neutron-rich isotopes in the sd shell. The use of the coincidence technique with γ-rays provides access to exclusive longitudinal momentum distributions on individual final energy states of the residual core fragment in breakup reactions. These exclusive measurements offer information relating to the angular orbital momentum associated with the valence neutron. In addition, experimental access to spectroscopic factors is provided. This could prove very useful in the near future to test the predictive power of model calculations. Experimental spectroscopic factors obtained in this experiment constitute a **unique** data set, because they are for the moment the only spectroscopic factors obtained at relativistic energies and for relatively heavy nuclei.

This work creates new perspectives in the investigation of light exotic nuclei using breakup reactions. From an experimental point of view, the use of high granularity and better energy resolution γ-ray detectors is vital to reduce the experimental incertitude. Such a progression would equip us to investigate heavier systems.

The contribution of the author to this work includes the collaboration in the detector setup and calibrations, particularly the NaI scintillator array, participation in the data taking and complete data analysis and interpretation.

Appendix A

Theoretical description of the nuclear structure

A.1 Second quantization

Second quantization refers to the "occupation number representation". We will state some basic concepts:

- **Creation and destruction operators:** a^+ and a

- **Vacuum state:**

It has no particles, and it is written as: $|>$. The vacuum fullfils the property $a|>=0$, for every a.

- We can **create, from the vacuum, one particle** in a quantum state p:

$$a_p^+|>=|p> \tag{A.1}$$

- When we have more than one particle, we define the **Number Operator** as:

$$\hat{n} \equiv \sum_p a_p^+ a_p \tag{A.2}$$

- Attending to the behaviour when we have more than one particle we can separate them in **two groups**:

1. **Fermions:**

We can add more particles: $a_q^+|p>=|p,q>$, but no more than one in the same state: $a_p^+|p>=0$. This, and the definition of the Number Operator, defines the following anticonmutation relations between the fermion operators:

$$\{a_p, a_q\} \equiv a_p a_q + a_q a_p = 0 \qquad \{a_p^+, a_q^+\} = 0 \qquad \{a_p, a_q^+\} = \delta_{p,q} \quad \text{(A.3)}$$

2. **Bosons:**

They are different from the fermions because any number of bosons can be in the same state. This originates the existence of conmutation relations between the boson operators:

$$[b_p, b_q] \equiv b_p b_q - b_q b_p = 0 \qquad [b_p^+, b_q^+] = 0 \qquad [b_p, b_q^+] = \delta_{p,q} \quad \text{(A.4)}$$

The conmutation relations and the definition of the Number Operator establishes the following expressions for creating and destroying a boson in a quantum state with N bosons.

$$b_p^+|(N)p>=\sqrt{N+1}|(N+1)p> \qquad b_p|(N)p>=\sqrt{N}|(N-1)p> \quad \text{(A.5)}$$

We will treat with nucleons, which are fermions.

- **Operators in the second quantization:**

- One-body operators:

$$O^{(1)} = \sum_{p,q} < p|O|q > a_p^+ a_q \quad \text{(A.6)}$$

Where: $< p|O|q >= \int d\vec{r} \phi_p^*(\vec{r}) O(\vec{r}) \phi_q(\vec{r})$

- Two-body operators:

$$O^{(2)} = \frac{1}{4} \sum_{p,q,r,s} < p,q|O|r,s >_{na} a_p^+ a_q^+ a_s a_r \quad \text{(A.7)}$$

Where: $< p,q|O|r,s >_{na} = \int\int d\vec{r}_1 d\vec{r}_2 \phi_p^*(\vec{r}_1)\phi_q^*(\vec{r}_2) O(\vec{r}_1,\vec{r}_2)(1-P_{1\leftrightarrow 2})\phi_r(\vec{r}_1)\phi_s(\vec{r}_2)$

$P_{1\leftrightarrow 2}$ is an operator which interchanges the coordinates of particles 1 and 2.

- **Angular momentum:**

Coupling of two particles of angular momenta j_1 and j_2 to a total angular momentum J, M:

$$|j_1, j_2; JM >= \\ = \frac{1}{\sqrt{1-\delta_{12}(-1)^{j_1+j_2-J}}} \sum_{\substack{m_1,m_2 \\ m_1+m_2=M}} < j_1 m_1, j_2 m_2 | JM > a^+_{j_1 m_1} a^+_{j_2 m_2} | > \quad \text{(A.8)}$$

Where $< j_1 m_1, j_2 m_2 | JM >$ is the Clebsch-Gordan coefficient.

- **Hole creation operator:**

$$\tilde{a}_{j,m} \equiv (-1)^{j+m} a_{j,-m} \quad \text{(A.9)}$$

- **Normal order:**

All the creation operators at the left of the annihilation operators. It is denoted by: $N(O_1 \dots O_2)$, where $O_1 \dots O_2$ are operators.

- **Contraction:**

$$\overbrace{O_p O_q} =< 0 | O_p O_q | 0 > \quad \text{(A.10)}$$

- **Wick's theorem:**

$$O_1 \dots O_N = N(O_1 \dots O_N) + \sum_{p<q} N(O_1 \dots \overbrace{O_p \dots O_q} \dots O_N) + \\ + \sum_{\substack{p<q \\ r<s}} N(O_1 \dots \overbrace{O_p \dots O_q} \dots \overbrace{O_r \dots O_s} \dots O_N) + \dots \quad \text{(A.11)}$$

A.2 Hartree-Fock (HF) method

Starting from the A-particle Hamiltonian with two-body interactions:

$$H = \sum_{p,q} < p|T|q > a_p^+ a_q + \frac{1}{4} \sum_{p,q,r,s} < pq|V|rs >_{na} a_p^+ a_q^+ a_s a_r \qquad \text{(A.12)}$$

Aplying Wick's theorem we obtain:

$$E_0 \equiv < 0|H|0 > = \sum_p < p|T|p > + \frac{1}{2} \sum_{p,q} < pq|V|pq >_{na} \qquad \text{(A.13)}$$

And the Hamiltonian results:

$$H = E_0 + \sum_p \epsilon_p N(a_p^+ a_p) + \frac{1}{4} \sum_{p,q,r,s} < pq|V|rs >_{na} N(a_p^+ a_q^+ a_s a_r) \qquad \text{(A.14)}$$

Where:

$$\epsilon_p = < p|T|p > + \sum_q < pq|V|pq >_{na} \qquad \text{(A.15)}$$

Are the Hartree-Fock equations.

We see that the Hamiltonian has been separated into: the energy of the reference state E_0, the single particle energy contributions ϵ_p (long range force), and the residual interaction $< pq|V|rs >$ (short ranged).

A.3 BCS pairing theory

As a trial approach to the 0^+ ground state wave function we propose a product state of $N/2$ pairs:

$$|N > = \sum_{p>0} (c_p(N) a_p^+ \tilde{a}_p^+)^{N/2} |HF > \qquad \text{(A.16)}$$

In order to determine the coefficients $c_p(N)$ we study the variational problem:

$$\delta < N|H|N > = 0 \qquad \text{(A.17)}$$

We can study this difficult problem in a more easy way by changing the trial wave function by another one simpler to treat and that, if projected onto the $N/2$ pairs space, gives back the $|N >$ solution:

$$|BCS>=\prod_{p>0}(u_p+v_p a_p^+ \tilde{a}_p^+)|HF> \tag{A.18}$$

It is called the BCS ground state, and although it does not correspond to a definite number of physical particles, the mean value of the number of particles can be calculated with the help of the Number Operator (considering particles and holes).

The state $|BCS>$ is the vacuum state for the operator:

$$\alpha_p = u_p a_p - v_p \tilde{a}_p^+ \tag{A.19}$$

The equation A.19 is called **Canonical Bogoljubov-Valatin Transformation**.

The conservation of the number of particles can be set as a bond by adding the term $-\lambda\hat{n}$ to the HF hamiltonian (*Lagrange* multipliers method):

$$\tilde{H}_{HF} = H'_{HF} - \lambda\hat{n} \tag{A.20}$$

λ is the chemical potential (or *Fermi* energy, which is related to the energy level filled in the single particle picture), and it is function of the particle number. In the special case where the pairing interaction has a constant strength G (which usually has the value of 23/A), the new hamiltonian is given by:

$$\tilde{H} = \sum_p (E_p - \lambda)(a_p^+ a_p + \tilde{a}_p^+ \tilde{a}_p) - G\sum_{p,q>0} a_p^+ \tilde{a}_p^+ \tilde{a}_q a_q \tag{A.21}$$

And the following BCS equations are obtained:

$$\begin{aligned} 2(\tilde{E}_p - \lambda)u_p v_p &= \Delta(u_p^2 - v_p^2) \\ \Delta = G\sum_{p>0} u_p v_p \qquad \tilde{E}_p &= E_p - G v_p^2 \end{aligned} \tag{A.22}$$

Where Δ is the so called *gap parameter*.

By performing some additional calculations, on the basis of the constant strength for the pairing interaction, it is possible to obtain explicit expressions for u^2 and v^2:

$$u_p^2 = \frac{1}{2}\left[1 + \frac{E_p - \lambda}{\sqrt{(E_p - \lambda)^2 + \Delta^2}}\right]$$
$$v_p^2 = \frac{1}{2}\left[1 - \frac{E_p - \lambda}{\sqrt{(E_p - \lambda)^2 + \Delta^2}}\right] \tag{A.23}$$

From where can be seen that v_p^2 and u_p^2 denote the occupation and depopulation probability, respectively, and are correlated by the normalization condition (obtained by applying the anticonmutator to the quasiparticle operator):

$$v_p^2 + u_p^2 = 1 \tag{A.24}$$

And the so called *gap equation*:

$$\frac{G}{2}\sum_{p>0}\frac{1}{\sqrt{(E_p - \lambda)^2 + \Delta^2}} = 1 \tag{A.25}$$

The Hamiltonian can be rewritten in terms of the quasiparticle operators as:

$$\tilde{H} = \sum_{p>0} E_p(\alpha_p^+\alpha_p + \tilde{\alpha}_p^+\tilde{\alpha}_p) + H'_{res} \tag{A.26}$$

A.4 Quasiparticle Random Phase Aproximation (QRPA)

It is possible to express the QRPA ground and excited states by using the creation and destruction operators B_ν^+ and B_ν, satisfying:

$$B_\nu^+ = B_{(pq)_\nu}^+ = \frac{[\alpha_p^+\alpha_q^+]_\nu}{\sqrt{1+\delta_{pq}}}$$
$$\tilde{B}_\nu = (-1)^{J_\nu + M_\nu} B_{-\nu} \tag{A.27}$$

Where $\frac{1}{\sqrt{1+\delta_{pq}}}$ is a normalization factor for the angular momentum coupling.

The QRPA operators Ω_c^+ are constructed as:

$$\Omega_c^+ = \sum_\nu (X_\nu^c B_\nu^+ - Y_\nu^c \tilde{B}_\nu) \tag{A.28}$$

If the factors Y_ν^c are small, the correlated ground state does not differ very much from the HF ground state, and the operators Ω_c^+, Ω_c fulfill approximately the boson conmutation relation (the so called *quasi-boson approximation*):

$$[\Omega_c, \Omega_{c'}^+] \approx \delta_{cc'} \tag{A.29}$$

The equation of motion for the Ω_c^+ operators can be writen as:

$$\frac{\partial \Omega_c^+}{\partial t} = [H, \Omega_c^+]|0> = E_c \Omega_c^+ |0> \tag{A.30}$$

The variation of the equation with respect to X_ν^c and Y_ν^c, and the application of:

$$< 0|\Omega_c^+ =< 0|H\Omega_c^+ = 0 \tag{A.31}$$

Gives the QRPA equations:

$$\begin{pmatrix} A & B \\ B^* & A^* \end{pmatrix} \begin{pmatrix} X^c \\ Y^c \end{pmatrix} = E_c \begin{pmatrix} 1 & 0 \\ 0 & -1 \end{pmatrix} \begin{pmatrix} X^c \\ Y^c \end{pmatrix} \tag{A.32}$$

A.5 QuasiParticle-Core coupling model (QP-C)

The ground state of the even-even core is assumed to be known from HFB-theory.

We choose an effective Hamiltonian of the form:

$$H = H_{11} + V_{22} + V_{13} \tag{A.33}$$

H_{11} is the one-quasiparticle part, which includes a static mean-field and pairing interactions. It is diagonal in the quasiparticle states α_μ^+ and α_μ, with eigenenergies $\pm E_\mu$, respectively.

The other two contributions to the Hamiltonian account for the residual interaction.

V_{22} acts in the 1p1h-channel and leads in the QP-picture to correlated 2-QP excitations described with QRPA.

V_{13} acts only in the odd-mass system, leading to the coupling of 1-QP states $|\mu >= \alpha_\mu^+|0>$ to core-excited 3-QP configurations $|(\mu c)j >= [\alpha_\mu^+ \Omega_c^+]_j|0>$. The 1-QP-plus-phonon states are coupled to angular momentum (j, m) and carry

parity $\pi(\mu c) = \pi(\mu)\pi(c)$. They are considered as elementary excitations and their excitation energies are given by the addition of the unperturbed core and the single particle ones:

We can define the operator:

$$\Upsilon_{\mu c,j} = [\Omega_c \alpha_\mu]_j \tag{A.34}$$

$$E_{\mu c} = E_\mu + E_c \tag{A.35}$$

The orthogonality relations are:

$$< 0|\alpha_\mu \Upsilon^+_{\mu' c',j'}|0 >= 0 \qquad < 0|\Upsilon_{\mu c,j} \Upsilon^+_{\mu' c',j'}|0 > \approx \delta_{\mu\mu'}\delta_{cc'}\delta_{jj'} \tag{A.36}$$

The quasi-boson approximation amounts to assume that the dynamics (and statistics) of the quasiparticle coupled to the excited core remains the same as in the ground state.

The QP-C model wave function of states $|\lambda j >$, with energy λ, angular momentum j, and parity π, in odd-mass nuclei are described as superpositions of one and three quasiparticle configurations. The correlated odd-quasiparticle states $|\lambda j >= \Gamma^+_\lambda(j)|0 >$ are defined in terms of excitation operators:

$$\begin{aligned} \Gamma^+_\lambda(j,m) = &\sum_n (z_{nj}(\lambda)\alpha^+_{nj} + \tilde{z}^*_{nj}(\lambda)\tilde{\alpha}_{nj}) + \\ &+ \sum_{\mu c} (z_{\mu c}(\lambda)\Upsilon^+_{\mu c,j} + \tilde{z}^*_{\mu c}(\lambda)\tilde{\Upsilon}_{\mu c,j}) \end{aligned} \tag{A.37}$$

Where n indicates summation over radial states.

These operators are defined with respect to the correlated QRPA-ground state $|0 >$ of the even-mass core rather than the quasiparticle vacuum state $|BCS >$. The correlated ground state is defined by the orthogonality condition $\Omega_c|0 >= 0$ to be fulfilled for all the QRPA-states. The QRPA-ground state differs from $|BCS >$ by admixtures of at least 4-QP configurations.

As known excitations in the even-mass system can also be created by annihilating virtual higher order ground state configurations as described by the "time-reversed" contributions in the QRPA-state operators. Ground state correlations have similar important consequences for odd-quasiparticle states. Since

$|0>$ is no longer the vacuum state for the operators α_μ, the final configuration can also be excited by annihilating a quasiparticle from the admixtures to $|0>$. Consequently, the odd-mass state operators contain, in general, contributions from the time-reversed counterparts $\tilde{\alpha}_\mu$ and $\tilde{\Upsilon}_{\mu c,j}$ of one and three quasiparticle states, respectively.

In analogy to RPA theory, we can impose the stronger condition $\Gamma_\lambda|0>= 0$, which allows us to obtain the correlated ground state in a consistent way, and to express the orthogonality condition for the odd-mass states as an anti-commutator:

$$\{\Gamma_\lambda(j), \Gamma^+_{\lambda'}(j')\} = \delta_{\lambda\lambda'}\delta_{jj'} \tag{A.38}$$

This is an important result showing that the Γ^+ operators obey approximately Fermion anti-commutator rules. In analogy to the quasi-boson approximation of RPA-theory they may be considered as quasi-fermion operators. Similar to the quasi-boson assumption, also here *Fermi* statistics are fulfilled only approximately on the level of expectation values.

The different components of the odd-mass system are projected out from the state operator Γ^+_λ by:

$$\begin{aligned} \{\alpha_\mu, \Gamma^+_\lambda\} = z_\mu(\lambda) \qquad \{\tilde{\alpha}^+_\mu, \Gamma^+_\lambda\} = \tilde{z}^*_\mu(\lambda) \\ \{\Upsilon_{\mu c,j}, \Gamma^+_\lambda\} = z_{\mu c}(\lambda) \qquad \{\tilde{\Upsilon}^+_{\mu c,j}, \Gamma^+_\lambda\} = \tilde{z}^*_{\mu c}(\lambda) \end{aligned} \tag{A.39}$$

In the preceeding sections, the QP-C theory was formulated in the QP picture. From a theoretical point of view, the quasiparticle approach has the advantage that the dynamics of hole and particle motion are treated symmetrically and both types of excitations are described in an unified way. However, in order to describe physical systems, the theoretical results have to be projected onto the hole and particle channels, respectively. In this section spectroscopic factors and correlated single particle wave functions are discussed.

The overlap of the model states Γ^+_λ with a physical particle state a^+_λ is described by the spectroscopic amplitudes:

$$\begin{aligned} C^{(+)}_\mu(\lambda) = \{\Gamma_\lambda, a^+_\mu\} = z^*_\mu(\lambda)u_\mu + \tilde{z}_\mu(\lambda)v_\mu \\ C^{(-)}_\mu(\lambda) = \{\Gamma_\lambda, \tilde{a}_\mu\} = -z^*_\mu(\lambda)v_\mu + \tilde{z}_\mu(\lambda)u_\mu \end{aligned} \tag{A.40}$$

These expressions lead to the single particle spectroscopic factors:

$$S_\lambda^{(\pm)} = \sum_\mu |C_\mu^{(\pm)}(\lambda)|^2 \tag{A.41}$$

The spectroscopic amplitudes C represent the correlated quasiparticle wave function in a basis of physical nucleon states which are defined by the eigenstates of the static mean-field. Thus, once the C-amplitudes have been determined, the correlated single particle/hole wave functions are known in any coordinate representation. In $\vec{r}$-space, the correlated single particle wave functions are defined as:

$$\Phi_\lambda^{(\pm)}(\vec{r}) = \frac{1}{\sqrt{S_\lambda^{(\pm)}}} \sum_{n_\mu} C_\mu^{(\pm)}(\lambda)\varphi_\mu(\vec{r}) \tag{A.42}$$

Where the eigenfunctions of the static mean-field are denoted by φ_μ.

n_μ indicates that the summation extends only over radial states.

As a function of the excitation energy, the C-coefficients vary in magnitude similarly to the strength distributions and the amplitudes of the wave functions would fluctuate correspondingly. By normalizing the wave function as has been done, this simple type of state dependence is projected out.

Bibliography

[Ann90] R. Anne *et al.*, Physics Letters B **250**, 19 (1990).

[Arn87] E. Arnold *et al.*, Physics Letters B **197**, 311 (1987).

[Arn92] E. Arnold *et al.*, Physics Letters B **281**, 592 (1992).

[Aud95] G. Audi and A. H. Wapstra, Nuclear Physics A **595**, 409 (1995).

[Aum00] T. Aumann *et al.*, Phys. Rev. Lett. **84**, 35 (2000).

[Bar96] F. Barranco, E. Vigezzi and R. A. Broglia, Z. Phys. A **356**, 45 (1996).

[Bar97] F. Barranco and E. Vigezzi, International School of Heavy Ion Physics, World Scientific, 217 (1997).

[Bar00] F. Barranco and P. G. Hansen, Euro. Phys. Journal A **7**, 479 (2000).

[Bau96] T. Baumann *et al.*, Acta Physica Universitatis Comenianae **XXXVII**, 3 (1996).

[Bau98] T. Baumann *et al.*, Physics Letters B **439**, 256 (1998).

[Bau99] T. Baumann, PhD. Dissertation, University of Giessen (1999).

[Baz98] D. Bazin *et al.*, Physical Review C **57**, 2156 (1998).

[Bel01] M. Belleguic *et al.*, Nuclear Physics A **682**, 136 (2001).

[Ber77] G. Bertsch *et al.*, Nuclear Physics A **284**, 399 (1977).

[Ber99] C. A. Bertulani, Lecture Notes on Reactions with Radioactive Beams, GSI - Darmstadt, 49 (1999).

[Bje36] T. Bjerge and K. J. Broström, Nature, **138**, 400 (1936).

[Bor86] M. J. G. Borge *et al.*, Nuclear Physics A **460**, 373 (1986).

[Bor88] M. J. G. Borge *et al.*, Nuclear Physics A **490**, 287 (1988).

[Bor91] M. J. G. Borge *et al.*, Z. Phys. A **340**, 225 (1991).

[Bor93] M. J. G. Borge *et al.*, Nuclear Physics A **460**, 664 (1993).

[Bri26] L. Brillouin, Comptes Rendus **183**, 24 (1926).

[Bro83] B. A. Brown, Rev. Mex. Fis. (Suppl. 2) **39**, 21 (1983).

[Bro01] B. A. Brown *et al.*, Prog. Part. Nucl. Phys. **47**, 517 (2001).

[Bro02] B. A. Brown *et al.*, Physical Review C **65**, 061601 (2002).

[Bro03] B. A. Brown, P. G. Hansen and J. A. Tostevin, Phys. Rev. Lett. **90**, 159201 (2003).

[Caa02] M. Caamaño Fresco, Tesina de licenciatura, Universidade de Santiago de Compostela, (2002).

[Cor97] D. Cortina-Gil *et al.*, Physics Letters B **401**, 9 (1997).

[Cor01] D. Cortina-Gil *et al.*, Euro. Phys. Journal A **10**, 49 (2001).

[Cor02] D. Cortina-Gil *et al.*, Physics Letters B **529**, 36 (2002).

[Cor03a] D. Cortina-Gil *et al.*, Nuclear Physics A **720**, 3 (2003).

[Cor03b] D. Cortina-Gil *et al.*, (Submitted to Phys. Rev. Lett.)

[Eck90] F. J. Eckle *et al.*, Nuclear Physics A **506**, 159 (1990).

[Ege02] P. Egelhof *et al.*, Euro. Phys. Journal A **15**, 27 (2002).

[Fer01] J. Fernández Vázquez, Diploma Thesis, Universidade de Santiago de Compostela, (2001).

[Fes91] H. Feshbach, Theoretical Nuclear Physics - Nuclear Reactions, John Wiley and Sons, (1991).

[Fir96] R. B. Firestone, 8th edition CD-ROM of the Table of Isotopes, (1996).

[Flo52] B. H. Flowers, Proc. Roy. Soc. A **212**, 248 (1952).

[For99] S. Fortier *et al.*, Physics Letters B **461**, 22 (1999).

[Gei92] H. Geissel *et al.*, Nucl. Inst. Methods B **70**, 286 (1992).

[Gla55] R. J. Glauber *et al.*, Physical Review **99**, 1515 (1955).

[Gla59] R. J. Glauber, Lectures on theoretical Physics **1**, Interscience, 315 (1959).

[Gui02] D. Guillemaud-Müller Euro. Phys. Journal A **13**, 63 (2002).

[Han96] P. G. Hansen, Phys. Rev. Lett. **77**, 1016 (1996).

[Han87] P. G. Hansen and B. Jonson, Europhys. Lett. **4**, 409 (1987).

[Hen96] K. Hencken, G. Bertsch and H. Esbensen, Physical Review C **54**, 3043 (1996).

[Hey94] K. L. G. Heyde, The Nuclear Shell Model, Springer-Verlag, (1994).

[Hli98] V. Hlinka *et al.*, Nucl. Inst. and Methods A **419**, 503 (1998).

[Hol92] R. Holzmann *et al.*, GSI Annual Report, 48 (1992).

[Iwa97] N. Iwasa et al., Nucl. Inst. Methods B **126**, 284 (1997).

[Jen00] A. S. Jensen and K. Riisager, Physics Letters B **480**, 39 (2000).

[Jur02] B. Jurado, K.-H. Schmidt and K.-H. Behr, Nucl. Inst. and Methods A **483**, 603 (2002).

[Kah00] E. Kahn *et al.*, Physics Letters B **490**, 45 (2000).

[Kan95] J. Kantele, Handbook of Nuclear Spectrometry, Academic Press, (1995).

[Kan02] R. Kanungo *et al.*, Phys. Rev. Lett. **88**, 142502 (2002).

[Kan03] R. Kanungo *et al.*, Phys. Rev. Lett. **90**, 159202 (2003).

[Kla69] R. Klapisch *et al.*, Phys. Rev. Lett. **23**, 652 (1969).

[Kra26] H. A. Kramers, Zeits. f. Phys. **39**, 828 (1926).

[Kob88] T. Kobayashi *et al.*, Phys. Rev. Lett. **60**, 2599 (1988).

[Kob89] T. Kobayashi *et al.*, Physics Letters B **232**, 51 (1989).

[Kof51] O. Kofoed-Hansen and K. O. Nielsen, K. Dan. Vidensk. Selsk. Mat. Fys. Medd., **26**, (1951).

[Lag01] A. Lagoyannis *et al.*, Physics Letters B **518**, 27 (2001).

[Lan64] A. M. Lane, Nuclear Theory, Benjamin, (1964).

[Lap01] V. Lapoux *et al.*, Physics Letters B **517**, 18 (2001).

[Len90] H. Lenske and J. Wambach, Physics Letters B **249**, 377 (1990).

[Len03a] H. Lenske, (private communication).

[Len03b] H. Lenske, C. M. Keil and F. Hofmann, (submitted to World Scientific).

[Leo93] W. R. Leo, Techniques for Nuclear and Particle Physics Experiments, Springer-Verlag, 127-213 (1993).

[Lvo01] Y. Lvovna-Parfenova, Diploma Thesis, Göteborg University, Sweden (2001).

[Mad01] V. Maddalena and R. Shyam, Physical Review C **63**, 051601 (2001).

[May50] M. G. Mayer, Physical Review **78**, 22 (1950).

[Mil83] D. J. Millener *et al.*, Physical Review C **28**, 497 (1983).

[Nav98] A. Navin *et al.*, Phys. Rev. Lett. **81**, 5089 (1998).

[Nav00] A. Navin *et al.*, Phys. Rev. Lett. **85**, 266 (2000).

[Neg74] J. W. Negele, Physical Review C **9**, 1054 (1974).

[Neg96] F. Negoita *et al.* Physical Review C **54**, 1787 (1996).

[Orr92] N. A. Orr *et al.*, Phys. Rev. Lett. **69**, 2050 (1992).

[Ots01] T. Otsuka *et al.*, Phys. Rev. Lett. **87**, 082502 (2001).

[Oza00] A. Ozawa *et al.*, Phys. Rev. Lett. **84**, 5493 (2000).

[Oza01] A. Ozawa *et al.*, Nuclear Physics A **691**, 599 (2001).

[Oza02] A. Ozawa *et al.*, Nuclear Physics A **709**, 60 (2002).

[Pfu94] M. Pfuetzner *et al.*, Nucl. Inst. and Methods B **70**, 213-218 (1994).

[Pos66] A. M. Poskanser *et al.*, Phys. Rev. Lett. **17**, 1271 (1966).

[Rac52] G. Racah and I. Talmi, Physica **18**, 1097 (1952).

[Ray79] L. Ray, Physical Review C **20**, 1857 (1979).

[Row70] D. J. Rowe, Nuclear Collective Motion, Methuen, (1970).

[Sak99] H. Sakurai *et al.*, Physics Letters B **448**, 180 (1999).

[Sau00a] E. Sauvan, PhD. Thesis, Caen University, France, (2000).

[Sau00b] E. Sauvan *et al.*, Physics Letters B **491**, 1 (2000).

[Sau03] E. Sauvan *et al.*, (submitted to Phys. Rev. C)

[Sch64] C. Schaerf and R. Scrimaglio, Nucl. Instr. and Meth. **30**, 359 (1964).

[Sch95] W. Schwab *et al.*, Z. Phys. A **350**, 283 (1995).

[Sme98] M. H. Smedberg, PhD. Thesis, Göteborg University, Sweden, (1998).

[Sme99] M. H. Smedberg *et al.*, Physics Letters B **452**, 1 (1999).

[Sor01] O. Sorlin *et al.*, Nuclear Physics A **685**, 186c (2001).

[Spe77] J. Speth, E. Werner and W. Wild, Phys. Reports **33**, 127 (1977).

[Sta03] M. Staniou *et al.*, (submitted to Phys. Rev. C)

[Sto99] A. Stolz *et al.*, GSI Scientific Report **99-1**, 174 (1999).

[Sym79] T. J. M. Symon *et al.*, Phys. Rev. Lett. **42**, 40 (1979).

[Tal52] I. Talmi, Helv. Phys. Act. **25**, 185 (1952).

[Tan85a] I. Tanihata *et al.*, Physics Letters B **160**, 380 (1985).

[Tan85b] I. Tanihata *et al.*, Phys. Rev. Lett. **55**, 2676 (1985).

[Tar97] O. Tarasov *et al.*, Physics Letters B **409**, 64 (1997).

[Thi00] P. G. Thirolf *et al.*, Physics Letters B **485**, 16 (2000).

[Vis02] A. de Vismes *et al.*, Nuclear Physics A **706**, 295 (2002).

[Vos95] B. Voss et al., Nucl. Instr. and Meth. A **364**, 150 (1995).

[Wan99] S. Wan, PhD. Thesis, Univ. Heidelberg, May 1999.

[Wen26] G. Wentzel, Zeits. f. Phys. **38**, 518 (1926).

[Wes79] G. D. Westfall *et al.*, Phys. Rev. Lett. **43**, 1859 (1979).

[Zie91] C. Ziegler *et al.*, Sci. Rep. **GSI-91-1**, 291 (1991).

[ATIMA] *http://www-aix.gsi.de/~weick/atima*

[FRS] *http://www-wnt.gsi.de/frs/index.asp*

[GEANT] *http://wwwasdoc.web.cern.ch/wwwasdoc/geantold/GEANTMAIN.html*

[GSI] *http://www.gsi.de*

[MOCADI] *http://www-aix.gsi.de/~weick/mocadi*

[SEETRAM] *http://www-wnt.gsi.de/kschmidt/seetraminfo/SEETRAM.html*